MASTERARBEIT

Flamelet Modeling and Simulation of CH4/O2 Rocket Thrust Chambers

Author: **Perakis, Nikolaos**

Supervisor: Dr.-Ing. Blazenko Ivancic
Dipl.-Ing. Christof Roth

Issued: 01.04.2016
Submitted: 30.09.2016

Declaration of Authorship

Name: **Perakis, Nikolaos**

I hereby declare that this thesis is my own work prepared without the help of a third party. No other than the listed literature and resources have been used. All sources transferred literally or analogously to this work have been labeled accordingly.

Additionally, I hereby certify that this thesis has not been underlain in any other examination procedure up to the present.

....
Date, Sign

Acknowledgements

I would like to thank my supervisors Dr. Blazenko Ivancic and Dipl.-Ing. Christof Roth for their support throughout the 6 months of the thesis. I really appreciate the time they invested in the project and the interest they demonstrated during our discussions, always eager to share their advice and try to tackle the issues I encountered. I would also like to express my gratitude towards Dr. Konrad Makowka and Dr. Hendrik Riedmann as well as the other colleagues at Airbus Safran Launchers for their ideas, comments and fruitful discussions.

Munich, September 30th 2016

Nikolaos Perakis

Abstract

The propellant combination of methane and oxygen is a very promising candidate for future rocket propulsion engines. In order to obtain a more comprehensive understanding of the performance properties of this new propellant, intensive efforts are placed in its experimental characterization as well as in the proper modeling of its combustion attributes. Within the frame of this thesis, the numerical simulation of the CH_4/O_2 combustion using the Flamelet model is undertaken. Similar to the chemical equilibrium model, in the Flamelet description of the combustion processes, a tabulation of the chemistry takes place, which omits the need for the solution of additional transport equations for each individual chemical species. In contrast to the equilibrium model however, Flamelet enables the inclusion of non-equilibrium effects and is hence more appropriate for the description of hydrocarbon combustion, where slower reaction rates are present.

For the implementation of the Flamelet model, a tool for the chemistry table generation is necessary. The approach taken in this work for the development of this library generator involves solving multiple instances of the counterflow diffusion flame problem and subsequently tabulating the obtained one-dimensional profiles. The open source chemistry tool "Cantera" is utilized in this process, using the Python interface. A significant degree of flexibility is connected to the developed Flamelet generator since it allows a variable definition of the reaction mechanism among other assets, in contrast to commercial tools like the CFX-RIF, where the user has limited control. Following a validation of the generator module, some peculiarities of the methane combustion (compared to hydrogen combustion) are identified, mainly attributed to the slower reaction rates and the higher dissociation degree of methane. Using the resulting Flamelet tables, two subscale rocket engine test cases are simulated with the commercial solver ANSYS CFX: the ISP-1 and Romeo combustors, which are operated with GOX/GCH₄ and subcritical LOX/GCH₄ respectively. The Flamelet tables originating from the Cantera tool manage to produce satisfactory results similar to the ones obtained with tables from the RIF generator. An exploration of other models regarding the molecular and turbulent transport properties of the hot gas as well as the description of LOX's thermodynamic properties is carried out to further improve the simulation results. The wall heat flux results obtained appear very promising, whereas the chamber pressure and efficiency seem to be underestimated compared to the experimental measurements. Several suggestions for the source of this discrepancy are analyzed and can serve as a starting point for further investigations.

Table of contents

Nomenclature

Latin characters

Symbol	Definition	Units
A	Pre-exponential factor	[1/s]
a	Strain rate	[1/s]
C	Species name	[-]
c	Speed	[m/s]
c_p	Specific heat capacity at constant pressure	[J/(kg·K)]
c_v	Specific heat capacity at constant volume	[J/(kg·K)]
D	Mass diffusivity	[m^2/s]
Da	Damköhler number	[-]
E	Total specific enthalpy	[J/kg]
$\boldsymbol{F}$	External force	[N]
$\underline{\underline{F}}$	Brokaw connectivity matrix	[-]
g	Gravity acceleration	[m/s^2]
h	Specific static enthalpy	[J/kg]
I_{sp}	Specific impulse	[s]
$\boldsymbol{j}$	Diffusion flux	[m^2/s]
L	Length	[m]
Le	Lewis number	[-]
K	Number of species	[-]
k	Turbulent kinetic energy	[J/kg]
k_B	Boltzmann constant	[J/K]
M	Molar mass	[kg/mol]
m	Molecule mass	[kg]
$\dot{m}$	Mass flow	[kg/s]
$\boldsymbol{n}$	Normal vector	[-]
p	Pressure	[bar]
Pr	Prandtl number	[-]
$\dot{q}$	Heat flux	[W/m^2]
R	Universal gas constant	[J/(mol·K)]
r	Radial coordinate	[m]
s	Specific entropy	[J/(kg·K)]
S	Surface area	[m^2]

$\underline{S}$	Mean rate of strain tensor	[1/s]
Sc	Schmidt number	[-]
T	Temperature	[K]
t	Time	[s]
$\boldsymbol{u}$	Velocity	[m/s]
V	Volume	[m^3]
x, y, z	Spatial coordinates	[m]
X	Molar fraction	[-]
y^+	Dimensionless wall distance	[-]
Y	Mass fraction	[-]
Z	Mixture fraction	[-]

Greek characters

Symbol	Definition	Units
α_T	Thermal diffusivity	[m^2/s]
β	Temperature exponent	[-]
Γ	Gamma function	[-]
δ	Kronecker delta	[-]
ϵ	Eddy dissipation rate	[m^2/s^3]
ϵ	Wall depth of Lennard-Jones	[J]
κ	Reaction rate	[1/s]
λ	Thermal conductivity	[W/(m·K)]
Λ	Pressure curvature	[1/m]
μ	Dynamic viscosity	[kg/(m·s)]
ν	Kinematic viscosity	[m^2/s]
ν', ν''	Stoichiometric coefficients	[-]
ρ	Density	[kg/m^3]
σ	Collision diameter	[m]
τ	Time scale	[s]
$\underline{\tau}$	Stress tensor	[bar]
$\underline{\Phi}$	Brokaw connectivity matrix	[-]
χ	Scalar dissipation rate	[1/s]
Ω	Reduced collision integral	[-]
ω	Eddy frequency	[1/s]
$\dot{\omega}$	Species source term	[kg/(m^3·s)]
$\dot{\omega}_T$	Temperature source term	[kgK/(m^3·s)]

Indices

Symbol	Definition
0	Formation or initial value
a	Activation
B	Backward
c	Combustion
e	Exhaust
F	Forward
f	Final
fu	Fuel
mix	Mixture
$norm$	Normalized
ox	Oxidizer
q	Quenching
R	Radiation
red	Reduced
s	Sound
st	Stoichiometric
t	Turbulent/eddy quantity
th	Throat
w	Wall
τ	Friction

Operators

Symbol	Definition
$\partial\,\bullet$	Partial derivative
$\nabla(\bullet)$	Gradient
$\nabla \cdot (\bullet)$	Divergence
$\langle\bullet\rangle$	Reynolds averaged quantity
$\bar{\bullet}$	Reynolds averaged quantity
$\tilde{\bullet}$	Favre averaged quantity
$[\bullet]$	Species concentration
$\bullet'$	Reynolds fluctuation
$\bullet''$	Favre fluctuation
$\bullet''^2$	Variance

Abbreviations

Symbol	Definition
BC	Boundary Condition
CDS	Central Differencing Scheme
CEA	Chemical Equilibrium with Applications
CFD	Computational Fluid Dynamics
CNES	Centre National d'Études Spatiales
DLR	Deutsches Zentrum für Luft- und Raumfahrt
DNS	Direct Numerical Simulation
EDM	Eddy Dissipation Model
EOS	Equation Of State
EVM	Eddy Viscosity Models
FDM	Finite Difference Method
FEM	Finite Element Method
FFSC	Full-Flow Stage Combustion
FVM	Finite Volume Method
GCH_4	Gaseous Methane
GOX	Gaseous Oxygen
ISRU	In-Situ Resource Utilization
LCH_4	Liquid Methane
LES	Large Eddy Simulation
LH_2	Liquid Hydrogen
LNG	Liquefied Natural Gas
LOX	Liquid Oxygen
MMH	Monomethylhydrazine
NS	Navier Stokes
ODE	Ordinary Differential Equation
O/F	Oxidizer to Fuel ratio
PDF	Probability Density Function
PDE	Partial Differential Equations
PPDF	Presumed Probability Density Function
RANS	Reynolds Averaged Navier Stokes
REACH	Registration, Evaluation, Authorization & restriction of CHemicals
RGP	Real Gas Properties
RIF	Representative Interactive Flamelet
RP-1	Rocket Propellant 1 / Refined Petroleum 1
RSM	Reynolds Stress Models

SSME	Space Shuttle Main Engine
SST	Shear Stress Transport
TRL	Technology Readiness Level
UDMH	Unsymmetrical Dimethylhydrazine
UDS	Upwind Differencing Scheme

1 Introduction

The scientific merit of space missions cannot be overstated, since they allow the performance of invaluable measurements used to extend mankind's knowledge and enable the ongoing discovery and exploration of celestial structures in outer space. The placement of scientific payloads in orbit as well as the launch of unmanned robotic probes and manned spacecraft for the physical exploration of space is made possible by the continuously evolving and growing field of space propulsion.

The technology which has distinguished itself as the most common solution in the field of spacecraft propulsion is the one of chemical rocket engines. The operating principle is rather simple and is based on Newton's third law: the acceleration of a propellant and its exhaust through the engine yields a force in the opposite direction according to the conservation of momentum.

Although rocket engines have been implemented for space applications since the 1950s, their improvement and further development are still topics of ongoing research. Reduction of costs, increase of the efficiency and reusability are some of the topics on which scientific efforts are focused on. A potential improvement could occur through the implementation of new propellant combinations.

1.1 Methane as a rocket propulsion fuel

In the field of launcher propulsion, liquid rocket engines have established themselves as the most widespread solution as far as the main and upper stage of the launcher is concerned. The most common liquid propellants in use today are LOX/LH$_2$, LOX/kerosene (RP-1) and nitrogen tetroxide (N$_2$O$_4$) with hydrazine (N$_2$H$_4$) or its variations (MMH, UDMH). LOX and LH$_2$ has been used in the Space Shuttle Main Engine (SSME), the Centaur upper stage of the Atlas V, Saturn V upper stages as well as the Vulcain and HM7-B engines of European Ariane 5 rocket among others. LOX and kerosene was implemented in the first stages of the Saturn V, Atlas V and Falcon, the Russian Soyuz, Ukrainian Zenit, and developmental rockets like Angara and Long March 6. Finally N$_2$H$_4$/MMH, or N$_2$H$_4$/UDMH is the main fuel for the Proton rocket, Long March rockets as well as the Aestus upper stage of Ariane 5.

LOX/CH$_4$ on the other hand is often regarded as a new promising propellant. Although full-scale rocket engines burning oxygen and methane have never flown, the interest in this propulsion combination has increased dramatically in the last years, including various studies and tests. Apart from academic institutions, the leading space companies have also

invested in a methane infrastructure. Specifically, SpaceX is developing the Raptor engine, which is intended to power high-performance lower and upper stages for heavy launch vehicles [1]. The French space agency (CNES) in collaboration with Airbus Safran Launchers is working on a reusable, cost-efficient LOX/LCH$_4$ engine called Promethee (Precursor Reusable Oxygen METHane cost Effective Engine) [2]. Finally, the privately-funded aerospace company Blue Origin, LLC develops the BE-4 rocket engine, which will operate using liquid oxygen and liquefied natural gas (LNG) as propellant [3].

Methane/oxygen is a green propellant combination, meaning that its products are non-toxic, human- and environmentally friendly. This is quite important within the framework of the REACH regulation, which addresses the production and use of chemical substances, and their potential impacts on both human health and the environment [4]. Within the same context, a potential replacement of hydrazine and its constituents is discussed, due to its high toxicity, and methane could be a candidate for that in many aerospace applications.
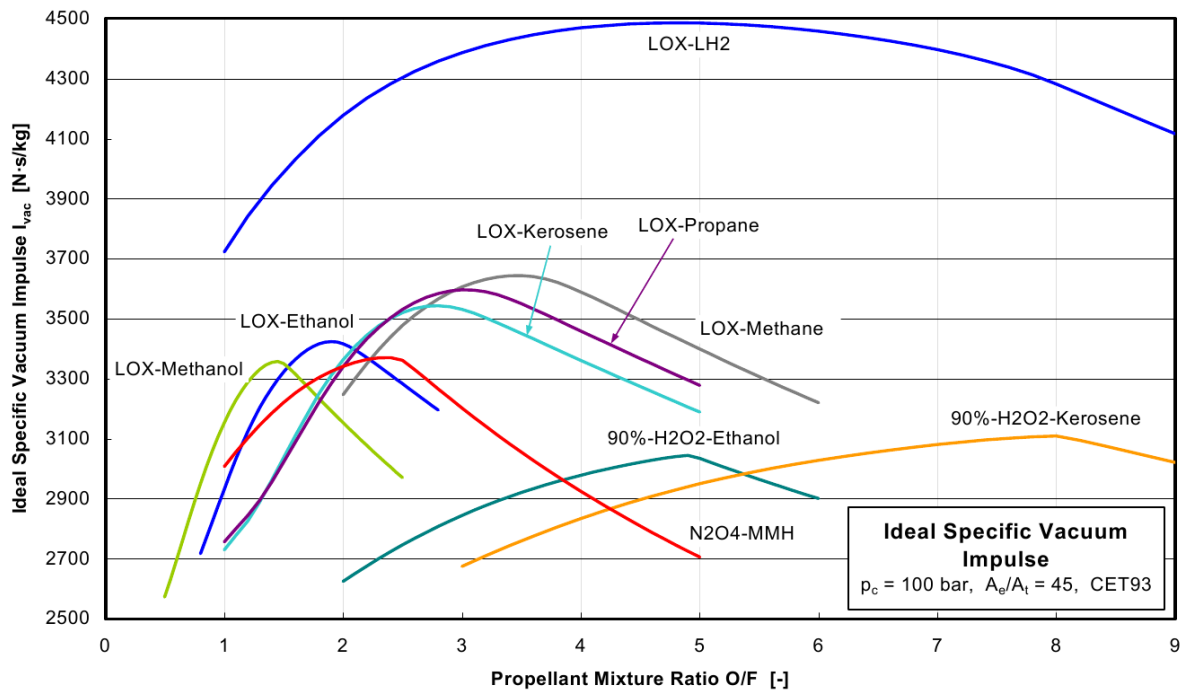
Figure 1.1: Ideal vacuum specific impulse for different propellant combinations (from Haidn et al. [5]).

Apart from its environmental aspects, methane is also advantageous from a performance standpoint. As Figure 1.1 shows, LOX/Methane possesses the highest specific impulse (I_{sp}) amongst other potential rocket fuels (excluding of course the highly energetic LOX/LH$_2$ combination). Compared to liquid hydrogen fuel, despite its lower I_{sp}, methane presents a higher density and a high vapor pressure. Due to it being less bulky than hydrogen, its weight-specific performance is higher than that of hydrogen. This implies that a smaller

tankage is required for the same mission and hence a lower structural mass, which could in turn increase the on board payload [6]. The higher density is also beneficial from the perspective of the turbopumps. LOX/LCH$_4$ turbopumps may be single shaft designed [7], which is not the case for LOX/LH$_2$ due to the too big a difference in liquid density between oxygen and hydrogen. The density of methane as a function of its thermodynamic state (pressure and temperature) is illustrated in Figure 1.2.

Moreover, although methane is also considered to be cryogenic (with a boiling temperature of approximately 110 K), it has the benefit of being easier to store than hydrogen, which boils already at 20 K. Mostly passive cooling can suffice to keep it cryogenic, whereas hydrogen needs active cooling, and demonstrates higher venting rates over time. This effect constitutes methane useful for deep space missions, with long mission durations. The higher boiling point has two further benefits. Firstly, it means that both fuel and oxidizer lines can be purged with gaseous nitrogen. Liquid hydrogen lines can only be purged with helium, as hydrogen's boiling point is below the melting point of other inert gases. This reduces the complexity of the system and also removes the need for helium to be brought on board, which is an expensive fossil gas. Secondly, methane's boiling point is close to the one of oxygen (approximately 90 K), which means that the temperature gradient between the oxidizer and fuel tanks is reduced. This in turn loosens the requirements for thermal insulation and spacing between the two tanks.
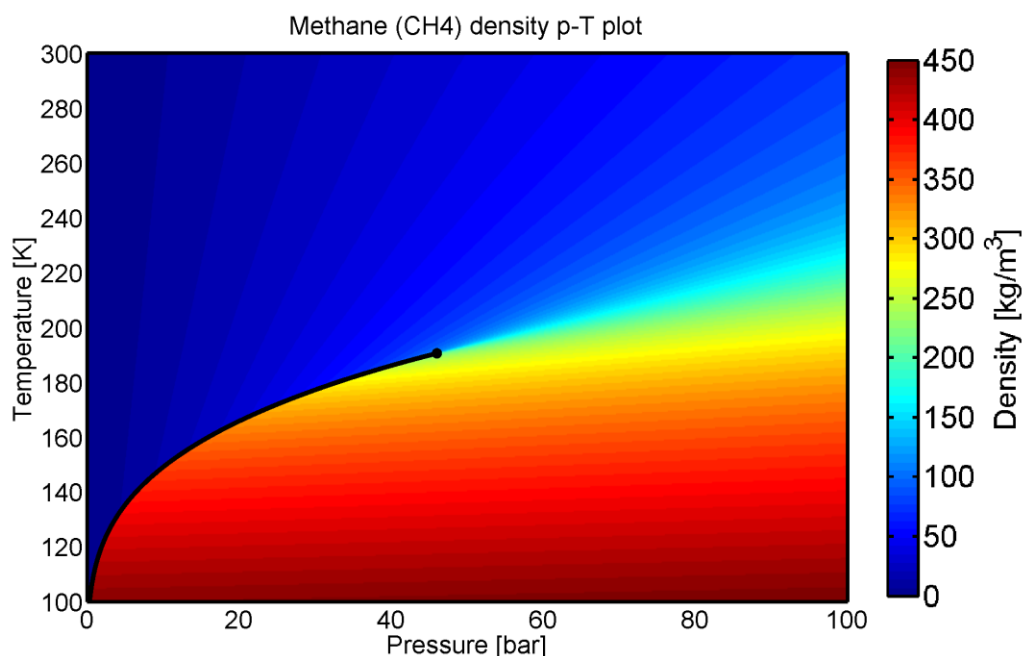
Figure 1.2: Density plot for methane as a function of temperature and pressure. Plot generated using data from the National Institute of Standards and Technology (NIST) [8].

Methane and RP-1 are roughly equivalent in realizable performance. As shown in Figure 1.1, CH$_4$ has slightly higher impulse – about 370 s in vacuum vs the 360 s of RP-1 – at the same

chamber pressure of 10 MPa. But, this is counterbalanced by its lower bulk density[1] of about 830 kg/m^3 vs about 1030 kg/m^3 for RP-1. The reasons why CH_4 is considered to be more promising than kerosene can be attributed to the following factors:

Methane does not coke (polymerize) at the operating temperatures of a rocket engine, whereas kerosene has a significant coking rate [9]. Therefore, methane engines have no residue build-up which means they can be reusable without the need for refurbishment. Due to the absence of coking, it is also easier to implement a full-flow stage combustion (FFSC) cycle where all the fuel and oxidizer flow goes through the pre-burner. Compared to partial flow stage combustion engines, higher chamber pressures are attainable leading to even higher specific impulse and thereby eliminating the performance deficiency of CH_4 compared to RP-1. Methane can also be used in expander cycles in contrast to RP-1, which is unsuitable for this stage design due to its high critical temperature, which does not allow it to be gaseous when entering the turbine [10].

Finally, methane is potentially manufacturable on Mars. With imported hydrogen (or native water), CO_2 (carbon dioxide) from the Martian atmosphere can be converted to CH_4 using the Sabatier reaction [11]. The idea of ISRU (In-Situ Resource Utilization) could potentially reduce the launch cost and the mass of the propellant needed for the return trip. Along with the better storability, it is a further factor that makes the use of methane for a Mars mission quite attractive.

A comparison matrix for the three most prominent propellant combinations is given in Table 1.1.

Table 1.1: Comparison of different propellant combinations.

	H_2/O_2	$RP-1/O_2$	CH_4/O_2
Performance	green	yellow	yellow
Propellant cost	red	yellow	green
Reusability	green	yellow	green
Full-flow stage combustion	green	red	green
Propellant transfer/storage	red	yellow	yellow
Mars propellant production	yellow	red	green

---

[1] Bulk density is the density of the combined fuel and oxidizer load in their appropriate ratios. Even though methane's density is roughly 430 kg/m^3, it is consumed with an oxidizer to duel ratio (O/F) equal to 3.5 compared to 2.1 for RP-1, hence a CH_4 rocket will be carrying more oxygen and less fuel by weight. Oxygen is pretty dense at 1140 kg/m^3 which is denser in fact than RP-1 (about 810 kg/m^3).

1.2 Scope of the thesis

The combination of methane and oxygen in rocket engine applications could potentially improve the flight performance of spacecraft propulsion modules, especially in interplanetary missions. For an effective utilization of this propellant, a better understanding of its properties and combustion characteristics is required.

Due to the costs associated with experimental testing programs, trial and error approaches have been limited by the rocket propulsion industry in the process of understanding physical mechanisms and developing new propulsion systems [12]. The improvement of today's rocket engines relies heavily on the numerical simulation of the physical phenomena taking place within the rocket thrust chamber. Applying analytical and/or numerical tools allows for a more resource efficient way of carrying out trade-off studies, deciphering complex physical and chemical processes and optimizing the performance in the design phase of propulsion systems.

Numerical simulations in the field of space propulsion enable predictions of the combustion and heat transfer phenomena taking place in the hot gas. The reliability of a simulation is however imminently connected to the chosen models being implemented and their validation. The high degree of complexity of the physical and chemical mechanisms taking place inside a rocket engine, including atomization, evaporation, mixing, two-phase flows, real gas thermodynamics, chemical reactions, supersonic velocities and flow/structure interaction, requires the introduction of models which simplify some of the simulated processes. The knowledge of the introduced simplifications and applied models is crucial for understanding the applicability limits of the simulation. Finally, the validation of the utilized models is required to ensure a reliable predictability, which occurs by comparing the simulation results with well-established test cases.

A physical process with significant influence on the performance of a chemical rocket engine is the one of combustion, i.e. the chemical reactions between oxidizer and fuel. This interaction of the propellants dictates the energy release in the chamber as well as the gas composition. The available enthalpy released during the reactions prescribes the temperature of the gas as well as its thermodynamic and transport properties. The performance and thermal loads of the chamber are hence directly connected to the combustion modeling.

In the present thesis, the Flamelet model for the simulation of CH_4/O_2 combustion is implemented. The main concept lies in separating the solution of the fluid dynamic processes from the combustion ones, due to the different time scales of the two phenomena. This is enabled by using pre-processed combustion tables (so-called Flamelet tables), which are accessed by the simulation code during runtime. This method has the

benefit of reducing the number of transport equations compared to other concepts (like the finite rate chemistry) and can hence lower the computational cost significantly. Moreover, the Flamelet model facilitates the description of chemical non-equilibrium effects in the thrust chamber as well as the use of a detailed reaction mechanism without additional computational effort. Although the method has been thoroughly examined for H_2/O_2 combustion cases, the focus is placed on methane, as it is a promising candidate for future launchers, and since its combustion characteristics in rocket engine applications are not entirely comprehended.

To achieve the generation of the Flamelet tables, a series of one-dimensional (1D) counterflow diffusion flames is solved with the open source tool Cantera, and the results are tabulated. A code programmed in Python was developed for this purpose. Although commercial tools for the table generation are available, the Python-based Cantera table generator allows for higher flexibility and user control. For the validation of the model, two test cases were simulated using the commercial solver ANSYS CFX. The GOX/GCH$_4$ subscale ISP-1 test case as well as the LOX/GCH$_4$ Romeo subscale engine was examined and the results were compared with the ones using commercial Flamelet generators like the CFX-RIF.

In Chapter 2, the fundamentals of rocket propulsion and the basics of Computational Fluid Dynamics (CFD) are presented. The modeling of the main thermal and fluid dynamic phenomena occurring in rocket engine applications is elaborated on, which includes the turbulence modeling, the description of transport and thermodynamic properties of the hot gas, phase change models and chemical reactions. Special emphasis is put on the latter one and specifically on the description of the turbulent nonpremixed combustion. In this frame, the Flamelet model is explained in detail, since it poses the main topic of the thesis. Chapter 3 gives an overview of the Cantera software and the modeling that goes into calculating the counterflow diffusion flames. In the same chapter, the code for the creation of the tables is analyzed in detail.

The results of the Flamelet generator are described in Chapter 4. There, a comparison with the theoretical equilibrium solution as well as with literature results is undertaken. Moreover, the main differences between the H_2/O_2 and CH_4/O_2 combustion properties (temperature and species composition) are underlined, in order to obtain a better understanding of methane's characteristics. Finally, Chapter 5 is used to give a detailed overview of the simulation results obtained for two test cases. The heat flux, pressure measurements and combustion efficiency are compared with the experimental results and the main differences between the Cantera and CFX-RIF tables' profiles are outlined. At the same time, the results are used in order to identify the most dominant phenomena taking place in methane/oxygen combustion that require further modeling in rocket engine applications.

2   Theory and Modeling

The field of combustion simulation in aerospace applications requires an understanding of the basic principles of rocket propulsion as well as knowledge about the modeling principles of the flow and heat transfer phenomena inside the thrust chamber.

In Section 2.1, the fundamental concepts of rocket propulsion needed for the correct interpretation of the simulation results are presented. Section 2.2 gives a detailed overview of the physical models included in the CFD simulation of a rocket combustor. After the general principles of the Navier-Stokes Equations and the turbulence modeling are shown in Sections 2.2.1 and 2.2.2 respectively, the modeling of transport properties, phase change and turbulent combustion, required for the simulation of the gas mixture in the chamber are outlined. Finally, Section 2.2.7 gives the necessary details on the Flamelet theory, which is also the combustion model that the present thesis is based on.

2.1   Basics of rocket propulsion

The main objective of a space propulsion device is to impart a velocity change onto the probe, satellite or launcher that it is attached to. This velocity increment Δv is achieved by means of expelling propellant with an effective exhaust speed c_e relative to the engine. The resulting Δv, assuming initial and final masses m_o and m_f respectively, is described according to the Tsiolkovsky equation [13]:

$$\Delta v = c_e \ln \left(\frac{m_o}{m_f} \right) \tag{2.1}$$

whereas the thrust force is given by the total mass flow $\dot{m}$:

$$F = \dot{m} c_e \tag{2.2}$$

An important merit of the performance of a rocket propulsion system is the specific impulse I_{sp}, which is defined as the total impulse per unit weight of the propellant. In Eq. (2.3) g, represents the acceleration due to gravity on the surface of the earth.

$$I_{sp} = \frac{\int_0^t F \, \mathrm{d}t}{\int_0^t \dot{m} g \, \mathrm{d}t} = \frac{c_e}{g} \tag{2.3}$$

The specific impulse can be also used to measure the efficiency of a rocket engine. A higher value for the I_{sp} translates to less propellant mass required for a certain velocity increment. Its value is mainly dictated by the choice of the propellants in the rocket engine and their mass ratio O/F. The O/F is defined as the ratio of the oxidizer mass flow to the fuel mass flow:

$$O/F = \frac{\dot{m}_{ox}}{\dot{m}_{fu}} \tag{2.4}$$

For the case of methane/oxygen combustion, the stoichiometric value of the oxidizer to fuel ratio is at $O/F \approx 4$. The maximal I_{sp} is achieved however at lower values and in the case of 100 bar and expansion ratio equal to 45, it occurs at $O/F \approx 3.5$, as Figure 1.1 indicates.

The value of the specific impulse is also dependent on the nozzle geometry and hence incorporates the effects of gas acceleration in the nozzle segment. A further performance merit is therefore required in order to characterize the efficiency of the combustion process in the chamber, decoupled from the nozzle performance. The characteristic velocity c^* fulfills these criteria, since it is a function of the propellant characteristics and the combustion chamber design, while being independent of the nozzle properties [14]. It is defined in Eq. (2.5):

$$c^* = \frac{p_c A_{th}}{\dot{m}} \tag{2.5}$$

and in the case of an ideal gas and 1D approach of the flow through the rocket combustion chamber, it can be shown that it is calculated by Eq. (2.6):

$$c^* = \sqrt{\frac{RT_c}{M\gamma}\left(\frac{\gamma + 1}{2}\right)^{\frac{\gamma+1}{\gamma-1}}} \tag{2.6}$$

In the notation used here, p_c represents the total combustion pressure at the throat, A_{th} the cross sectional area of the throat, T_c the combustion temperature, R the universal gas constant, M the molecular mass of the hot gas and γ its adiabatic exponent.

In order to examine the degree of completion of the energy release and the creation of high-pressure hot gas in the chamber, the efficiency of the characteristic velocity η_{c^*} is used. This represents the ratio between the actual value of c^*, as determined from the

measurements in Eq. (2.5) and the theoretical value from Eq. (2.6)[2]. The actual value of c^* obtained from measurements does not only refer to experimental tests but also to numerical simulations. The term "measurements" is used in that case for the numerical results obtained for the total pressure and mass flow rate.

Apart from the quality of the combustion, which is described by the characteristic velocity and its efficiency, a figure used for quantifying the performance of a rocket engine is the thrust coefficient c_F. It characterizes the transformation of internal energy into kinetic energy of the gas within the nozzle and is defined as follows:

$$c_F = \frac{F}{p_c A_{th}} = \frac{F}{\dot{m} c^*} \tag{2.7}$$

The thrust coefficient quantifies the increase in thrust due to the nozzle, by presenting the ratio of the actual thrust F to the theoretical thrust $p_c \cdot A_{th}$ at the throat. The effective exhaust speed is connected to the figures c^* and c_F by means of the expression in Eq. (2.8):

$$c_e = c_F \cdot c^* \tag{2.8}$$

2.2 Computational Fluid Dynamics

The solution of a fluid mechanics problem using CFD requires the description of the physical phenomena via a set of models. These models can be translated into a group of mathematical equations, which in turn are solved by the computer. The main objective when choosing the appropriate models is to approximate the physical processes as realistically as possible, while keeping the computational effort to a minimum. The following sections describe the models that are considered for the simulation of rocket engines within the framework of this thesis.

2.2.1 Navier-Stokes Equations

The characteristic length scales and densities present in conventional chemical rocket engines, allow for the characterization of the flow using the continuum assumption[3]. The

---

[2] In order to increase the accuracy of the calculation, the theoretical value is estimated using 1D numerical calculations based on ideal gas and chemical equilibrium assumptions instead of the simple analytical formula in Eq. (2.6). This is done with NASA's Chemical Equilibrium with Applications (CEA) code [54] for example.

[3] The continuum assumption is not always valid for electric propulsion systems operating at a rarefied regime in which collision and plasma length scales are similar to or even larger

flow can therefore be described using the Navier-Stokes (NS) equations with sufficient accuracy. The NS equations are a set of coupled nonlinear partial differential equations (PDEs) able to describe compressible, viscous three-dimensional (3D) flows. The NS equations in the Euler specification of the flow field (stationary frame) and in integral form read as follows[4]:

$$\frac{\partial}{\partial t}\int_V \rho \, \mathrm{d}V + \int_S \rho \boldsymbol{u}\boldsymbol{n}\mathrm{d}S = 0 \tag{2.9}$$

$$\frac{\partial}{\partial t}\int_V \rho \boldsymbol{u}\mathrm{d}V + \int_S (\rho \boldsymbol{u}\boldsymbol{u})\boldsymbol{n}\mathrm{d}S = -\int_S p\boldsymbol{n}\mathrm{d}S + \int_S \underline{\underline{\tau}}\boldsymbol{n}\mathrm{d}S + \int_V \rho\boldsymbol{F}\mathrm{d}V \tag{2.10}$$

$$\frac{\partial}{\partial t}\int_V \rho E\mathrm{d}V + \int_S (\rho \boldsymbol{u}E)\boldsymbol{n}\mathrm{d}S = -\int_S \boldsymbol{u}p\boldsymbol{n}\mathrm{d}S + \int_S \boldsymbol{u}\underline{\underline{\tau}}\boldsymbol{n}\mathrm{d}S + \int_S (\lambda\nabla T)\boldsymbol{n}\mathrm{d}S + \int_V \rho\boldsymbol{u}\boldsymbol{F}\mathrm{d}V \tag{2.11}$$

where ρ is the density of the fluid, $\boldsymbol{u}$ its velocity, p its pressure, T its temperature and λ its heat conductivity. $\boldsymbol{F}$ represents the external forces applied to the fluid, whereas $\underline{\underline{\tau}}$ is the stress tensor and E the total specific enthalpy of the fluid. V and S represent the volume and the surface of the control fluid in the Euler frame and $\boldsymbol{n}$ is the outward normal vector of the surface.

The system of equations presented in Eqs. (2.9)-(2.11) consists of five equations and has seven unknown flow variables (pressure, density, temperature, energy and the three components of the velocity). The problem is hence under-defined and requires two additional relationships to become well-posed.

This is done by using an equation of state (EOS) to connect the thermodynamic properties. In the case of an ideal gas, the EOS is given by Eq. (2.12), where the pressure is expressed as a function of the density, temperature and composition of the gas.

$$p = \rho RT \sum_{i=1}^{K} \frac{Y_i}{M_i} \tag{2.12}$$

Y_i represents the mass fraction of species i and M_i its molar mass, whereas K stands for the total number of species in the mixture.

---

than the size of the thruster. In such cases, the flow is instead represented by a molecular, kinetic approach [67].

[4] The term "Navier-Stokes equations" strictly describes only the fluid impulse equation [68] but is usually extended to include the continuity and energy equations as well, in the context of CFD [69]. In this thesis, the extended definition is used.

The second equation leading to the closure of the system of equations connects the total specific energy E with the temperature. E is the sum of static enthalpy h and kinetic energy, i.e.:

$$E = h + \frac{1}{2}u^2 \tag{2.13}$$

The closure of the problem occurs by defining the static enthalpy as a function of temperature as shown in Eq. (2.14).

$$h(T) = h_0(T_0) + \int_{T_0}^{T} c_p(T)\mathrm{d}T \tag{2.14}$$

The standard enthalpy of formation is denoted as h_0. When dealing with an ideal gas, the specific heat capacity c_p is assumed to be pressure independent.

The ideal gas assumption is valid for high temperatures and low pressures, where the interaction between the fluid molecules becomes negligible. In rocket engine applications, thermodynamic conditions that do not satisfy the ideal gas assumptions can apply. This is the case when the injection of the propellants occurs at low temperatures and when the operating pressure becomes supercritical. An alternative to the ideal gas EOS has to be implemented in those cases. Two of the alternative equations of state, which can predict the thermodynamic properties in a wider range of temperature and pressure, are the Redlich-Kwong and Peng-Robinson EOS [15]. A further option is the use of tabulated thermodynamic properties, as described in Section 2.2.4, which can be utilized to even predict phase transitions of a fluid, as is the case in cryogenic rocket engines.

For the solution of a CFD problem, the discretization of the system of equations must take place. The numerical discretization in space and time transforms the system of PDEs into algebraic equations. The most commonly used methods for the discretization are the Finite Difference Method (FDM), the Finite Element Method (FEM) and the Finite Volume Method (FVM). All these methods lead to a system of nonlinear algebraic equations, but the efficiency and speed of the solution differs according to the choice of discretization.

Within the framework of this thesis, the solution of the NS equations takes place with the commercial solver ANSYS CFX. CFX utilizes the Finite Volume Method which is extensively described in the literature [16], [17]. The process of the solution of the resulting algebraic equations will not be described in this thesis, since a detailed overview is given in [16].

2.2.2 Turbulence Modeling

The NS equations can be used to describe laminar and turbulent flow fields alike. In order to simulate turbulent flows effectively, different models have been developed, which differ in the way they treat the turbulent scales. The three main representatives are Direct Numerical Simulation (DNS), Large Eddy Simulation (LES) and Reynolds Averaged Navier Stokes (RANS).

In the case of DNS the whole turbulent spectrum is directly calculated and no modeling of the turbulent field is required. All the spatial scales of the turbulence must be resolved in the computational mesh, from the smallest dissipative scales (Kolmogorov microscales), up to the integral scale, associated with the motions containing most of the kinetic energy. This comes of course in the expense of high computational times. For rocket engine applications, associated with high Reynolds numbers, DNS becomes ineffective, since the resolution and hence computational resources rise proportionally to the third power of the Reynolds number [18].

The principal idea behind LES is to reduce the computational cost by splitting the turbulent spectrum into large and small scales. The smallest length scales, which are the most computationally expensive to resolve, are ignored via low-pass filtering of the Navier–Stokes equations. Such a low-pass filtering, which can be viewed as a time- and spatial-averaging, effectively removes small-scale information from the numerical solution. The effect of this information on the flow field is instead modeled, a task which is an active area of research for problems in which small-scales can play an important role. Although efforts are being done in maturing LES up to a level where it can simulate rocket engines with reasonable computational resources [19], [20], it still remains computational expensive for most engineering applications.

The method with the most widespread application in the industry and in the field of rocket engine simulations specifically, is RANS. The idea behind the equations is the decomposition of an instantaneous quantity (velocity, pressure, temperature etc.) into its time-averaged and fluctuating quantities. According to this idea, the NS equations (2.9)-(2.11) are averaged and solved only for the time-averaged quantities. The influence of turbulence is included by modeling the complete turbulence spectrum. This leads to higher computational speeds, but also to a strong dependency of the results on the chosen turbulence model.

Within the present thesis, all CFD calculations are carried out with the commercial solver ANSYS CFX, which uses the RANS equations. The Reynolds averaging process involves decomposing an instantaneous quantity u_i into its ensemble-average $\langle u_i \rangle$ and its fluctuation u_i' according to:

$$u_i = \langle u_i \rangle + u_i'$$ (2.15)

For steady state problems, $\langle u_i \rangle$ can be expressed as:

$$\bar{u}_i = \langle u_i \rangle = \lim_{t \to \infty} \frac{1}{t} \int_0^t u_i(t') \mathrm{d}t'$$ (2.16)

By averaging the NS equations as in [21], they are transformed into Eqs. (2.17)-(2.18) (in differential form).

$$\nabla \cdot \bar{u}_i = 0$$ (2.17)

$$\frac{\partial \bar{u}_i}{\partial t} + \nabla \cdot \left(\bar{u}_i \bar{u}_j \right) + \nabla \cdot \left(\overline{u_i' u_j'} \right) = -\frac{1}{\rho} \nabla \bar{p} + \frac{1}{\rho} \nabla \cdot \bar{\tau}_{ij}$$ (2.18)

The correlation marked in red color in Eq. (2.18) is a tensor of the fluctuation velocities and cannot be obtained by examining the average flow alone. It represents the turbulent fluctuations in fluid momentum and is called Reynolds stress tensor. In order for this system of equations to be closed, special modeling of the term $\overline{u_i' u_j'}$ is needed, which is done by choosing an appropriate turbulence model.

The models for the closure of the RANS equations are divided in the Reynolds Stress Models (RSM) and the Eddy Viscosity Models (EVM). In the first type, a transport equation is solved for the Reynolds stress tensor. This translates to the solution of at least six additional equations thereby increasing the computational cost. The RSM are not considered in this thesis and a detailed description is given in literature [22].

In the case of EVM, the Reynolds stress tensor is modeled similar to the physical stress tensor $\underline{\underline{\tau}}$, by utilizing the analogy between molecular and turbulent processes [22]. The momentum transfer caused by turbulent eddies can be modeled with an eddy viscosity v_t in analogy with how the momentum transfer caused by the molecular motion in a gas can be described by a molecular viscosity. This Boussinesq model[5] reads as follows:

$$\overline{u_i' u_j'} = -2v_t S_{ij} + \frac{2}{3} k \delta_{ij}$$ (2.19)

δ_{ij} is the Kronecker-delta function, S_{ij} the mean rate of the strain tensor given by Eq. (2.20) and k the turbulent kinetic energy defined in Eq. (2.21).

---

[5] The model is named after the French mathematician Joseph Boussinesq who proposed it in 1877.

$$S_{ij} = \frac{1}{2}\left(\frac{\partial \bar{u}_i}{\partial x_j} + \frac{\partial \bar{u}_j}{\partial x_i}\right) \qquad (2.20)$$

$$k = \frac{1}{2}\langle u_i' u_i' \rangle \qquad (2.21)$$

The closure of the RANS equations is hence reduced to the calculation of the eddy viscosity ν_t, which (unlike the molecular kinetic viscosity ν) is not a material property but a quantity of the flow field. This reduction is beneficial for the computational cost, but has the disadvantage of assuming the proportionality between the Reynolds stress tensor and the middle strain rate, which can lead to insufficient modeling of anisotropic effects in the flow.

The Eddy Viscosity Models can be divided to zero-, one- and two-equation models, depending to the number of PDEs that need to be solved for the calculation of ν_t. The most commonly used models in the case of rocket engines are the two-equation models $k - \epsilon$ and $k - \omega$.

In the $k - \epsilon$ model, the two additional equations are the ones for the turbulent kinetic energy k and the eddy dissipation rate ϵ. The model assumes that the turbulence production and turbulence dissipation are in equilibrium and under the assumption of isotropic turbulence, the eddy viscosity takes the form:

$$\nu_t = \frac{C_\mu k^2}{\epsilon} \qquad (2.22)$$

C_μ is a proportionality constant. The two transport equations for k, ϵ have a similar form and consist of five terms: transient, advection, production, diffusion, dissipation [21]. Although the model is stable and more cost efficient than the RSM, it has the disadvantage that the assumption of turbulence isotropy is not satisfied in the boundary layer. For that reason, it does not give accurate results in specific cases close to the wall and it fails to simulate flow separation [21].

The $k - \omega$ model on the other hand solves an equation for k and one for the eddy frequency ω. The eddy viscosity is then defined as:

$$\nu_t = \frac{k}{\omega} \qquad (2.23)$$

This model is able to capture flows close to the boundary layer as well as separation and high pressure gradients. For that reason, the combination of the two models in the form of

the Shear Stress Transport (SST) model is widespread. It combines the benefits of both methods by utilizing the $k - \omega$ in the vicinity of walls and the $k - \epsilon$ in regions where the wall influence is reduced. The SST model is also the one used throughout the simulations presented in the thesis.

The treatment of the walls is important for the estimation of the occurring heat fluxes and viscous stresses. A useful variable for the description of the flow close to the wall boundaries is the y^+, which represents a dimensionless distance from the wall, connected to the physical distance y via:

$$y^+ = \frac{u_\tau}{\nu} y \tag{2.24}$$

The definition uses the friction velocity u_τ:

$$u_\tau = \sqrt{\frac{\tau_w}{\rho}} \tag{2.25}$$

In the present thesis, no wall functions are used for the description of the flow in the boundary layer and instead, the whole regime up to the viscous sublayer is resolved. This requires a finer mesh closer to the walls, in order to ensure that the value of y^+ is close to 1 at the cell adjacent to the wall.

2.2.3 Transport and thermodynamic modeling of mixtures

Within a rocket thrust chamber, the high energy release stemming from the combustion of the propellants, leads to a significant increase of the temperature. This strong change in the thermodynamic state of the fluid has an influence on its transport properties and its heat capacity.

The heat capacity determines the temperature rise of the gas resulting from the released reaction enthalpy. It is hence an important parameter when predicting the temperatures occurring in a combustion chamber or the nozzle of a rocket engine. When dealing with ideal gases, the common approach lies in modeling the temperature dependence of the specific heat capacity, using the NASA polynomials [23]. These consist of 9 parameters implemented for the description of the heat capacity, enthalpy and entropy of a substance as shown in Eqs. (2.26)-(2.28):

$$c_p(T) = \frac{R}{M} (a_1 + a_2 T + a_3 T^2 + a_4 T^3 + a_5 T^4) \tag{2.26}$$

$$h(T) = \int c_p \mathrm{d}T = \frac{R}{M}\left(a_1 T + a_2 \frac{T^2}{2} + a_3 \frac{T^3}{3} + a_4 \frac{T^4}{4} + a_5 \frac{T^5}{5} + a_6\right) \tag{2.27}$$

$$s(T) = \int \frac{c_p}{T} \mathrm{d}T = \frac{R}{M}\left(a_1 \ln(T) + a_2 T + a_3 \frac{T^2}{2} + a_4 \frac{T^3}{3} + a_5 \frac{T^4}{4} + a_7\right) \tag{2.28}$$

Due to the assumption of an ideal gas, the specific heat capacity, enthalpy and entropy do not depend on the pressure of the fluid. For the polynomial parameters, the database of McBride et al. [24] and the one from the GRI 3.0 mechanism [23] are used in this thesis.

When it comes to the transport properties, i.e. the heat conductivity and the dynamic viscosity, the temperature dependence can also have a significant influence when dealing with rocket thrust chambers. Within a rocket engine, turbulent effects can be dominant and determine the mixing, impulse and heat exchange within the gas. For that reason, the molecular heat and impulse exchange (represented by the heat conductivity and dynamic viscosity respectively) become less important. However, in the vicinity of the chamber and nozzle walls, and specifically in the boundary layer, the flow becomes laminar, and turbulent effects are no longer dominant. In this region, the molecular transport properties gain significance and dictate the interaction between the fluid and the structure to a large degree. Therefore, the calculation of the heat flux transferred to the wall requires an accurate knowledge of the heat conductivity and viscosity over a large temperature range. The modeling of these molecular transport properties takes place with the use of an exponential function, defined in McBride et al. [25]:

$$\left.\begin{matrix} \lambda \\ \mu \end{matrix}\right\} = \exp\left(A \ln T + \frac{B}{T} + \frac{C}{T^2} + D\right) \tag{2.29}$$

The parameters $A - D$ can be obtained from the GRI 3.0 mechanism [23] or Svehla [26]. The values used in the present thesis were taken from the GRI 3.0 mechanism as explained in Appendix B.

Apart from predicting the transport properties of the individual species, the calculation of the mixture conductivity and viscosity needs to be addressed. Since the heat flux in the viscous layer close to the wall is determined by the molecular conductivity of the mixture, special mixing rules have to be applied.

ANSYS CFX models the transport properties of a mixture based on a mass-averaging which corresponds to an ideal mixture. In order to account for gas kinetic effects and the interactions between molecules, more complicated mixing rules may need to be implemented.

For the calculation of the mixture's dynamic viscosity μ_{mix}, the model of Wilke [27], extended by the correction from Brokaw [28] is implemented in the in-house CFD code of Airbus Defence and Space "Rocflam3". This model was also applied in ANSYS CFX and examined within the present thesis as shown in Chapter 5. The formula for the viscosity reads as follows:

$$\mu_{mix} = \sum_i^K \frac{X_i \mu_i}{\sum_j X_j F_{ij,Brokaw}} \tag{2.30}$$

where X_i represents the molecular fraction of species i. The definition of the mixing term $F_{ij,Brokaw}$ is given in Eqs. (2.31)-(2.33).

$$F_{ij,Brokaw} = F_{ij} \Phi_{ij} \tag{2.31}$$

$$F_{ij} = \frac{\left[1 + \left(\frac{\mu_i}{\mu_j}\right)^{0.5} \left(\frac{M_j}{M_i}\right)^{0.25}\right]^2}{\sqrt{8\left(1 + \frac{M_i}{M_j}\right)}} \tag{2.32}$$

$$\Phi_{ij} = 1 + \frac{2.41(M_i - M_j)(M_i - 0.142M_j)}{(M_i + M_j)^2} \tag{2.33}$$

The calculation of the mixture's heat conductivity μ_{mix} is done in a similar manner and is given by Eq. (2.34).

$$\lambda_{mix} = \sum_i^K \frac{X_i \lambda_i}{\sum_j X_j F_{ij,Brokaw}} \tag{2.34}$$

2.2.4 Phase change modeling

In the case of gaseous injection of the propellants through the injector, the ideal gas approach described in Section 2.2.1 captures the physical processes adequately. A cryogenic injection of propellants in liquid form, is however common. In the case of supercritical conditions, no evaporation takes place, since the propellant remains above the saturation curve at all times. For subcritical liquids nevertheless, the fluid undergoes evaporation, during which its temperature remains constant and its gaseous phase increases in mass.

A conventional method of simulating evaporation of liquid propellants in a rocket engine is the use of a Lagrange particle tracking module [29]. According to this method, the liquid is

described by discrete droplets with finite size, mass and temperature which interact with the gaseous phase through impulse and heat transfer. The liquid can undergo evaporation and/or boiling, during which part of its mass is transferred to the gaseous phase and is available for chemical reactions with other species. This method was not included in the present work due to the extra modeling effort required, including description of the particles' size distribution, velocity distribution and injection location etc., which was not the topic of the thesis.

Instead, for the modeling task of multiphase flow, two separate methods were introduced for the description of liquid oxygen:

- Constant properties liquid
- Real gas properties (RGP) fluid

In the case of the **constant properties liquid**, no gaseous oxygen is included in the simulation. The LOX is defined as a liquid with constant, temperature independent density, heat capacity, heat conductivity and viscosity values. The benefit of this modeling technique is mainly the very simple implementation, but it comes in the expense of insufficient description of the underlying physics. Specifically, oxygen is assumed to react in liquid form with the gaseous methane, and no phase change is actually taking place in the chamber. Even at temperatures close to 3500 K, oxygen is present only in liquid form, with very high density. This can lead to a lower combustion temperature than the expected one, due to the higher density and heat capacity of the liquid, which requires more energy to heat up. However, the method can still produce meaningful results, because the oxygen is used up in the region close to the injector to a large degree and is present only in small quantities in the rest of the computational domain.

When the fluid is described with the **RGP** model, a table containing the thermodynamic and transport properties of LOX and GOX is implemented. For each point within the thrust chamber, the pressure and temperature values of the flow are utilized, to interpolate the thermodynamic properties of oxygen including density, heat capacity etc. [16]. The oxygen is introduced at a thermodynamic state corresponding to a liquid and hence the appropriate values are accessed in the RGP table. In the computational cells where the combination of temperature and pressure corresponds to a point above the saturation line however (gas regime), the thermodynamic quantities instantly "jump" from the liquid values to the gaseous ones. Hence again, the process of evaporation is not modeled, but its effects (gaseous oxygen in the chamber) are observed.

Further, more complex methods include the Euler/Euler description, where the interface between liquid and gas is resolved. These methods require substantially higher modeling effort and computational power and are mainly compatible with LES or DNS formulations.

2.2.5 Turbulent combustion

Simulating a rocket thrust chamber involves the challenging task of correctly modeling the coupling between turbulence and combustion processes. Combustion requires that fuel and oxidizer are mixed at the molecular level in order for them to react. How this takes place in turbulent combustion depends on the turbulent mixing process.

The general idea describing this phenomenon is that once a range of different size vortices has developed, strain and shear at the interface between the eddies enhance the mixing. According to the energy cascade of turbulent scales, larger eddies break up and the resulting smaller eddies inherit their energy [21]. During the eddy break-up process and the formation of smaller eddies, strain and shear will increase and thereby amplify the concentration gradients at the interface between reactants, which in turn enhances their molecular interdiffusion. The molecular mixing of fuel and oxidizer, as a prerequisite of combustion, therefore takes place at the interface between small eddies.

The difficulty arises from the fact that an interaction between chemical and turbulent scales is inevitable. The heat release during combustion can lead to an increase or even to the damping of turbulence. Eddies on the other hand can either accelerate the chemical reactions or lead them to extinction [30].

The starting point for the formulation of turbulent combustion problems are the NS equations for mass and momentum, the equation for temperature as well as the species equations. The notation used in here is adopted from Peters [31].

$$\frac{\partial \rho}{\partial t} + \nabla \cdot (\rho \boldsymbol{u}) = 0 \tag{2.35}$$

$$\frac{\partial (\rho \boldsymbol{u})}{\partial t} + \nabla \cdot (\rho \boldsymbol{u} \boldsymbol{u}) = -\nabla p - \nabla \cdot \underline{\underline{\tau}} \tag{2.36}$$

The temperature and species equations are formulated with the assumption of equal specific heat capacity and binary diffusivity for all species and constant pressure[6] [31], [32]:

$$\rho \frac{\partial T}{\partial t} + \rho \boldsymbol{u} \cdot \nabla T = \nabla \cdot (\rho \alpha_T \nabla T) + \dot{\omega}_T \tag{2.37}$$

$$\rho \frac{\partial Y_i}{\partial t} + \rho \boldsymbol{u} \cdot \nabla Y_i = \nabla \cdot (\rho D_i \nabla Y_i) + \dot{\omega}_i \tag{2.38}$$

---

[6] These assumptions are made to simplify the equations. ANSYS CFX does not include them in the derivation of the used equations, which leads to additional terms in the right-hand side of each equation [16].

In Eq. (2.37), α_T represents the thermal diffusivity $\lambda/(\rho c_p)$ and D_i in Eq. (2.38) is the binary diffusivity of species i into the mixture. The instantaneous species source term $\dot{\omega}_i$, accounting for the production/reaction of species i as a result of the N_r reactions, is described by:

$$\dot{\omega}_i = M_i \sum_{j=1}^{N_r} \left(v''_{ij} - v'_{ij} \right) \left[\kappa_{F,j} \prod_{k=1}^{K} [C_k]^{r'_{ij}} - \kappa_{B,j} \prod_{k=1}^{K} [C_k]^{r''_{ij}} \right] \tag{2.39}$$

The factors v'_{ij} and v''_{ij} stand for the stoichiometric coefficients of species i in reaction j for the forward and backwards direction respectively[7]. The reaction rates are proportional to the molar concentrations of each species $[C_k]$, raised to the power of the exponent r'_{ij} or r''_{ij}. The rate constants for the forward and backward reaction $\kappa_{F,j}$ and $\kappa_{B,j}$ are modeled according to the Arrhenius ansatz:

$$\kappa_{FB,j} = A_j T^{\beta_j} \exp\left(-\frac{E_{a,j}}{RT} \right) \tag{2.40}$$

The Arrhenius ansatz involves a pre-exponential factor A_j, a temperature exponent β_j and the activation energy $E_{a,j}$ of the reaction j. The temperature source term $\dot{\omega}_T$ is given by Eq. (2.41):

$$\dot{\omega}_T = -\frac{1}{c_p} \sum_{i=1}^{K} h_i \dot{\omega}_i \tag{2.41}$$

In order to solve Eqs. (2.35)-(2.38) using the RANS model, an averaging has to take place. However, the regular Reynolds averaging shown in Section 2.2.2 is only convenient for inert flows. In the case of reacting flows, where large density changes are present and the flow is incompressible, the Favre decomposition is instead chosen [31]. Only the density and pressure are decomposed using the conventional Reynolds averaging, whereas all other variables are Favre-averaged according to Eqs. (2.42)-(2.43):

$$u = \tilde{u} + u'' \tag{2.42}$$

$$\tilde{u} = \frac{\overline{\rho u}}{\bar{\rho}} \tag{2.43}$$

---

[7] With this notation, the equation for the chemical reaction j, can be summarized by $\sum_{i=1}^{K} v'_{ij} C_i \overset{k_f/k_b}{\longleftrightarrow} \sum_{i=1}^{K} v''_{ij} C_i$.
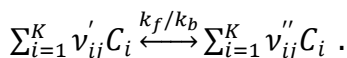
Applying the averaging to the transport equations leads to a new system of equations:

$$\frac{\partial \bar{\rho}}{\partial t} + \nabla \cdot (\bar{\rho} \tilde{\boldsymbol{u}}) = 0 \tag{2.44}$$

$$\frac{\partial (\bar{\rho} \tilde{\boldsymbol{u}})}{\partial t} + \nabla \cdot (\bar{\rho} \tilde{\boldsymbol{u}} \tilde{\boldsymbol{u}}) = -\nabla \bar{p} - \nabla \cdot \underline{\underline{\bar{\tau}}} - \nabla \cdot \left(\overline{\bar{\rho} \boldsymbol{u}'' \boldsymbol{u}''} \right) \tag{2.45}$$

$$\bar{\rho} \frac{\partial \tilde{Y_\iota}}{\partial t} + \bar{\rho} \tilde{\boldsymbol{u}} \cdot \nabla \tilde{Y_\iota} = \nabla \cdot (\overline{\rho D_\iota \nabla Y_\iota}) - \nabla \cdot \left(\overline{\bar{\rho} \boldsymbol{u}'' Y_\iota''} \right) + \overline{\dot{\omega}_\iota} \tag{2.46}$$

$$\bar{\rho} \frac{\partial \tilde{T}}{\partial t} + \bar{\rho} \tilde{\boldsymbol{u}} \cdot \nabla \tilde{T} = \nabla \cdot (\overline{\rho \alpha_T \nabla T}) - \nabla \cdot \left(\overline{\bar{\rho} \boldsymbol{u}'' T''} \right) + \overline{\dot{\omega}_T} \tag{2.47}$$

The colored terms in Eqs. (2.44)-(2.47) require further modeling, in order to complete the closure of the system, since they include contributions from the fluctuations of the flow quantities.

The first term, marked in red color is the equivalent of the Reynolds stress tensor and its closure takes place with the turbulence models described in Section 2.2.2.

The laminar diffusive fluxes of the chemical species and the temperature (green terms) can be neglected in highly turbulent flows, i.e. at large Reynolds numbers. However, they have a big influence in the vicinity of the wall, where turbulent effects disappear. Their modeling in this case takes place according to [30]:

$$\overline{\rho D_\iota \nabla Y_\iota} \approx \bar{\rho} \overline{D_\iota} \nabla \tilde{Y_\iota} \tag{2.48}$$

$$\overline{\rho \alpha_T \nabla T} \approx \frac{\bar{\lambda}}{c_p} \nabla \tilde{T} \tag{2.49}$$

For the blue terms, a closure assumption of first order is implemented, which directly models them using a gradient-diffusion method:

$$\bar{\rho} \overline{\boldsymbol{u}'' Y_\iota''} \approx -\frac{\mu_t}{Sc_t} \nabla \tilde{Y_\iota} \tag{2.50}$$

$$\bar{\rho} \overline{\boldsymbol{u}'' T''} \approx -\frac{\mu_t}{Pr_t} \nabla \tilde{T} \tag{2.51}$$

This introduces two further modeling parameters: the turbulent Schmidt number Sc_t and the turbulent Prandtl number Pr_t. These are defined in Eqs. (2.52)-(2.53).

$$Sc_t = \frac{\mu_t}{\bar{\rho} D_t} \tag{2.52}$$

$$Pr_t = \frac{\mu_t c_p}{\lambda_t} \tag{2.53}$$

These two dimensionless numbers help quantify the turbulent diffusivity D_t and turbulent heat conductivity λ_t. D_t and λ_t are responsible for the mass and heat transfer dominated by turbulence and are not material properties but rather flow quantities. For that reason, the turbulent Schmidt and Prandtl numbers are chosen *a priori* and are set as constants throughout the computational domain, leading to the closure of the system of equations. ANSYS CFX has a built-in assumption about the turbulent Lewis number ($Le_t = Sc_t/Pr_t$), according to which $Le_t = 1$ and hence the Schmidt and Prandtl numbers cannot be chosen independently. This restriction leads to several issues as will be explained in Section 5.2.

Finally, further terms requiring modeling are the temperature and species source terms $\overline{\dot{\omega}_T}$ and $\overline{\dot{\omega}_i}$. These terms are nonlinear and cannot be obtained by the averaged flow quantities $\tilde{T}, \tilde{Y}_i$. Special models like the Eddy Dissipation Model (EDM), which is applied in the case of infinitely fast chemistry, can be utilized to simplify the aforementioned terms. In the case of EDM, it is assumed that the chemical reactions occur much faster than turbulence can mix reactants and heat into the reaction region and hence the mixing alone determines the reaction rate. This way the source terms are calculated by an algebraic function [16].

Other methods are the Equilibrium method which assumes that the chemical equilibrium composition prevails as soon as the reactants mix in the flow. This again has as a prerequisite that the reactions are infinitely fast. An extension of the equilibrium model to include turbulence interaction and flow strain, is the Flamelet model, which is also the topic of the present thesis in the case of nonpremixed combustion and is described in detail in Sections 2.2.6 and 2.2.7.

2.2.6 Nonpremixed turbulent combustion

The majority of the conventional rocket applications with bipropellants involve the fuel and oxidizer entering the combustion chamber separately, where they mix and burn[8]. This gives rise to a process called nonpremixed (or diffusive) combustion. In contrast to premixed flames, nonpremixed flames do not have a characteristic flame speed and hence do not propagate in the direction of the oxidizer or fuel.

---

[8] There are experimental rocket engines in which the oxidizer and fuel are premixed and injected into the chamber as a single fluid. This system architecture simplifies the storage and feeding systems compared to conventional bipropellants and has a better performance (specific impulse) than monopropellants but comes in the expense of potential flashback through the injector [66].

The general description of the nonpremixed combustion involves the mixing process of the oxidizer and the fuel down to molecular level and the consequent chemical reactions between the reactants. The modeling of the reactions with a finite-rate chemistry model can lead to increased computational time depending on the implemented reaction mechanism. A useful description of nonpremixed flames involves reducing the problem only to the mixing of the reactants, by assuming that this is the mechanism that defines the overall time scale of the combustion. This requires the assumption that the chemistry is infinitely fast and hence that the time needed for convection and diffusion during turbulent mixing is much larger than the chemical time. In fact diffusion is indeed the rate-defining process in many nonpremixed applications and this is why these flames are also called "diffusive". This assumption introduces an important simplification, by eliminating all the parameters connected to finite-rate chemical kinetics.

A useful variable when dealing with nonpremixed combustion is the mixture fraction Z. A benefit of introducing this quantity is that the temperature of the gas as well as the source terms and the species mass fraction depend on Z. This way the combustion problem (calculation of $T(\boldsymbol{x},t)$, $Y_i(\boldsymbol{x},t)$) can be reduced to determining the distribution of the mixture fraction in the reaction zone $Z = Z(\boldsymbol{x},t)$, and subsequently transforming back to determine the temperature and species concentrations as in $T(\boldsymbol{x},t) = T(Z)$, $Y_i(\boldsymbol{x},t) = Y_i(Z)$ [30].

Several definitions for the mixture fraction are available in literature [30], [32]. The most general formulation of Z states that it describes the local ratio of the mass flux originating from the fuel feed to the sum of both mass fluxes. By definition, Z is equal to 0 in the oxidizer inlet and 1 in the fuel inlet.

$$Z = \frac{\dot{m}_{fu}}{\dot{m}_{fu} + \dot{m}_{ox}}$$
(2.54)

Another way to express the mixture fraction is based on the chemical elements. The benefit of this formulation lies in the fact that the mass of chemical elements remains constant even after chemical reactions, unlike the mass fraction of chemical species. The mass fraction of element j within the flow is given by Eq. (2.55).

$$Z_j = \sum_{i=1}^{K} a_{ij} Y_i$$
(2.55)

where K is the number of species and a_{ij} the mass fraction of element j in species i. Assuming that the diffusion coefficients of all species are equal ($D_i = D$), the mixture fraction can be given by Eq. (2.56) [32].

$$Z = \frac{Z_j - Z_{j,ox}}{Z_{j,fu} - Z_{j,ox}} \tag{2.56}$$

where $Z_{j,ox}$, $Z_{j,fu}$ refer to the mass fractions at the oxidizer and fuel inlet respectively. A useful definition when dealing with the combustion of hydrocarbons (C_mH_n) is given by Bilger [33]:

$$Z = \frac{\dfrac{Z_C}{mM_C} + \dfrac{Z_H}{nM_H} + 2\dfrac{Y_{O_2,ox} - Z_O}{\nu_{O_2}M_{O_2}}}{\dfrac{Z_{C,fu}}{mM_C} + \dfrac{Z_{H,fu}}{nM_H} + 2\dfrac{Y_{O_2,ox}}{\nu_{O_2}M_{O_2}}} \tag{2.57}$$

ν_{O_2} is the stoichiometric coefficient of oxygen in the one step chemical reaction with a hydrocarbon (Eq. (2.58)):

$$\nu_{fu}C_mH_n + \nu_{O_2}O_2 \rightarrow \nu_{CO_2}CO_2 + \nu_{H_2O}H_2O \tag{2.58}$$
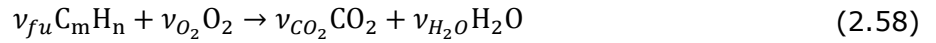
Summing up the equations for the chemical species in Eq. (2.46) according to the rule in Eq. (2.55), leads to a conservation law for the mass fraction of each element j:

$$\rho \frac{\partial Z_j}{\partial t} + \rho \boldsymbol{u} \cdot \nabla Z_j = -\nabla \cdot \left(\sum_{i=1}^{K} \frac{a_{ij}M_j}{M_i} \boldsymbol{j}_i \right) \tag{2.59}$$

The main benefit of Eq. (2.59) is the absence of the source term which is a result of the element mass conservation throughout all chemical reactions. Under the assumption that the diffusion coefficients of all species are equal ($D_i = D$), a conservation equation for the passive scalar Z can be obtained:

$$\rho \frac{\partial Z}{\partial t} + \rho \boldsymbol{u} \cdot \nabla Z = \nabla \cdot (\rho D \nabla Z) \tag{2.60}$$

The implementation of the Favre-averaged mixture fraction equation in ANSYS CFX is shown in Eq. (2.61) using the Einstein notation and the assumption of unity Lewis number [16].

$$\frac{\partial \bar{\rho}\tilde{Z}}{\partial t} + \frac{\partial}{\partial x_i}(\bar{\rho}\tilde{u}_i\tilde{Z}) = \frac{\partial}{\partial x_i}\left(\left(\bar{\mu} + \frac{\mu_t}{\sigma_Z} \right) \frac{\partial \tilde{Z}}{\partial x_i} \right) \tag{2.61}$$

The quantity σ_Z is a modeling constant used in CFX and has the default value of 0.9. The turbulence effects are included by solving the transport equation for the variance of the mixture fraction $\widetilde{Z''^2}$.

$$\frac{\partial \bar{\rho} \widetilde{Z''^2}}{\partial t} + \frac{\partial}{\partial x_i}\left(\bar{\rho}\widetilde{u}_i\widetilde{Z''^2}\right) = \frac{\partial}{\partial x_i}\left(\left(\bar{\mu} + \frac{\mu_t}{\sigma_{Z''^2}}\right)\frac{\partial \widetilde{Z''^2}}{\partial x_i}\right) + \frac{2\mu_t}{\sigma_Z}\left(\frac{\partial \widetilde{Z}}{\partial x_i}\right)^2 - \bar{\rho}\tilde{\chi} \tag{2.62}$$

A further modeling constant $(\sigma_{Z''^2})$ is introduced by ANSYS CFX in Eq. (2.62), which has a default value of 0.9. The last term in the right hand side of Eq. (2.62) represents the dissipation of the mixture fraction variance. The proportionality factor $\tilde{\chi}$, is called scalar dissipation and is defined as in Eq. (2.63).

$$\tilde{\chi} = 2D\left(\frac{\widetilde{\partial Z''}}{\partial x_\iota}\right)^2 \tag{2.63}$$

The scalar dissipation has a similar role in the diffusion of $\widetilde{Z''^2}$, as the dissipation rate ϵ in the diffusion of kinetic energy k. It also serves the purpose of modeling non-equilibrium effects in the combustion. Values of the scalar dissipation close to $\chi = 0\,s^{-1}$ are equivalent to the equilibrium solution, whereas higher values for χ induce a larger departure from equilibrium. This characteristic quantity in the description of nonpremixed turbulent combustion is also able to describe the extinction limit of the flame. When it reaches the critical value χ_q, the non-equilibrium effects are so dominant that quenching of the flame occurs. The influence of the scalar dissipation on the flame temperature and extinction is elaborated in Section 3.1. The modeling assumption implemented in most CFD applications for the calculation of $\tilde{\chi}$, is given by the expression in Eq. (2.64)

$$\tilde{\chi} = C_\chi \frac{\tilde{\epsilon}}{\tilde{k}} \widetilde{Z''^2} \tag{2.64}$$

This empirical correlation is also used in ANSYS CFX and has a proportionality constant $C_\chi = 2.0$.

As already described in this chapter, the formulation of the conservation equations for the mixture fraction and its variance is a significant simplification in the case of nonpremixed flames, since the enthalpy and mass fraction conservation equations do not need to be solved and hence the reaction rate $\bar{\dot{\omega}}$ does not require further modeling.

A specific model, which involves solving the transport equation of mixture fraction combined with a tabulated chemistry for the calculation of the temperature and mass fraction fields, is the so-called Flamelet model, which is extensively described in Section 2.2.7

2.2.7 Flamelet theory

The Flamelet model is the main method for the calculation of nonpremixed turbulent combustion implemented in this thesis. It poses a special model which incorporates finite rate and non-equilibrium effects without solving the computationally expensive equations for the mass fraction of the chemical species. The theory was developed independently by Peters and Kuznetsov [32] and serves as an extension of the classic Burke-Schumann model, by including non-equilibrium effects [31]. This departure from the equilibrium is represented by the scalar dissipation.

A basic requirement for the use of the Flamelet model is the assumption of chemical rates which are faster than the time scales present in the turbulent flow. This corresponds to very large values for the Damköhler number Da, since this is defined as the ratio of chemical τ_R to turbulent macroscopic time scales τ_0:

$$Da = \frac{\tau_0}{\tau_R} \tag{2.65}$$

If this assumption is fulfilled, then the thickness of the reaction zone is thinner than the size of the smallest vortex occurring in the flow field, which typically has the order of magnitude of the Kolmogorov scale [32]. This implies that the vortices are unable to enter the reaction zone and to cause the extinction of the flame, as shown in Figure 2.1.
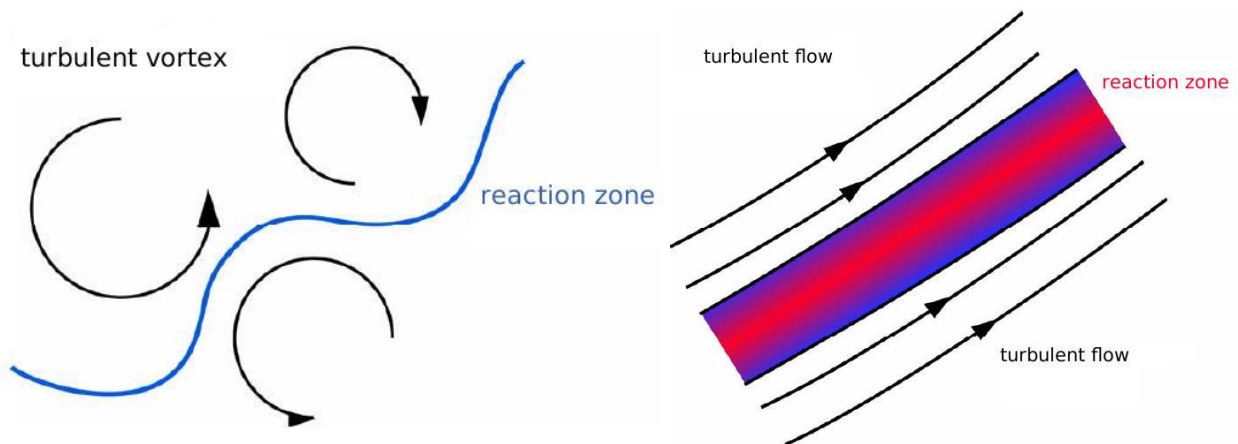
Figure 2.1: Kolmogorov vortex compared to the reaction zone according to the Flamelet theory from Peters [34].

This separation of the two scales, justifies the decoupling of the chemistry calculation from the rest of the flow field. The flame is modeled as an ensemble of small laminar flames, which are called "flamelets". They describe the local structure of the turbulent flame and are coupled to the turbulent flow only by a few parameters: the mixture fraction $\tilde{Z}$, its variance $\widetilde{Z''^2}$ and the scalar dissipation $\tilde{\chi}$. The properties of these flamelets are calculated in a pre-processing step, before the CFD calculation and are stored in libraries. The variables stored in those libraries differ depending on the used CFD solver. In the case of ANSYS CFX, only the mass fractions of the species are tabulated.

The laminar flamelets are located on the iso-surface of the stoichiometric mixture fraction, i.e. at the location $Z(x,t) = Z_{st}$. Including turbulent effects on the structure of the flamelets is done by using a PDF integration, as shown in this section. The CFD solver obtains the mass fraction values from the library, depending on the $\tilde{Z}, \widetilde{Z''^2}$ and $\tilde{\chi}$ values calculated in the flow field. This has great benefits for the computational resources used, since the resulting mass fractions do not need to be repeatedly calculated by solving a transport equation.

A significant step in the Flamelet model lies in creating the table of the species mass fractions as a function of the mixture fraction and the scalar dissipation. Since the table after this first step does not include any effects of turbulence (absence of mixture fraction variance), it is called the laminar table. The method used in the present thesis is utilizing a number of counterflow diffusion flames at different scalar dissipation values in order to fill the table, which will be analytically described in Section 3.1.

ANSYS CFX has a built-in tool called CFX-RIF (Representative Interactive Flamelet), which can be used for the creation of the tables. The governing equations for the temperature and mass fraction which are used for the creation of the laminar table in CFX-RIF result from a coordinate transformation of Eqs. (2.46) and (2.47) in the mixture fraction space, as shown by Peters [32]. For uniform diffusion ($Le = 1$), they take the form of Eqs. (2.66) and (2.67).

$$\frac{\partial T}{\partial t} - \frac{\chi}{2}\frac{\partial^2 T}{\partial Z^2} = \frac{1}{\rho c_p}\sum_{i=1}^{K} h_i\dot{\omega}_i + \frac{\dot{q}_R}{c_p} + \frac{1}{c_p}\frac{\partial p}{\partial t} \tag{2.66}$$

$$\frac{\partial Y_i}{\partial t} - \frac{\chi}{2}\frac{\partial^2 Y_i}{\partial Z^2} = \dot{\omega}_i \tag{2.67}$$

It evident in the Flamelet equations that the mass fraction Y_i is only dependent on the local mixture fraction, which justifies the use of the flamelets-ensemble in the case of fast chemistry [32]. Moreover, the scalar dissipation takes the form of a diffusion constant in the Flamelet equations, since it is proportional to the second order term of the temperature and mass fraction. This correspondence to a diffusion coefficient can be also visualized in the

qualitative plots of Figure 2.2. Here, the temperature and mass fraction profiles are shown as a function of mixture fraction for a nonpremixed methane/air flame. It is evident that a higher value for the scalar dissipation causes the heat to diffuse faster away from the flame, leading to lower temperatures (left subfigure). The same effect in the mass fraction profile causes oxygen to "diffuse" in regions of higher mixture fraction Z.
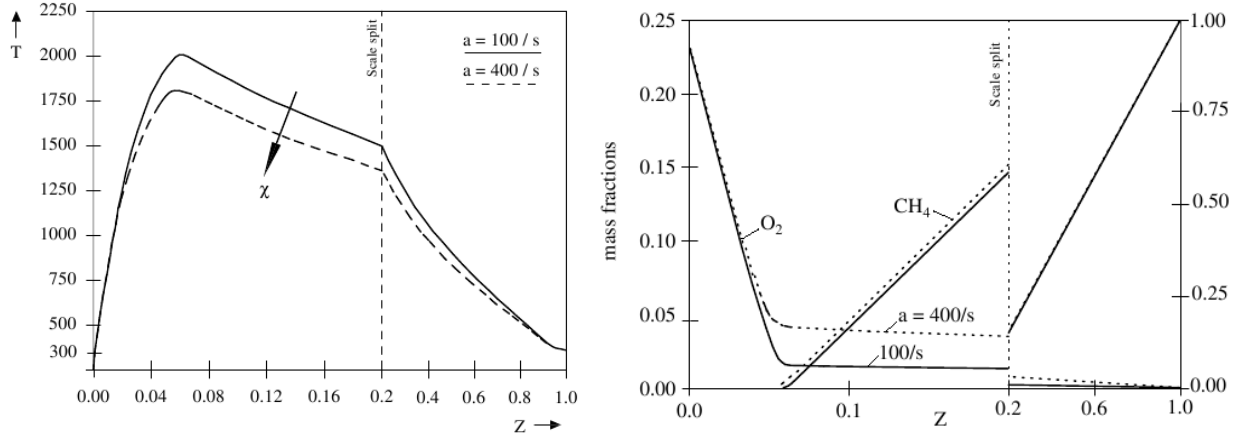
Figure 2.2: Temperature (left) and mass fractions (right) profiles over mixture fraction for different values of the scalar dissipation for a nonpremixed methane/air flame [31].

A scalar dissipation value equal to zero leads to a simplification of the Flamelet Eqs. (2.66) and (2.67). For the steady state case and in the absence of radiation (adiabatic case), they transform to:

$$\dot{\omega}_i = 0 \qquad (2.68)$$

This is also the definition of chemical equilibrium, since no further reactions take place. It is hence seen, how the Flamelet model approaches the equilibrium model in the limit of low dissipation.

The resulting table after the solution of the laminar equations has the form $Y_i = Y_i(Z, \chi)$. In order to predict the influence of turbulence on the chemistry, a Presumed Probability Density Function (PPDF) is implemented in the Flamelet theory. With the assumption of a Probability Density Function (PDF) for the distribution of the mass fractions, an integration takes place, which results in the Favre-averaged species fractions $\tilde{Y}_i$.

$$\tilde{Y}_i\big(\tilde{Z}, \widetilde{Z''^2}, \tilde{\chi}\big) = \int\limits_0^\infty \int\limits_0^1 Y_i(Z, \chi) \cdot P(Z, \chi)\, \mathrm{d}Z \mathrm{d}\chi \qquad (2.69)$$

The prediction of a fitting PPDF can be very difficult, especially since it includes a coupling between the influences of Z and χ for each value of the variance $\widetilde{Z''^2}$. A widely used method which simplifies the modeling is decoupling the two effects, leading to:

$$P(Z,\chi) = P(Z) \cdot P(\chi) \tag{2.70}$$

ANSYS CFX has an implemented Dirac function for $P(\chi)$ and a β-PDF for $P(Z)$. The Dirac function is simply given by Eq. (2.71):

$$P(\chi) = \delta(\chi - \tilde{\chi}) \tag{2.71}$$

and hence the integration over χ (for a specific value $\tilde{\chi}$) leads to:

$$\tilde{Y}_i\big(\tilde{Z}, \widetilde{Z''^2}, \tilde{\chi}\big) = \int_0^\infty \int_0^1 Y_i(Z,\chi) \cdot P(Z) \cdot P(\chi)\, \mathrm{d}Z \mathrm{d}\chi = \int_0^1 Y_i(Z,\tilde{\chi}) \cdot P(Z)\, \mathrm{d}Z \tag{2.72}$$

The β-PDF is very flexible since it changes its form for different values of the mixture fraction and its variance. Its form is defined by Eqs. (2.73), (2.74) and (2.75), in which Γ represents the gamma-function [35].

$$P(Z) = \frac{Z^{\alpha-1}(1-Z)^{\beta-1}}{\Gamma(\alpha)\Gamma(\beta)}\Gamma(\alpha+\beta) \tag{2.73}$$

$$\alpha = \tilde{Z}\left(\frac{\tilde{Z}\big(1-\tilde{Z}\big)}{\widetilde{Z''^2}} - 1\right) \tag{2.74}$$

$$\beta = (1-\tilde{Z})\left(\frac{\tilde{Z}\big(1-\tilde{Z}\big)}{\widetilde{Z''^2}} - 1\right) \tag{2.75}$$

Another widely used PPDF ansatz is the Gaussian PDF, which is defined by Eq. (2.76). Compared to the β-PDF however, it demonstrates a decreased flexibility.

$$P(Z) = \frac{1}{\sqrt{2\pi\widetilde{Z''^2}}}\exp\left(-\frac{\big(\tilde{Z} - \widetilde{Z''^2}\big)^2}{2\widetilde{Z''^2}}\right) \tag{2.76}$$

Since the integration process can be time-consuming when performed during runtime at every iteration, it is done during pre-processing and hence the already integrated values $\tilde{Y}_i\big(\tilde{Z}, \widetilde{Z''^2}, \tilde{\chi}\big)$ are stored in the Flamelet library and called by the CFD code.

The complete process of a premixed combustion simulation in ANSYS CFX using the RIF model is illustrated in Figure 2.3. The CFD code calculates the flow properties in the domain, namely the velocity, pressure, the turbulence variables, the mixture fraction and its variance as well as the scalar dissipation. With the information of the load point (oxidizer and fuel temperatures, pressure) as well as the local properties of the mixture $(\tilde{Z}, \widetilde{Z''^2}, \tilde{\chi})$, the averaged mass fractions $\tilde{Y}_i$ can be obtained. The flow chart demonstrates the whole process of creating the laminar table $Y_i(Z)$ using the Flamelet code and the following PDF integration for clarity. However, these steps take place during pre-processing and not during runtime to reduce the computational resources and hence the $\tilde{Y}_i$ values are simply interpolated from the Flamelet table. Using the mass fractions, the enthalpy of the mixture is obtained. In order to calculate the temperature of the gas given its enthalpy, Eq. (2.14) is implemented, which however includes a temperature-dependent expression for the specific heat capacity c_p. For that reason, an iterative process is utilized, which also leads to a result for the averaged density, according to the equation of state [32]. Other codes avoid the iterative calculation of the temperature, by tabulating the temperature as well, since it results from the solution of the Flamelet equations, just like the mass fractions.
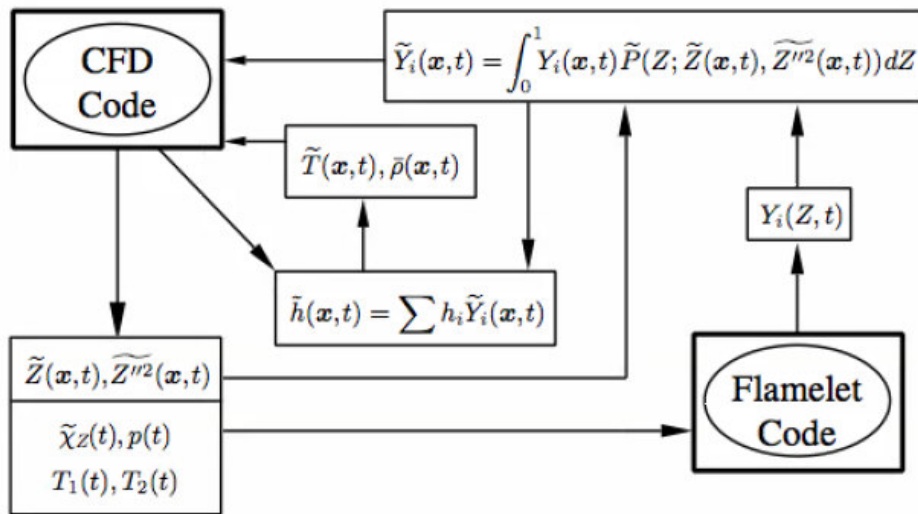
Figure 2.3: Flow chart of a premixed combustion simulation in ANSYS CFX using a Flamelet model and a presumed PDF for the turbulence interaction from Peters [32].

Different methods for creating the Flamelet tables can be implemented. The CFX-RIF module solves the Flamelet Eqs. (2.66) and (2.67) and then performs a PDF integration. The process utilized in the present thesis is however different and based on the solution of the counterflow diffusion flame equations to create the Flamelet tables as described in Chapter 3.

3 Generating Flamelet tables with Cantera

The goal of this thesis is the development, validation and optimization of a Flamelet table generator, able to operate with the rocket fuel combination of methane and oxygen. The resulting Flamelet tables shall be used in 3D-CFD calculations of rocket thrust chambers using the simulation tool ANSYS CFX. The format of the tables therefore has to be compatible with CFX. This implies that the table is three-dimensional and within it the averaged mass fractions $\tilde{Y}_i$ of all chemical species involved in the reactions are listed as a function of the mixture fraction $\tilde{Z}$, the mixture fraction variance $\widetilde{Z''}$ and the scalar dissipation rate $\tilde{\chi}$ for a specific load point.

The method utilized in this thesis for the Flamelet table generation is the solution of 1D counterflow diffusion flames. The theoretical details of this process are given in Section 3.1. For the solution of the counterflow diffusion flame, the open source chemistry tool Cantera is utilized, which is presented in Section 3.2. The process of generating the Flamelet tables is divided in two separate steps, which are schematically summarized in Section 3.3: First, the laminar table is generated by solving multiple instances of the counterflow diffusion flame problem. The practical implementation of this procedure in Python and Cantera is outlined in Section 3.4. The second step in the Flamelet table generation is the PDF integration in order to include the effects of turbulence as described in Section 3.5. Finally, a comparison of the Cantera tool and the CFX-RIF module is given in Section 3.6. A detailed overview of the user manual for the Flamelet generator is given in Appendix H.

3.1 Counterflow diffusion flames

Counterflow diffusion flames are a type of stagnation flows, where an oxidizer inlet and a fuel inlet are placed opposite to each other as shown in Figure 3.1. The two streams are decelerated because of their interaction downstream of their respective inlets, until a stagnation plane is reached. The position of this stagnation plane is dependent on the mass flux (density and velocity) of the two fluids. The reactions between fuel and oxidizer give rise to a stationary flame, whose location does not necessarily coincide with the stagnation plane. The flame is located at the plane where the mixture ratio has its stoichiometric value, i.e. at the point where $Z = Z_{st}$. In most conventional rocket fuel combinations, the stoichiometric O/F is bigger than 1 ($Z_{st} > 0.5$) and hence the flame location is closer to the oxidizer inlet. This is also the case for methane-oxygen combustion, where $Z_{st} = 0.2$. Another important location is the one of the maximal temperature. For flames close to equilibrium, this point is equivalent to the stoichiometric point. However, when a non-

equilibrium flame is examined, the point of maximum temperature departs from the location with $Z = Z_{st}$.
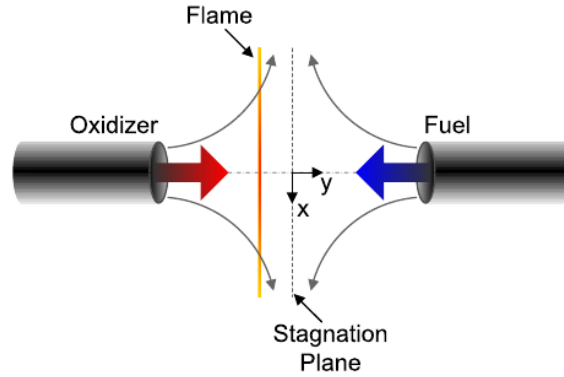
Figure 3.1: Illustration of a counterflow diffusion flame.

A main benefit of the counterflow diffusion flames is that the complex 3D flow problem can be reduced to a set of 1D equations, which describe the problem exactly [32]. This leads to a significant decrease of the computational effort and allows for the implementation of complex reaction mechanisms which would be very costly in a 2D or 3D simulation. Moreover, due to their 1D nature, they can be used to describe the laminar structure of Flamelets. Herein lies the essence of using the counterflow flames in Flamelet library generation applications. By modifying the inlet boundary conditions of the problem, a different degree of "non-equilibrium" is introduced, which is represented by a different value of the scalar dissipation rate χ.

The counterflow diffusion flame problem can be characterized by a single variable, namely the strain rate α, which serves as a time scale representative of the problem [32], [36]. Different definitions are available for α, including the maximum or the average velocity gradient in the flow field. The strain rate can also be expressed as the average velocity gradient at the stoichiometric point or by the velocity gradient in the oxidizer-rich side, due to the assumption of a potential flow [32], [37], [38]. It has been shown however that all definitions are nearly proportional to each other [39]. Within the frame of the present thesis, following expression has been adopted from Law [36]:

$$\alpha = \frac{u_{ox}}{L}\left(1 + \frac{u_{fu}\sqrt{\rho_{fu}}}{u_{ox}\sqrt{\rho_{ox}}}\right) \tag{3.1}$$

In Eq. (3.1) u_{ox} and u_{fu} represent the velocities of oxidizer and fuel respectively, whereas L stands for the distance between the two inlets. This definition takes into account the different densities of oxidizer (ρ_{ox}) and fuel (ρ_{fu}) which is relevant for CH_4/O_2 and H_2/O_2 flames, where the oxidizer is much denser than the fuel.

The large number of different definitions for the strain rate poses the main source of uncertainty when comparing between different counterflow diffusion flames, due to the inconsistency observed in literature [36].

CFD implementations of the Flamelet model do not require calculation of the strain rate, since this is a value representative only for the counterflow diffusion flame problem. Instead, CFD solvers include the scalar dissipation rate χ in their solution as explained in Eq. (2.64). For that reason, in order to enable the cross reference between the solution of the counterflow flame and the table imported in the CFD solver, the strain rate value must be transformed to an equivalent scalar dissipation. The expression implemented in this thesis is defined by Kim et al. [40] and takes into account the different densities of oxidizer and fuel:

$$\chi = \frac{\alpha}{2\pi} \frac{\left(2\sqrt{\frac{\rho_{ox}}{\rho_{st}}} + 1\right)}{3\left(\sqrt{\frac{\rho_{ox}}{\rho_{st}}} + 1\right)^2} \frac{1}{\exp(2 \cdot [\mathrm{erfc}^{-1}(2 \cdot Z_{st})]^2)} \tag{3.2}$$

In Eq. (3.2), ρ_{st} is the density at the stoichiometric point and erfc^{-1} the inverse error function. The variable χ represents the degree of departure from chemical equilibrium and is also a characteristic time scale of the combustion problem. The correct estimation of the scalar dissipation is crucial not only for Flamelet applications but also in experimental investigations of laminar flames. Counterflow diffusion flames are very often used experimentally because they represent an essentially one-dimensional flame structure and can therefore give insight into the combustion process of different fuel combinations. In those experimental configurations, a common practice involves performing the counterflow test multiple times, for increasing value of the strain rate or equivalently of the scalar dissipation. This allows examining the dependence of the maximal temperature occurring in this laminar flame on the applied scalar dissipation.

The influence of χ in the combustion process can be understood by examining Eqs. (2.66) and (2.67), where the scalar dissipation occurs as a proportionality constant similar to a diffusion coefficient. Hence, χ can be thought of equivalently as the rate at which heat diffuses away from the flame. A higher scalar dissipation implies that the heat diffuses faster away from the reaction zone and therefore leads to smaller temperature values. After a specific value for χ, the heat dissipates away faster than the reactants are supplied to the reaction zone, and hence the flame extinguishes. This point is called quenching point and the corresponding value for the dissipation rate is denoted as χ_q. A qualitative illustration of this effect can be seen in Figure 3.2, where the quenching point has also been marked.
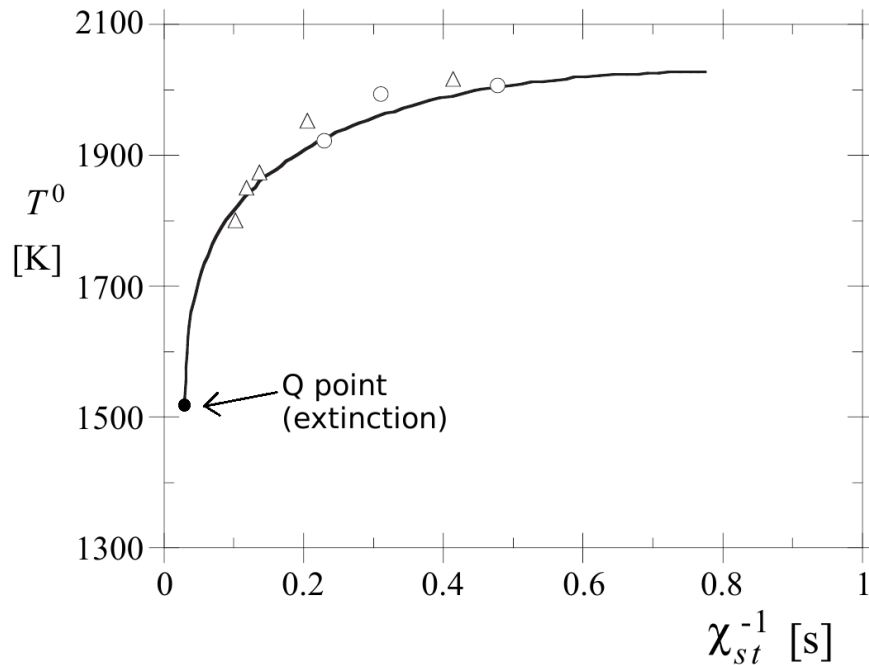
Figure 3.2: Dependence of the maximal flame temperature T⁰ in a nonpremixed methane/air flame on the inverse of the scalar dissipation rate [32].

3.2   Cantera

For the generation of the Flamelet tables, the counterflow diffusion flame problem has to be solved. In order to simulate the flow in this 1D problem, the software Cantera has been utilized. Cantera is a set of object-oriented software tools for problems involving chemical kinetics, thermodynamics, and/or transport processes [38]. It was developed by David G. Goodwin at the California Institute of Technology and allows a user interface with Python and Matlab scripts, or with codes written in C++ and Fortran 90, whereas the code's kernel itself is written in C++ [41]. An overview of the internal structure involved in Cantera is schematically illustrated in Figure 3.3. The work presented in this thesis was carried out with the use of the Python Extension Module.

The flexibility of the software allows it to perform different types of calculations ranging from thermodynamic and transport properties to chemical equilibrium calculations, one-dimensional flames, reaction path diagrams and reactor networks. Within the frame of this thesis, the most relevant module is the one involving the solution of axisymmetric flame problems, which includes the counterflow diffusion flame. Details about the other modules and the internal domain structure of Cantera are given in [42].
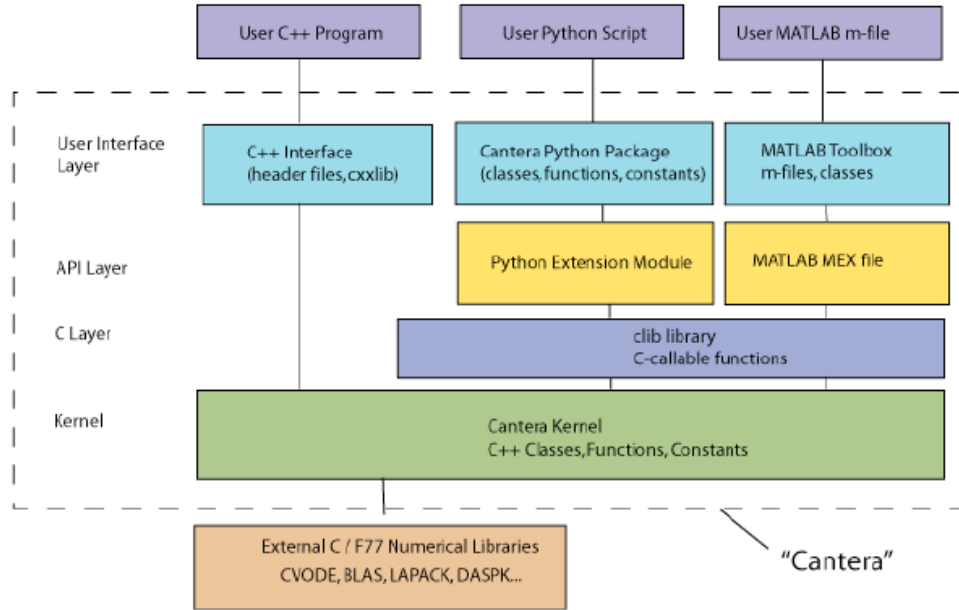
Figure 3.3: Internal structure of the Cantera software from Goodwin [41].

3.2.1 Conservation laws

For the simulation of a counterflow diffusion flame, Cantera uses an axisymmetric flow domain called "AxisymmetricFlow". Within this domain, a 1D grid is set up and at each grid point, $K + 4$ variables are solved for, where K represents the number of species being modeled in the combustion process:

- Axial velocity u
- Scaled radial velocity V
- Temperature T
- Pressure curvature Λ
- Species mass fractions Y_i ($i = [1, K]$)

The scaled radial velocity is defined as a function of the radial velocity v and the radial coordinate r:

$$V = \frac{v}{r} \tag{3.3}$$

The pressure curvature Λ on the other hand is given by Eq. (3.4)

$$\Lambda = \frac{1}{p} \cdot \frac{\mathrm{d}p}{\mathrm{d}r} \tag{3.4}$$

35

The system of equations for the solution of the problem can be simplified to a set of Ordinary Differential Equations (ODEs) along the spatial axial coordinate x for the solution of the mass continuity, the momentum and energy conservation as well as the species transport [32], [42].

Continuity equation:

$$\frac{\mathrm{d}}{\mathrm{d}x}(\rho u) + 2\rho V = 0 \tag{3.5}$$

Radial momentum equation:

$$\rho \frac{\mathrm{d}V}{\mathrm{d}t} = \frac{\mathrm{d}}{\mathrm{d}x}\left(\mu \frac{\mathrm{d}V}{\mathrm{d}x}\right) - \Lambda - \rho u \frac{\mathrm{d}V}{\mathrm{d}x} - \rho V^2 \tag{3.6}$$

Energy equation:

$$\rho c_p \frac{\mathrm{d}T}{\mathrm{d}t} = \frac{\mathrm{d}}{\mathrm{d}x}\left(\lambda \frac{\mathrm{d}T}{\mathrm{d}x}\right) - \rho c_p u \frac{\mathrm{d}T}{\mathrm{d}x} - \sum_i M_i \dot{\omega}_i h_i - \sum_i j_i c_{p,i} \frac{\mathrm{d}T}{\mathrm{d}x} \tag{3.7}$$

Species equation:

$$\rho \frac{\mathrm{d}Y_i}{\mathrm{d}t} = -\rho u \frac{\mathrm{d}Y_i}{\mathrm{d}x} - \frac{\mathrm{d}j_i}{\mathrm{d}t} + M_i \dot{\omega}_i \tag{3.8}$$

Λ is an eigenvalue of the problem, which remains constant throughout the domain [42].

In Eq. (3.8), j_i represents the diffusion flux of species i into the mixture and can be expressed according to Fick's first law [43]:

$$j_i = -\rho \frac{M_i}{\overline{M}} D_{im} \frac{\mathrm{d}X_i}{\mathrm{d}x} \tag{3.9}$$

The average molar mass of the mixture is denoted as $\overline{M}$, whereas the diffusion coefficient of species i into the mixture is represented by D_{im}.

The closure of the system (3.5)-(3.8) takes place with the implementation of a suitable equation of state. Cantera uses the ideal gas equation of state in order to connect the pressure, density and temperature of the gas mixture, as shown in Eq. (3.10):

$$p = \rho RT \sum_{i=1}^{K} \frac{Y_i}{M_i} \tag{3.10}$$

It has been demonstrated that including real gas effects in the calculation of Flamelet tables does not induce significant differences in the mass fraction and temperature profiles [44], [45]. For that reason the assumption of ideal gas which is implemented in Cantera, can be utilized without compromising the accuracy of the tabulated mass fraction results. The exclusion of real gas effects does not extend however to the actual CFD calculations that the Flamelet tables are used in. Especially for higher pressures and/or low propellant temperatures, real gas effects cannot always be neglected when simulating the combustion processes in the rocket thrust chamber.

It is important to mention, that a limitation of Cantera is its inability to perform calculations for inlet temperatures lower than 200 K. Cantera utilizes the ideal gas approach and for the lower temperature limit, where this assumption departs from the real gas behavior, the solver fails to converge. This implies that for the use of Cantera in Flamelet table generation calculations, the temperature at the inlet has to be modified, to ensure that it does not drop below the limit of 200 K.

3.2.2 Thermodynamic, transport and kinetic properties

For the solution of the conservation laws in Eq. (3.5)-(3.8), the temperature dependent value of the specific heat capacity $c_{p,i}$ is required. This occurs by applying the NASA-polynomials, which are described in Section 2.2.3.

Apart from the thermodynamic properties, the transport properties of the mixture (μ, λ, D_{im}) require proper modeling in order to accurately predict the flux of impulse, heat and mass through the system. Cantera makes use of the kinetic theory of gases in order to model these coefficients at different load points and gas compositions.

The viscosity of a single component (μ_i) is expressed according to the Chapman-Enskog theory [43]:

$$\mu_i = \frac{5}{16} \frac{\sqrt{\pi m_i\, k_B T}}{\pi \sigma_i^2 \Omega^{(2,2)}} \tag{3.11}$$

In Eq. (3.11) m_i stands for the molecule mass, σ_i for the collision diameter in the Lennard-Jones potential and $\Omega^{(2,2)}$ for the reduced collision integral. $\Omega^{(2,2)}$ is a function of the reduced temperature $T^* = k_B T/\epsilon_i$, with ϵ_i being the well depth of the intermolecular Lennard-Jones potential-energy curve.

The resulting dynamic viscosity of the mixture is determined by the Wilke mixing rule [46] and is then used for the solution of Eq. (3.6):

$$\mu = \sum_i \frac{\mu_i X_i}{\sum_j \Phi_{ij} X_j} \tag{3.12}$$

$$\Phi_{ij} = \frac{\left[1 + \sqrt{\frac{\mu_i}{\mu_j} \sqrt{\frac{M_j}{M_i}}} \right]^2}{\sqrt{8} \sqrt{1 + \frac{M_i}{M_j}}} \tag{3.13}$$

A similar expression is derived for the heat conductivity:

$$\lambda_i = \frac{25}{32} \frac{\sqrt{\pi m_i k_B T}}{\pi \sigma_i^2 \Omega^{(2,2)}} \frac{c_v}{m_i} \tag{3.14}$$

c_v is the specific heat at constant volume. For a mixture, the resulting conductivity takes the form of Eq. (3.15).

$$\lambda = 0.5 \left(\sum_i X_i \lambda_i + \frac{1}{\sum_i \frac{X_i}{\lambda_i}} \right) \tag{3.15}$$

Finally, the diffusion coefficient of species i into the mixture is expressed by Eq. (3.16):

$$D_{im} = \frac{1 - Y_i}{\sum_{j \neq i} \frac{X_j}{D_{ji}}} \tag{3.16}$$

The binary diffusion coefficients D_{ji} are given by the Chapman-Enskog theory [43] as well:

$$D_{ji} = \frac{3}{16} \frac{\sqrt{2\pi \frac{k_B^3 T^3}{m_{ji}}}}{p\pi \sigma_{ji}^2 \Omega^{(1,1)}} \tag{3.17}$$

In Eq. (3.17) $\Omega^{(1,1)}$ represents a reduced collision integral, which is a function of the reduced temperature $T_{ji}^* = k_B T / \epsilon_{ji}$ where:

$$\epsilon_{ji} = \sqrt{\epsilon_j \epsilon_i} \tag{3.18}$$

Other important factors from Eq. (3.17) are defined in Eq. (3.19).

$$m_{ji} = \frac{m_j m_i}{m_j + m_i}, \qquad \sigma_{ji} = \frac{\sigma_j + \sigma_i}{2} \tag{3.19}$$

The species production rate $\dot{\omega}_i$ is modeled by means of finite rate chemistry. This is in fact the main benefit of the Flamelet model. Given the 1D character of the flame problem, a complex reaction mechanism can be used, which would be too costly in a 2D/3D CFD application. A list of the included species and reactions has to be provided in order to model the production rate $\dot{\omega}_i$ in Eq. (3.5)-(3.8). Different reaction mechanisms were compared within the framework of this thesis, but the GRI 3.0 mechanism was eventually chosen for the calculations [23]. GRI 3.0 is an optimized mechanism designed to model natural gas combustion and hence provides good results for the combustion of methane. It contains 53 species and 325 reactions, which are described in Appendix A.

It is hence evident, that for the solution of the counterflow diffusion flame, Cantera requires a significant input of thermodynamic, transport and kinetic parameters. In order to simplify the input process, Cantera allows the definition of the reaction mechanism as well as the species' thermodynamic and transport properties based on the widely used CHEMKIN format. CHEMKIN is a proprietary software tool for solving complex chemical kinetics problems [47]. Among other functions, it can be used to generate files describing kinetic, thermodynamic and transport properties of mixtures. Three separate files stemming from CHEMKIN are required to completely describe a mixture in Cantera:

- Reaction mechanism file containing the elements, species and chemical reactions
- Thermodynamic file containing the factors of the NASA polynomials for each species
- Transport file containing the values of ϵ_i, σ_i and other gas-kinetic properties

Cantera transforms the three files into a .cti file which summarizes all the information required to completely define the properties of the mixture. This file can then be used to create an instance of the gas used in the counterflow diffusion problem.

3.2.3 Numerical solution of the ODEs

The conservation laws (3.5)-(3.8) are discretized based on a finite difference method, according to which the differential equations are approximated with the Taylor expansion

theorem and transformed into a system of nonlinear algebraic equations [42]. The convective terms are approximated with an Upwind Differencing Scheme (UDS), whereas the diffusive terms are approximated with a second order Central Differencing Scheme (CDS) [18], [42].

When dealing with a finite-rate chemistry model and an extensive mechanism, a large number of species and reactions can potentially be included (53 species and 325 reactions in the case of GRI 3.0). The reaction rates of the individual reactions usually demonstrate differences of several orders of magnitude, leading to a numerically stiff system of equations which can lead to numerical instability [43]. The solution of this system hence requires special numerical treatment.

Cantera utilizes a hybrid damped Newton/time-stepping algorithm to solve the equations. By using an implicit discretization method for the transient terms of Eqs. (3.5)-(3.8), the robustness of the time-stepping method is combined with the fast convergence character of the Newton method. First, the Newton method tries to find the steady-state solution of the system. If this fails, then a pseudo-transient problem with much larger domain of convergence is attempted. By taking a few time steps, the transient algorithm tries to find a solution within the domain of convergence of the steady state solution. After the time steps have been carried out, the steady solution is attempted again and the process is iterated until the code converges. This process is described extensively in Goodwin [42] and is illustrated in Figure 3.4.

Finally, the grid on which the equations are being solved can be adaptively refined to resolve the profiles or coarsened to remove unnecessary points. The user has direct influence on the grid adaptation criteria as well as the convergence tolerance [48].
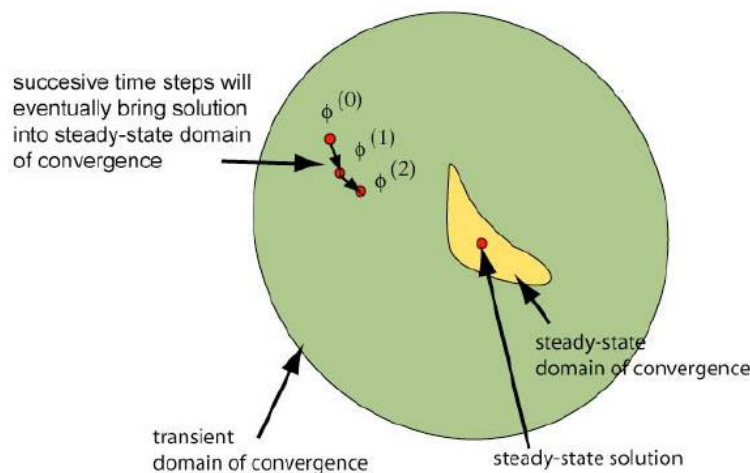
Figure 3.4: Domain of convergence of transient and steady state Newton method from Goodwin [42].

3.3 Description of the calculation process

The process of generating the Flamelet tables with the Python/Cantera interface and then using them for CFD calculations is described in Figure 3.5. Solving the 1D counterflow diffusion flame problem for different values of the scalar dissipation rate results in the laminar tables in the form of the species mass fraction distribution $Y_i(Z, \chi)$.

The integration of the tables takes place in Python and results in the species tables containing the effect of turbulence $\tilde{Y}_i\big(\tilde{Z}, \widetilde{Z''^2}, \tilde{\chi}\big)$. This table comprises the final Flamelet library, which is imported in the CFD solver.

After the two steps of pre-processing are carried out, the simulation of the flow field in the rocket thrust chamber can take place, using the commercial solver CFX. In each iteration the species mass fractions stored in the Flamelet table are accessed, using as an input the values of the mixture fraction, its variance and the scalar dissipation rate.

In the following sections (3.4 and 3.5), the code implementation of the two the pre-processing steps is described in detail.

Figure 3.5: Schematic flow chart of the calculation process using Python and Cantera for the Flamelet table generation and ANSYS CFX for the CFD solution (modified from Müller et al. [49]).

3.4 Generating the laminar table

The timeline of the calculation process for the generation of the laminar table is presented in Figure 3.6 in the form of a flow chart.
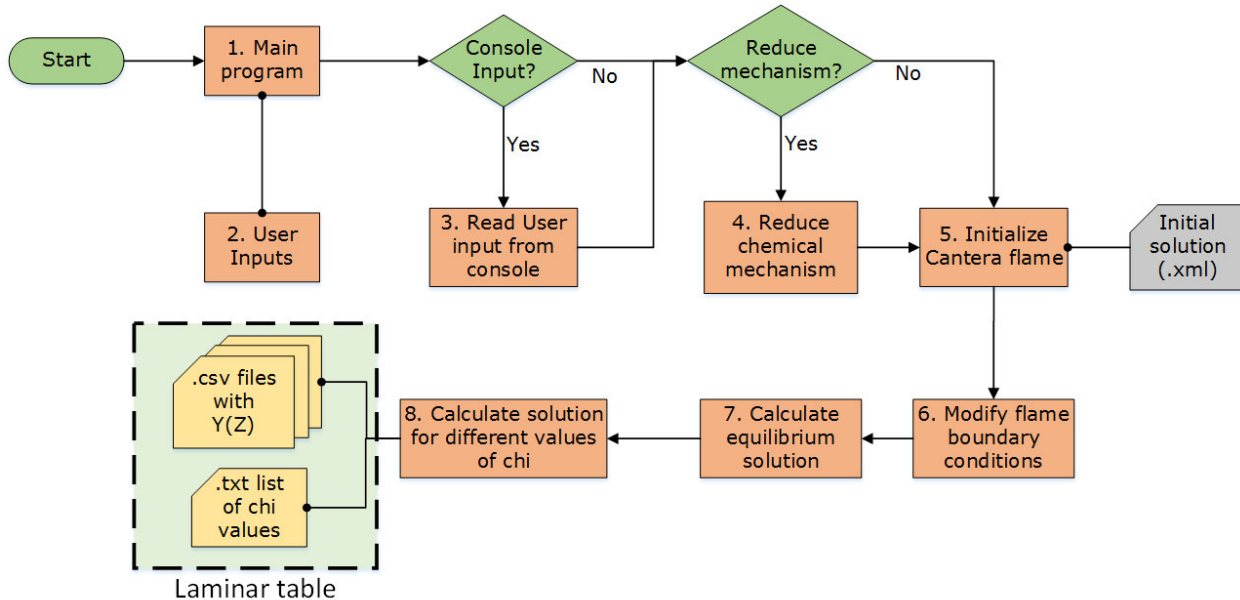
Figure 3.6: Flow chart of the laminar table generation.

The execution of the table generation begins by starting the main program. This calls all subsequent functions and loads the required input data. This is marked by **"1. Main program"** in the flow chart. The main program is a Python script called Flamelet_tabellengenerator.py (see Appendix H). All the steps described in this section are carried out in Python, utilizing the Cantera/Python interface where necessary.

3.4.1 User Inputs

The first part of the code lies in loading the user inputs for the calculation and is denoted as **"2. User Inputs"** in Figure 3.6. This is done by loading a Python script called User_Inputs.py, which contains the definitions of several parameters that are used in the course of the calculation. As explained in Appendix H, the user has to fill out the suitable values for each of these parameters. These include:
- The boundary conditions of the flame (temperature of oxidizer and fuel at inlets, operating pressure, gas composition at inlets)
- The path of the initial solution file
- Control over the reaction mechanism (path of the reaction mechanism file, species to be excluded, reduction method for the mechanism)
- Control over the output Flamelet table (type of PDF integration, name of the table)
- Parameters controlling the CCL output used in the ANSYS CFX (should a CCL be produced, name of file etc.)

The user has a complete influence of the basic parameters used in the generation of the Flamelet table, and they are all accessible through this Python script.

In case the user does not wish to fill the information about the boundary conditions in the Python script (by indicating so according to the instructions in Appendix H), a console input is made available. In this step (**"3. Read User input from console"**), the user can specify the inlet temperature, pressure and composition using the Python window directly. The code makes sure that the inlet temperature given by the user is higher than 200 K and that the sum of the mass fractions adds up to 1 or otherwise requests the inputs again.

3.4.2 Reduction of the reaction mechanism

In the user input definition, it is possible to indicate whether the used chemical reaction mechanism should be simplified or not. In case the user requests a simplified mechanism, the following process is carried out (**"4. Reduce chemical mechanism"** in Figure 3.6):

The gas in the oxidizer and fuel inlets consists of a mixture, which can include any of the species described by the chemical reaction mechanism. In the case of detailed mechanisms like the GRI 3.0, nitrogen and nitrogen-based species are also modeled. This is especially beneficial when dealing with rocket engines operating with LNG, since the same reaction mechanism can be utilized as in the case of pure methane combustion. In most rocket engine applications however, nitrogen is not necessarily present in the fuel mixture. In those cases, solving the counterflow diffusion flame problem, while using the complete reaction mechanism, would increase the computational cost without improving the accuracy of the calculation. Although all the nitrogen-based species would have a mass fraction equal to zero, their transport equations would still have to be solved.

In the present Flamelet table generation code, the program can identify, whether nitrogen is present in one of the two inlets. If this is the case, then the unaltered, complete reaction mechanism is used. If however no nitrogen is injected at the inlet, the reactions containing nitrogen as well as the respective species are deleted, and the reduced mechanism is used for the calculation. Taking as an example the GRI 3.0 mechanism, removing nitrogen leads to 217 reactions and 35 species (compared to 325 reactions and 53 species unmodified).

The same procedure is implemented for carbon as well. Although the code is designed for the simulation of methane/oxygen combustion, it has been constructed in a modular way, to allow for the calculation of hydrogen/oxygen combustion as well. For that reason, in case no carbon is detected in the inlets, all reactions and species containing carbon are removed.

The user also has the ability to indicate specific species that should be excluded from the reaction mechanism. This is especially useful when the influence of some intermediate

species on the final solution is to be examined. When this is the case, all reactions containing the listed molecules are removed from the mechanism.

3.4.3 Initializing the flame

Using the finalized reaction mechanism, a flame element can be defined in Cantera. In order to accelerate the solution, the flame domain is initialized with an already calculated flame. This is done by loading an existing flame configuration (in the form of an .xml) file, into the created flame element. Any solution can serve as an initial condition. Of course, the closer the initial solution is to the desired working point, the faster the code will converge.

3.4.4 Modifying the boundary conditions

After the Cantera flame object has been initialized, its boundary conditions (BCs) are the same as the ones defined in the loaded initial solution. These do not necessarily agree with the ones required for the present calculation, and therefore a modification is required, as indicated by the point **"6. Modify flame boundary conditions"**. This includes the modification of the pressure, the inlet temperatures and mass compositions.

These three modifications are performed in sequence. The main idea is the following: The current boundary condition of the flame is compared to the desired boundary condition. If the two do not coincide, then the applied BC is altered, and brought closer to the desired value. The solution of the 1D flame problem is undertaken again. If the code fails to converge, then the magnitude, by which the BC was changed, is reduced and the solution is attempted again. Upon successful convergence of the 1D flame, the applied and desired values for the BC are compared and the process is iterated, until a coincidence of the two values is reached. In Figure 3.7, this process is drawn schematically for the pressure correction. The temperature and mass fraction modifications are performed in very similar manner.

An important step for the solution of the 1D flame problem in Cantera is the scaling of the existing solution, as indicated in the Figure 3.7. When changing the boundary conditions of the flow problem, the code requires more time in order to converge. For an acceleration of the convergence procedure Fiala et al. [37] proposed a scaling rule for counterflow diffusion simulations. This scaling is extensively described in [37] and is applied to the mass flow, domain length, velocity and temperature profiles before solving with the new applied boundary conditions. This serves as an improved initialization for the solution and significantly accelerates the convergence behavior.
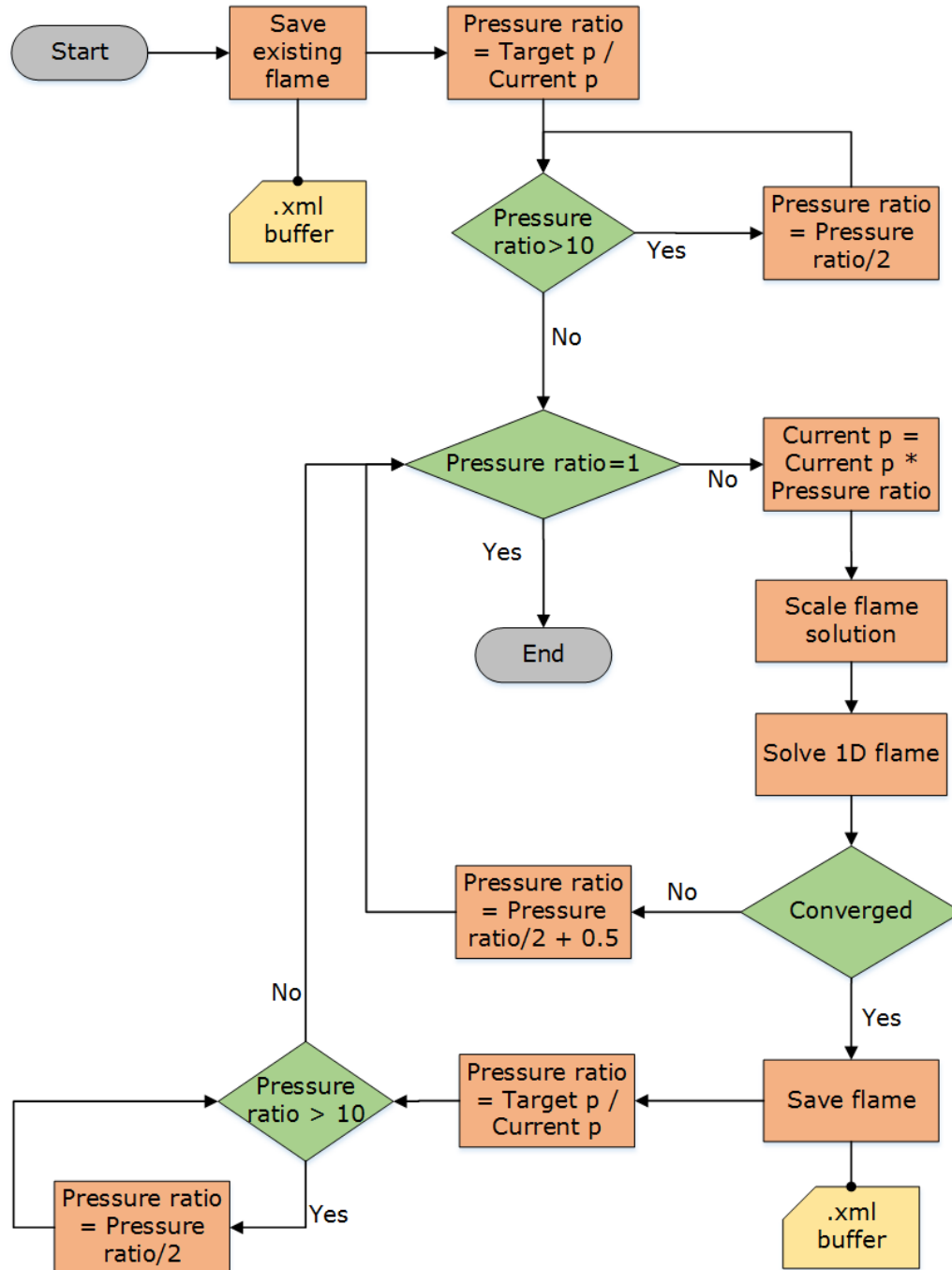
Figure 3.7: Flow chart of the pressure correction in the laminar table generation.

3.4.5 Calculating the equilibrium solution

After the boundary conditions of the flow problem have been corrected, the scalar dissipation rate is gradually reduced, in order to find the equilibrium solution. This represents point "**7. Calculate equilibrium solution**" in Figure 3.6. The equilibrium solution in this context represents the solution corresponding to the lowest value of the scalar dissipation χ. The main concept lies in gradually reducing the value of the strain rate

in the flame until it reaches a predefined limit. The strain rate is proportional to the scalar dissipation as shown in Eq. (3.2) and therefore its reduction corresponds to approaching the equilibrium solution.

The lower limit is given by the user, and a value equal to 0.01 s^{-1} was found to be adequate both for the methane/oxygen and hydrogen/oxygen combustion. Theoretically, reducing this value further would lead to a more accurate solution for the chemical equilibrium. However, it was observed, that Cantera experiences difficulties converging when the values of the strain rate approach zero. This is due to the way that a lowering of the strain rate is implemented in the counterflow diffusion flame problem. The mass flow rate has to be reduced, and the distance between the two inlets has to be increased, approaching infinity in the limit of zero strain rate (or scalar dissipation equivalently). Therefore, the value of 0.01 s^{-1} was found to be a good compromise, leading to a good convergence of the code while being close to the equilibrium solution at the same time.

The process of reducing the strain rate and calculating the equilibrium solution is shown in Figure 3.8. After saving the existing flame, the strain rate is calculated. This is done with the expression in Eq. (3.1). In order to reduce this strain rate, a value for the strain rate ratio (SRratio) is defined. This is the factor, by which the strain rate is reduced in each step. Choosing a very steep decrease, leads to difficulties in the convergence of Cantera, since the initial and target solution will differ significantly. Choosing too low a factor however on the other hand, means that a larger number of calculations has to be carried out in total, for the final value to be reached. A compromise was found by choosing the SRratio equal to 0.7.

After this is defined, the loop is started. The first step within the loop is checking whether the target strain rate of this step is lower than the final one (SRlimit). Since having a lower strain rate than SRlimit is not required, the reduction factor is decreased appropriately. The next step is scaling the flame solution. This process serves the purpose of improving the convergence behavior of the Cantera solution and is based on the work of Fiala et al. [37] as explained earlier in the present section.

With the improved boundary conditions, the 1D counterflow diffusion problem is solved. If the convergence is unsuccessful, then the SRratio is altered. The ratio is made smaller, in order to ensure that the convergence becomes easier. If the code continues failing to converge, then other measures are taken. After the 4th failed attempt, the tolerance limits are loosened and the SRratio is returned to 0.75. If the problem of convergence persists, then after the 7th failure, the SRratio is increased to 0.95 and the target value for the strain rate is increased by a factor of 1.2. Once this step is carried out, it implies that the limit for the strain rate given by the user (0.01 s^{-1} in this case), cannot be reached. As described in

Chapter 4, this was the case for several CH_4/O_2 test cases. With the new limit and reduction factor, the next iteration of the loop is started and the flame solution is attempted again.

Once the solution converges, then the flame is saved and the tolerance limits as well as the SRratio are restored. The loop keeps running until the strain rate reaches its target value. Then the resulting equilibrium solution is saved and the corresponding scalar dissipation rate is calculated. This is given by Eq. (3.2).
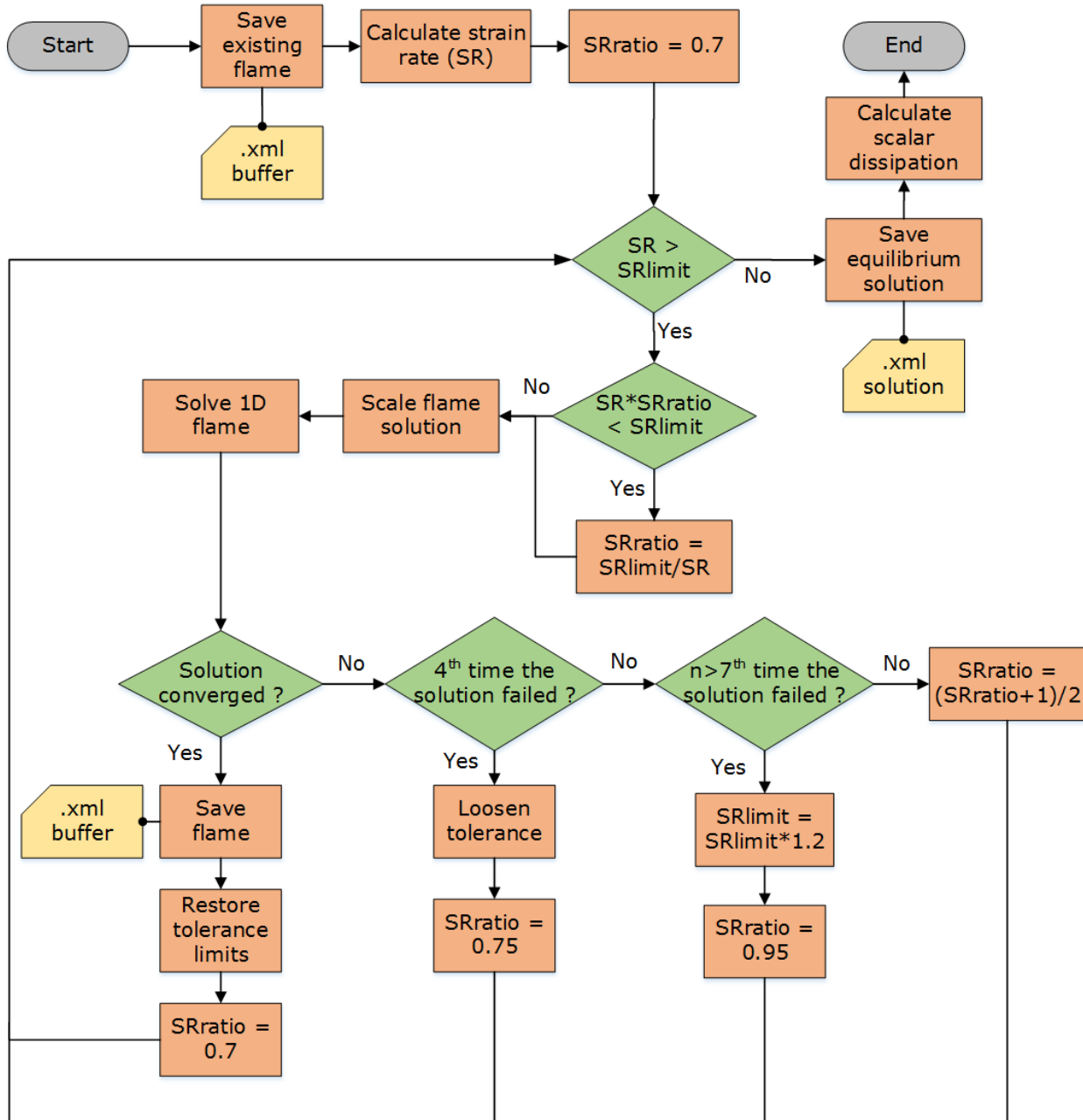
Figure 3.8: Flow chart of the equilibrium solution calculation in the laminar table generation.

3.4.6 Variation of scalar dissipation

The final step in the generation of the laminar table is solving the flame problem for a wide range of χ-values. These values will later on serve as the "grid" of the scalar dissipation, used in the Flamelet table. The grid extends from the lowest possible value for the scalar dissipation (equilibrium solution defined in the previous step) up to the extinction point of the flame. Hence, the critical value at which the flame extinguishes has to be calculated. For that reason, the calculation is divided in three phases or runs:

Run 1: The strain rate is increased in large steps, until the flame extinguishes
Run 2: Starting from the last step before extinction, the strain rate is increased in fine steps, until the flame extinguishes again. Using this extinction value, the grid for the scalar dissipation is calculated.
Run 3: For each one of the values for the scalar dissipation, the solution is obtained and saved in .csv files.

This process is illustrated in Figure 3.9 in simplified form. Within the solution process, the strain rate is updated in every iteration before solving the 1D flame problem. The way this update is done is dependent on which run is executed at the time. For the first run, the current strain rate value is increased in a coarse manner by being multiplied with a large factor >1, whereas in the second run, a smaller factor is utilized, closer to 1.05, in order to ensure a finer increase. These factors are not constants but vary depending on the current iteration number according to empirical relations. For the third run, a distribution is defined for the values of the scalar dissipation ranging from the lowest value up to the extinction value. In the case of methane, it was found that a logarithmic distribution provides satisfactory results.

As seen in Figure 3.9, the number of χ-values is restricted to 60. This is done because ANSYS CFX allows a maximum of 60 values for the scalar dissipation when importing a Flamelet table. Hence this setting was adopted during the table generation process. The resulting 60 .csv solutions contain the profiles for Z, T and Y_i along the axial position x. They can be then used to generate the turbulent table.
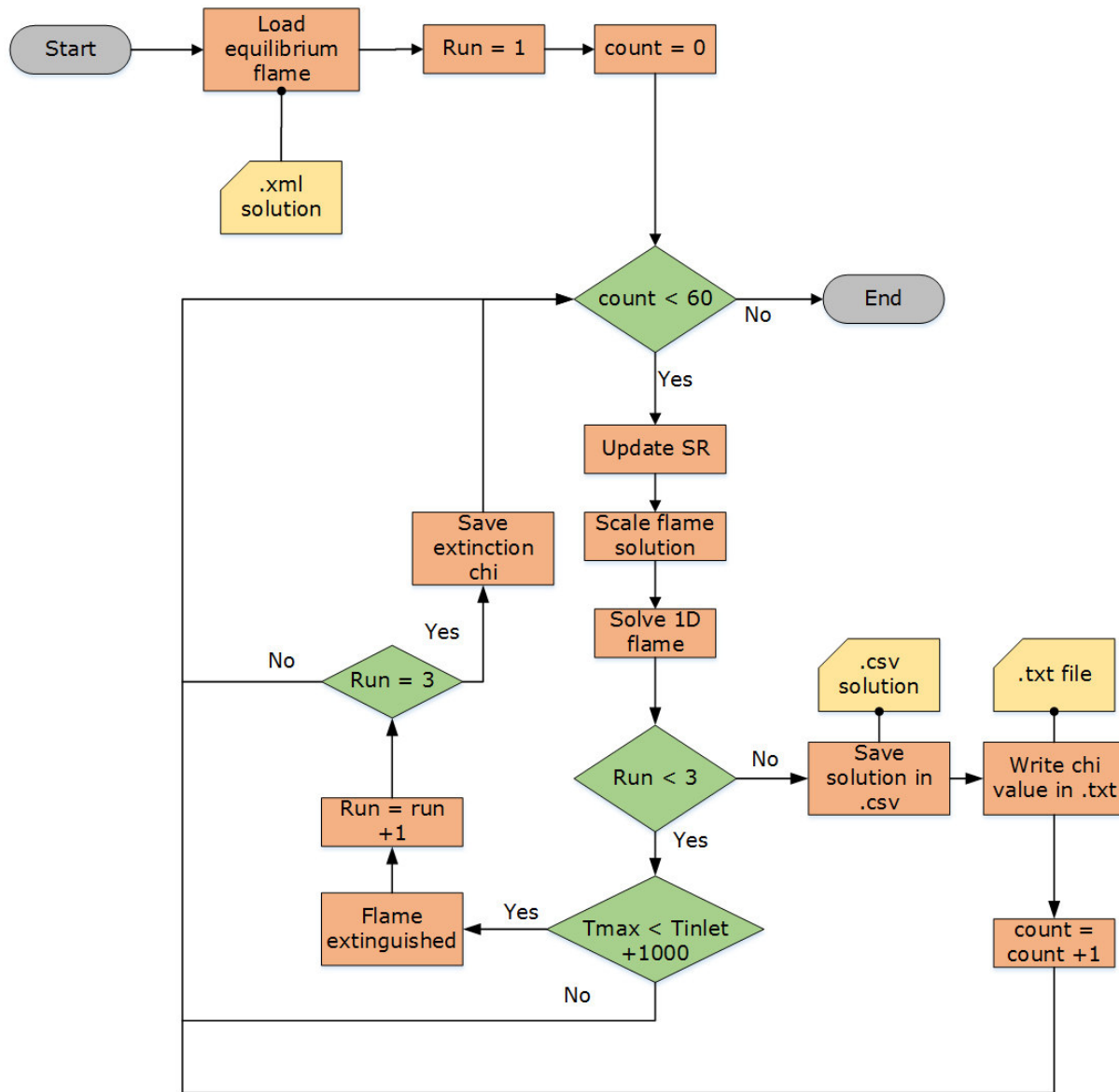
Figure 3.9: Flow chart of the scalar dissipation variation during the laminar table generation.

3.5   Generating the turbulent table

Using the laminar table, the final step of the Flamelet table generation lies in incorporating the effect of turbulence. This takes into account the interaction between chemistry and eddies in the flow. The resulting turbulent table is the final output of the code and can be directly imported into a commercial solver for the CFD simulation.

3.5.1 Format of CFX RIF tables

The format of the generated table must be compatible with the guidelines of CFX-RIF [16]. Within each table, the mass fractions of all species are tabulated as a function of $\tilde{Z}$, for each combination of $\tilde{\chi}$, $\widetilde{Z''^2}$. However, according to the definition of the mixture fraction variance, its maximal value is a function of the mixture fraction itself and is given by:

$$\widetilde{Z''^2}_{max} = 0.25 - \left(0.5 - \tilde{Z}\right)^2 \tag{3.20}$$

For that reason, in order to drastically reduce the size of the table and simplify its structure, the normalized variance is used, $\widetilde{Z''^2}_{norm}$, whose definition is given in Eq. (3.21)

$$\widetilde{Z''^2}_{norm} = \frac{\sqrt{\widetilde{Z''^2}}}{\min\left(\tilde{Z}, 1 - \tilde{Z}\right)} \tag{3.21}$$

The structure of the file reads as follows:
1) Comments (optional)
2) A header defining the library dimensions and sample points for tabulation
3) Component mass fractions for the unburnt Flamelet (inert mixing) as a function of $\tilde{Z}$
4) Component mass fractions for each combination of $\tilde{\chi}$, $\widetilde{Z''^2}$ as a function of $\tilde{Z}$

A generic example of a CFX-RIF table, which visualizes its structure, is shown in Figure 3.10.

3.5.2 PDF Integration

The table resulting from the laminar calculation using Cantera, has the form $Y_i = Y_i(Z, \chi)$. Although commercial and open source tools exist, which can integrate this laminar table as described in Section 2.2.7, a new script was programmed in Python for this task. The benefit of using an in-house tool was the flexibility attached to it, allowing for a more complete overview of the operations taking place.

The selection between a Gaussian and a β-PDF is possible in this Python-integrator. Using this PDF type, the values of the PDF are calculated for a chosen combination of $\widetilde{Z''^2}$ and $\tilde{Z}$ according to Eqs. (2.73)-(2.76), yielding $P(Z)$. The subsequent step is integrating the integrand $P(Z) \cdot Y_i(Z)$ for each one of the species i. In order to carry out the numerical integration, the trapezoidal rule was implemented [50] with the built-in function "trapz", from the "scipy.integrate" Python module [51].

```
C      Flamelet Library
C
C      Pressure         [bar]:      1.0000
C      Temp Oxidizer    [K]  :    300.0000
C      Temp Fuel        [K]  :    300.0000          Comments
C      Scalar Diss Rate [1/s]:   0 - 10
C      Z-Variance factor :       0 - 0.99
```

```
DIMENSIONS :
MSTZ, MSPEC, MSTRN, MSVAR (I3,I3,I3,I3)
 10   9   2   2
-------------------------------------------
STRAIN - STEPS   (unused)
 0.00000E+00    0.00000E+00
SCALAR DISSIPATION RATE - STEPS                    Header
 0.00000E+00    0.10000E+02
VARIANCE - STEPS
 0.00000E+00    0.99000E+00
Z
 0.00000E+00    0.25000E-01    0.50000E-01    0.75000E-01    0.10000E+00
 0.48571E+00    0.61429E+00    0.74286E+00    0.87143E+00    0.10000E+01
```

```
Unburnt Flamelet
H2
 0.00000E+00    0.25000E-01    0.50000E-01    0.75000E-01    0.10000E+00
 0.48571E+00    0.61429E+00    0.74286E+00    0.87143E+00    0.10000E+01
O2
 0.23300E+00    0.22718E+00    0.22135E+00    0.21553E+00    0.20970E+00
 0.11983E+00    0.89871E-01    0.59914E-01    0.29957E-01    0.10408E-15

  .

  .                                               Unburnt Flamelet

  .

N2
 0.76700E+00    0.74782E+00    0.72865E+00    0.70947E+00    0.69030E+00
 0.39446E+00    0.29584E+00    0.19723E+00    0.98613E-01    0.00000E+00
```

```
  0.000000E+00    0.000000E+00
H2
 0.10000E-24    0.32167E-03    0.22257E-01    0.48043E-01    0.73785E-01
 0.47074E+00    0.60305E+00    0.73537E+00    0.86768E+00    0.10000E+01
O2
 0.23300E+00    0.26938E-01    0.13402E-05    0.30433E-08    0.12735E-10
 0.00000E+00    0.00000E+00    0.00000E+00    0.00000E+00    0.10000E-24

  .

  .                                          First combination of

  .                                          dissipation and variance

N2
 0.76700E+00    0.74782E+00    0.72865E+00    0.70947E+00    0.69030E+00
 0.39446E+00    0.29584E+00    0.19723E+00    0.98613E-01    0.00000E+00
  0.100000E+00    0.000000E+00
H2
 0.10000E-24    0.32167E-03    0.22257E-01    0.48043E-01    0.73785E-01
 0.47074E+00    0.60305E+00    0.73537E+00    0.86768E+00    0.10000E+01
O2
 0.23300E+00    0.26938E-01    0.13402E-05    0.30433E-08    0.12735E-10
 0.00000E+00    0.00000E+00    0.00000E+00    0.00000E+00    0.10000E-24

  .

  .                                          Second combination

  .

  .
```

Figure 3.10: Example of a generic CFX-RIF table for illustration of its structure.

In the case of the β-PDF integration, special numerical treatment has to be applied in the cases where the parameters α, β become smaller than unity. This leads to a singularity

either at the origin or at $Z = 1$ as the plots of the PDF and CDF (Cumulative Distribution Function) demonstrate in Figure 3.11. Since any type of non-analytic integration (including the trapezoidal rule) would produce a NaN or Inf value in the event a singularity, the PDF was modified in those cases, as described in Appendix C.
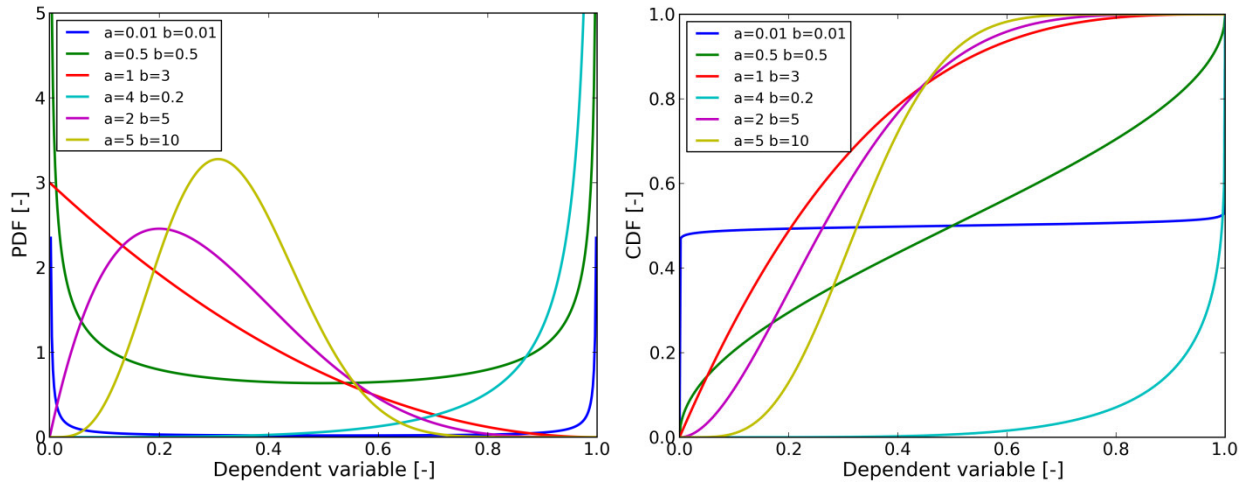
Figure 3.11: PDF and CDF profiles for different combinations of the parameters α, β in β-PDF.

3.5.3 Validation of PPDF integration module

A previous thesis at Airbus Defence and Space led to the development of a Flamelet table generator for H_2/O_2 combustion [52], which was validated by Ivancic et al. [53]. In that Flamelet generator, the integration of the laminar table was performed using the open source tool OpenFOAM and specifically the "canteraToFoam" module. The process followed when utilizing canteraToFoam is conceptually similar, and involves the laminar table containing the species mass fractions being passed on to the OpenFOAM/Python interface and integrated according to a β-PDF.

Since the OpenFOAM module has been applied and validated in several other applications involving Flamelet table generators (Müller et al. [49]), it was used as a verification tool for the Python-based integration module. For that reason, a laminar H_2/O_2 table, generated by the code from Katzy [52] was used and integrated with the new PDF integration module, leading to an .fll Flamelet library file. The results of this integration were compared to the values obtained by integrating the same table using the canteraToFoam module. This process is schematically illustrated in Figure 3.12.
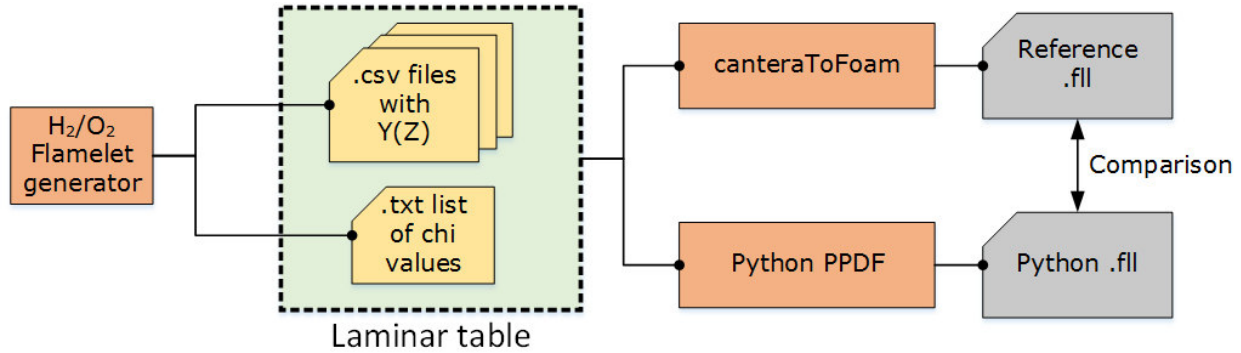
Figure 3.12: Validation process for the Python PPDF integration module.

For the comparison, a generic test case at 10 bar operating pressure, 500 K oxidizer inlet temperature and 600 K fuel inlet temperature was taken. The results from the two methods demonstrate a satisfactory match, which can be observed in Figure 3.13, where the mass fractions of OH and O_2 are plotted for different values of the scalar dissipation $\tilde{\chi}$ and the normalized mixture fraction variance $\widetilde{Z''^2}_{norm}$.

One can identify, that a slight discrepancy between the two solutions occurs in the vicinity of $Z = 0.5$ for higher values of $\widetilde{Z''^2}_{norm}$. Close to this combination of Z and $\widetilde{Z''^2}_{norm}$, the mixture fraction variance approaches $\widetilde{Z''^2} = 0.25$ and hence the parameters α and β of the β-PDF draw near zero. The β-PDF then approaches a double-Dirac function and a fine grid is required for the integration. The canteraToFoam module has a coarse grid for the integration close to $Z = 0.5$, which leads to the observed difference between the two solutions. This is better understood when examining the OH concentrations for $\widetilde{Z''^2}_{norm}$ and $Z = 0.5$. Theoretically, $\alpha = \beta = 0$ for the PPDF at this point and the concentration of OH should be exactly zero, as predicted by the Python integrator. The canteraToFoam module on the other hand predicts a finite mass fraction, due to the coarser grid. Since the source of this minimal difference between the two codes was pinned down, the Python integrator was validated and further utilized for the Flamelet generator.
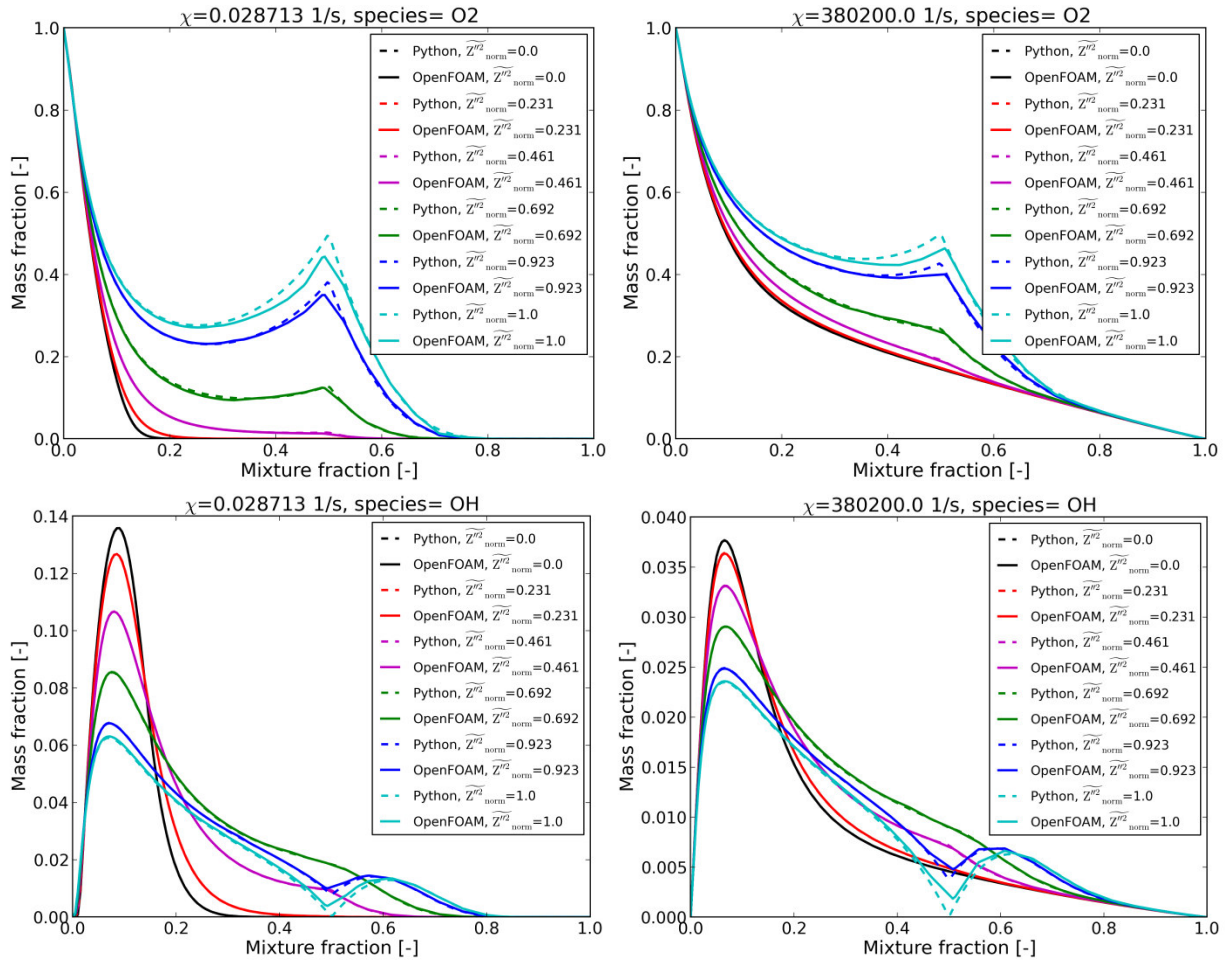
Figure 3.13: Comparison between canteraToFoam and Python PPDF integration results for a H_2/O_2 combustion test case.

3.6 Differences with RIF tables

The motivation behind creating the Flamelet tables using an in-house Cantera tool instead of the commercial CFX-RIF module lies in having a better control over the chemical reaction mechanism used. It is however important to grasp the main differences between the Cantera and RIF modules when applying the Flamelet model in CFD applications.

As already mentioned, the Cantera table generation involves the solution of the counter-flow diffusion flame, whereas the RIF module solves the exact Flamelet equations. This gives rise to two further differences. Firstly, the definition of the scalar dissipation in Cantera, occurs after the solution of the flow problem, using the expressions in Eqs. (3.1) and (3.2). The analytic formula used for the transformation of the strain rate into the scalar dissipation could eventually lead to discrepancies compared to the direct definition of χ in Eqs. (2.66)-(2.67) (as done in RIF) or compared to the calculation process in the CFD

solution, shown in Eq. (2.64). On the other hand, the user can modify the definition of the scalar dissipation calculation in Cantera, in order to adjust the expression to the specific problem. Secondly, the definition of the mixture fraction as a function of the axial coordinate is also done *a posteriori* in the case of Cantera, according to Eq. (2.57). This adds a further source of uncertainty that should be taken into account, especially when working with different propellant combinations, since the definition of Z may need to be modified.

Furthermore, an additional point where the two modules distinguish from each other is the definition of the transport properties. Cantera implements the gas kinetic theory in order to calculate the diffusion coefficient of each species into the mixture, whereas RIF utilizes the $Le = 1$ assumption. Although the Cantera formulation is more precise since it incorporates realistic transport coefficients, it also contradicts one of the basic assumptions used in the derivation of the mixture fraction. Specifically, Z is defined based on the assumption of unity Lewis number for all species. When this is not fulfilled, a mixture fraction variable has to be defined for each species separately [30], which is however not implemented in the Flamelet calculations using CFX. This conflict with the mixture fraction theory has to be kept in mind when evaluating the results.

Moreover, Cantera is unable to perform calculations when the inlet temperature of the oxidizer or the fuel is below 200 K. This implies that for cryogenic applications where e.g. the LOX is injected at 100 K through the injector, the Flamelet table has to be generated for the lowest temperature allowed in Cantera, i.e. 200 K. Since only the mass fractions are tabulated in the final Flamelet library and not the temperature values, this disadvantage of Cantera has no direct effect on the final solution.

Finally, the Cantera tool has an embedded flexibility in the definition of the reaction mechanism and the PPDF type. The user is free to implement a complete or reduced mechanism or even examine the effect of individual species in the mechanism. RIF uses the C1 and C2 mechanisms in the case of methane/oxygen combustion, which are however not described in literature and can also not be modified. In the present thesis, the C1 mechanism has been implemented for the RIF based calculations, which consists of 17 species. For the PPDF integration, RIF has a built-in β-PDF, and the user has no influence in its definition or modification.

Achieving a satisfactory understanding of the calculation process in the Flamelet table generation is crucial when evaluating the CFD results. Having established the main concepts involved in the generation of the libraries and having highlighted the differences between the Cantera tool and the commercial module RIF, the results obtained with the Cantera/Python tool are analyzed in Chapter 4.

4 Discussion of Flamelet results

Before examining the Flamelet tables solely based on the results they provide in a CFD calculation, exploring the values stored in the tables is a very significant step. This allows for a better understanding of the methane/oxygen combustion characteristics at different conditions. Based on the knowledge obtained by this inspection of the Flamelet tables, the results occurring later on in the CFD calculations can be better interpreted.

Section 4.1 presents the theoretical equilibrium results for the methane/oxygen combination, which serve as a baseline for further comparisons of the Flamelet tables. The results stored in the laminar table (namely excluding the effects of the PDF integration) are illustrated in Section 4.2 and in Section 4.3 they are compared to results found in the literature, thereby leading to a validation of the Flamelet generator. The main differences between the methane/oxygen and hydrogen/oxygen combustion properties are elaborated on in Section 4.4.

4.1 Theoretical equilibrium solution

An important solution included in a Flamelet table is the case of $\chi = 0\,\mathrm{s}^{-1}$, which corresponds to the equilibrium solution. As the results in Chapter 5 show, the solution corresponding to low values of scalar dissipation becomes very important in CFD calculations at the regions close to the walls. Since these positions are characterized by low speeds and a nearly laminar flow, χ takes values close to zero, since it is defined as in Eq. (2.64). The local temperature and gas composition near the wall define the transport properties and hence have a significant influence on the wall heat flux.

In order to obtain a better understanding of the methane/oxygen combustion at equilibrium, calculations were performed to determine the theoretical gas composition and temperature at those conditions. This calculation takes place by assuming a zero-dimensional (0D) homogeneous reactor at isobaric and adiabatic conditions. The initial pressure, temperature and composition of the gases are given by the user and the equilibrium solution is found by means of Gibb's enthalpy minimization [14]. For that purpose, two different tools were utilized and compared with each other:
- Chemical Equilibrium with Applications (CEA) code developed at NASA [54]
- Built-in Cantera 0D equilibrium tool "equilibrate"

Both tools delivered nearly identical results, with a relative discrepancy smaller than 0.5% for the temperature and gas mass fractions. By evaluating the chemical equilibrium solution

for different values of the initial composition (variation of oxidizer to fuel ratio), the dependence of the temperature and gas mass fractions on the mixture fraction can be obtained. In order to enable a more detailed examination of those profiles, the results of CH_4/O_2 combustion were compared to the ones of H_2/O_2 combustion. Hydrogen combustion demonstrates a less complex reaction mechanism which can be validated when taking a look into the temperature profiles illustrated in Figure 4.1. They correspond to a 0D equilibrium calculation a 1 bar operating pressure and with an initial temperature of 300 K for the mixture.
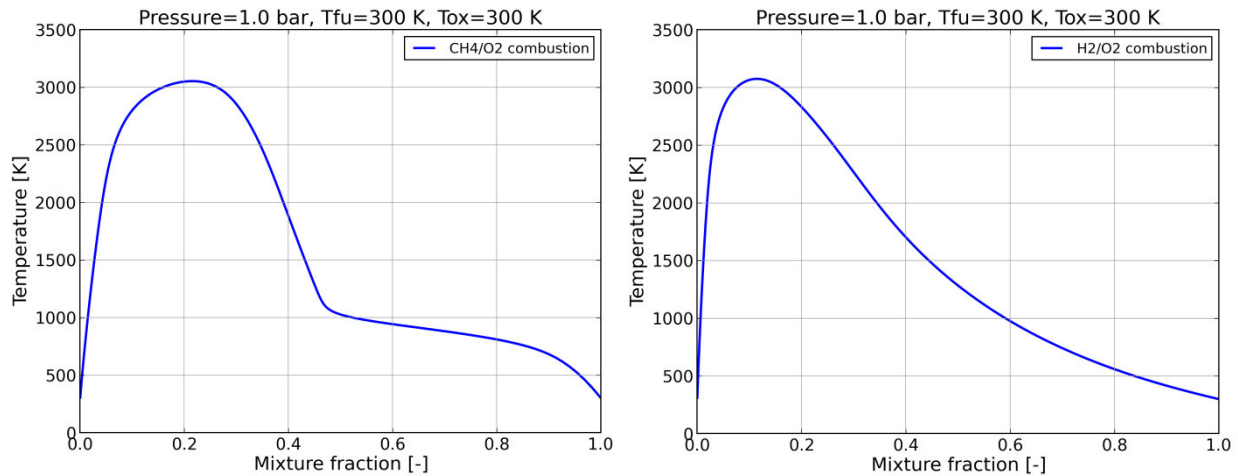
Figure 4.1: Temperature dependence on mixture fraction for the equilibrium solution of CH_4/O_2 (left) and H_2/O_2 combustion (right).

As expected, both the hydrogen/oxygen as well as the methane/oxygen combustion show a temperature maximum close to the point of stoichiometric composition. In the case of CH_4 this occurs close to $Z_{st} = 0.2$ whereas for H_2 it takes place around $Z_{st} = 0.11$. For pure oxidizer ($Z = 0$) and pure fuel conditions ($Z = 1$), there are no chemical reactions and hence the temperature remains unchanged at 300 K. The main qualitative difference in the two temperature profiles of Figure 4.1 occurs after the maximum mixture temperature, namely for mixture fraction values larger than Z_{st}. In the case of hydrogen, the temperature drops from its maximal value down to the 300 K in a smooth and continuous manner. Methane on the other hand demonstrates a sharp decrease directly after its maximum until $Z \approx 0.45$ and then proceeds with a much slower decline down to the initial temperature. This sudden change in slope gives rise to a kink point within the profile.

In order to examine the nature of this salient point, the pressure load point was varied. The resulting profiles for the temperature profile are given in Figure 4.2. It is evident, that the kink remains for all pressure levels from 1 bar to 200 bar. For higher pressures, the temperature rises as expected but the slope of the profile remains qualitatively similar.
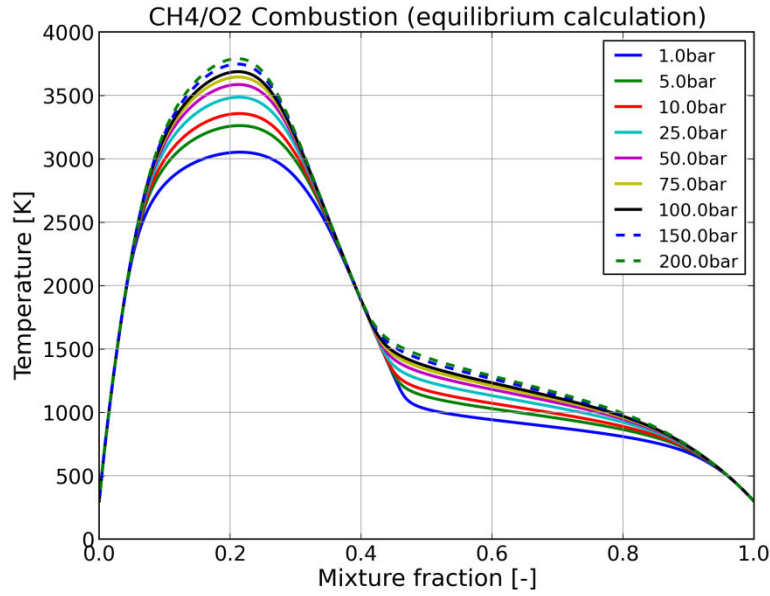
Figure 4.2: CH$_4$/O$_2$ equilibrium temperature profile over mixture fraction for different pressure load points.

For that reason, identifying the cause of the kink requires investigating the species profiles over the mixture fraction, as illustrated in the left subfigure of Figure 4.3. The mass fraction of the oxidizer and fuel is equal to 1 at the $Z = 0$ and $Z = 1$ boundaries respectively and is reduced for mixture fraction values closer to Z_{st}. If the combustion process was dictated by a single-step mechanism, a Burke-Schumann flame would be present, where the mass fractions of O$_2$ and CH$_4$ would drop linearly from 1 at the boundary to 0 at $Z = Z_{st}$ [32]. This is not the case for a detailed reaction mechanism, as the GRI 3.0 implemented here, since recombination and secondary reactions lead to a consumption or production of the oxidizer and fuel and hence to a departure from the linear profile. This is seen in Figure 4.3, where CH$_4$ reaches 0 close to $Z \approx 0.45$ and O$_2$ at around $Z \approx 0.3$, i.e. not directly at the stoichiometric point. This is one of the main differences compared to the H$_2$/O$_2$ combustion (right subfigure in Figure 4.3). In fact, this region that exists between $Z \approx 0.3$ and $Z \approx 0.45$ is a byproduct of the thermal dissociation of methane even in the absence of oxygen. It is hence expected that even in certain fuel-rich configurations (e.g. O/F=3.4, i.e. Z=0.227) no methane is present after the end of combustion and only some oxygen remains. This effect is counter-intuitive and has to be kept in mind when evaluating the results in Chapter 5.

In the hydrogen combustion, there appears to be a region between $Z \approx 0.1$ and $Z \approx 0.2$, where both oxidizer and fuel are present simultaneously. Such a region of overlap would not be allowed in the absence of reverse reactions, since the remaining oxygen and hydrogen would react and produce H$_2$O. It is however present in real flames, mainly due to the existence of recombination effects and is expected in reaction mechanisms involving more

than a single step [32]. For that reason, the fact that CH_4 reaches a mass fraction equal to 0 for Z values much larger than Z_{st} could be identified as an "abnormality" of the CH_4/O_2 fuel combination when compared to H_2/O_2 and as a reason for the observed kink in the temperature profile.
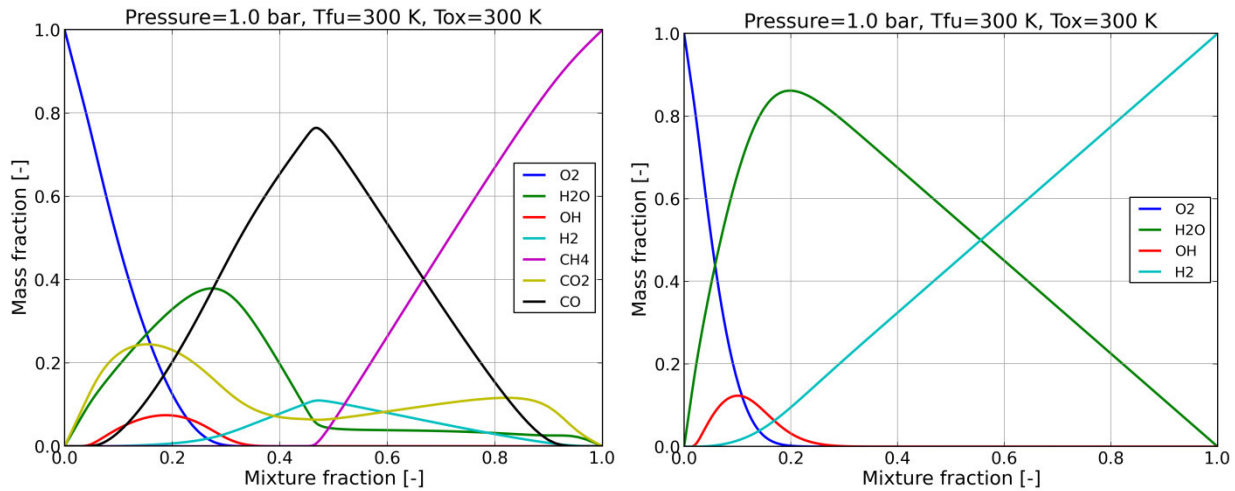
Figure 4.3: Mass fraction dependence on mixture fraction for the equilibrium solution of CH_4/O_2 (left) and H_2/O_2 combustion (right).

The validity of this assumption is enhanced when comparing the profile of temperature with the CH_4 mass fraction as is done in Figure 4.4. The location where methane vanishes is namely coinciding with the kink at the temperature profile. Along with the temperature, the mass fraction of H_2O also has a kink at the exact same location, indicating, that the two effects are connected and are a byproduct of the methane profile.
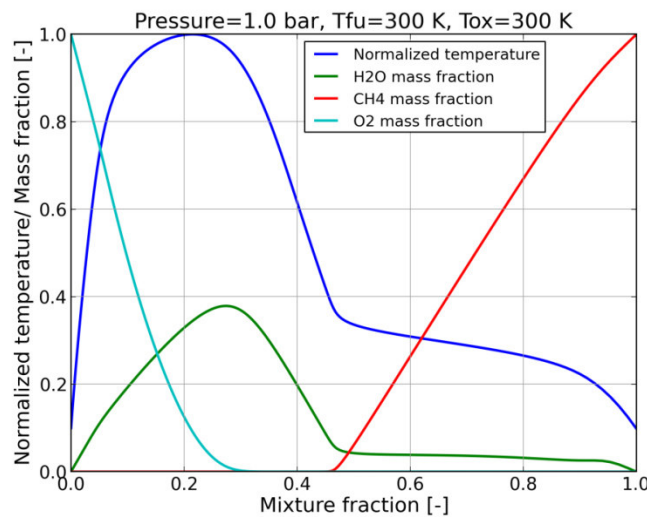
Figure 4.4: Temperature, H_2O and CH_4 profiles as a function of mixture fraction in the CH_4/O_2 equilibrium. The temperature is normalized by its maximum value.

As an explanation for the apparent influence of CH_4 on the gas temperature, a combination of two effects is identified and shown in Figure 4.5. First, the energy release from the chemical reactions is reduced quite sharply and reaches 1% of its maximum for $Z \approx 0.4$ (left subfigure). This could serve as a justification for the sharp initial temperature decrease of Figure 4.1. The second effect is that the presence of methane in the vicinity of $Z \approx 0.45$ triggers a sudden rise in the specific heat capacity of the gas (right subfigure). Methane has a much larger heat capacity than CO, which is the dominant species for mixture fraction values smaller than 0.45. With increasing presence of methane, the specific heat capacity of the mixture is hence expected to rise and the kink in the heat capacity is translated to a kink in the adiabatic equilibrium temperature.
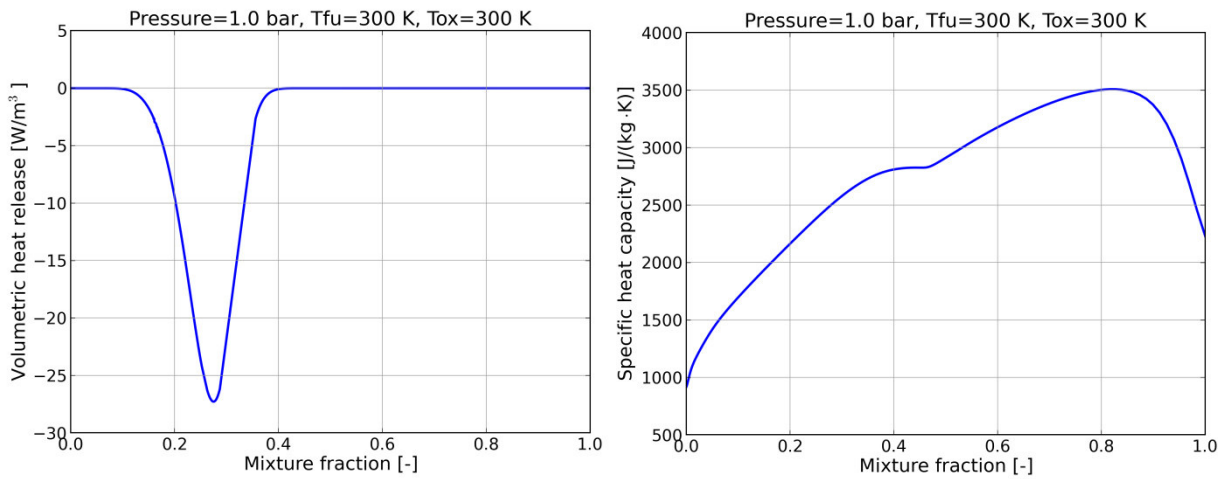
Figure 4.5: Volumetric heat release (left) and specific heat capacity of the gas (right) for the equilibrium solution of the CH_4/O_2 combustion.

The temperature profile has some similarities with the H_2O mass fraction profile, which also possesses a kink. H_2O is a product of the CH_4/O_2 reaction and is expected to have low concentration for mixture fractions larger than the stoichiometric. This is actually observed in Figure 4.4, where the water mass fraction is being reduced up to $Z \approx 0.45$. After this point, its profile's slope drops and the concentration decreases much slower until it reaches zero for $Z = 1$. The presence of methane could be the cause of this effect, since it acts as a third body in several reactions involving the production of water [23], such as:

$$H + OH + M \rightarrow H_2O + M \tag{4.1}$$

Apart from the methane, water and temperature profiles, the CH_4/O_2 equilibrium solution has a further intriguing property, which is the mass fraction profile of CO_2, as shown in Figure 4.3. This demonstrates a complex behavior with two local maxima, one located close to the stoichiometric point $Z \approx 0.2$ and a second one at $Z \approx 0.85$. The second maximum

could be a result of the CO decomposition in the presence of methane. The mass fraction of the secondary species CO appears to be dropping after $Z \approx 0.45$ and part of this could be attributed to the decomposition:

$$CO + O + M \rightarrow CO_2 + M \tag{4.2}$$

Methane has a significant influence in this reaction as well, by acting as a third body, which would explain the second rise of the CO_2 mass fraction at $Z \approx 0.85$. For even larger values, CO_2 drops again, since there is not enough oxygen present, to initiate the CO_2 formation. The complexity of the methane/oxygen combustion is hence evident based on the theoretical equilibrium calculations. The resulting profiles of this analysis serve as a comparison measure for the Flamelet results produced by the table generator.

4.2   Laminar Flamelet results

Upon solving the counterflow diffusion flame, the laminar Flamelet table, consisting of the species mass fractions along Z, is available. As described in Section 3.4, the scalar dissipation rate is decreased until the equilibrium solution is approximated. The comparison between the theoretical flame temperature at equilibrium and the Flamelet solution, is illustrated in Figure 4.6 for the 1 bar case.
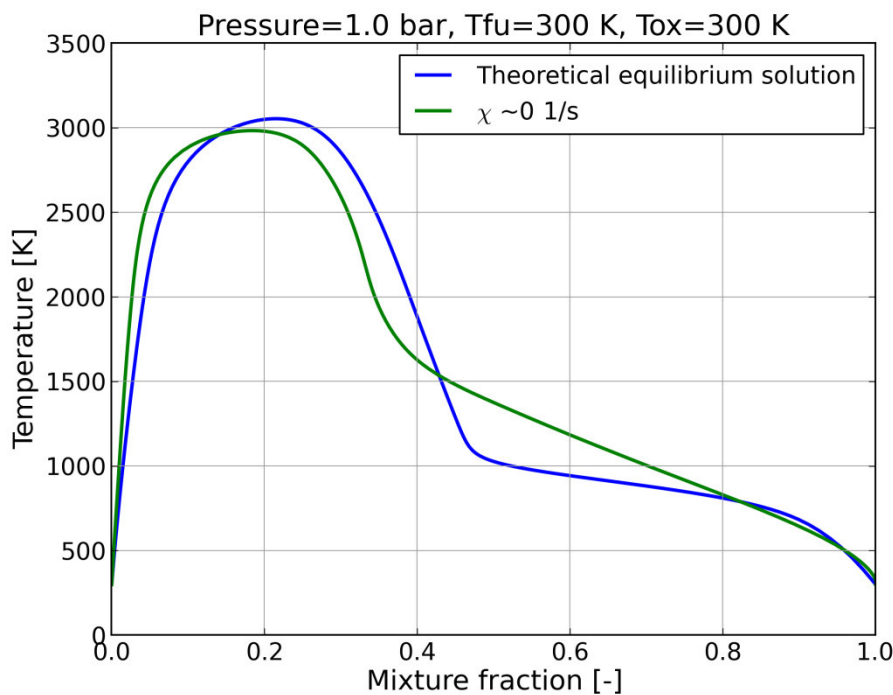
Figure 4.6: Comparison between theoretical equilibrium solution and Flamelet solution for $\chi \rightarrow 0\,\mathrm{s}^{-1}$ **at 1 bar.**

It appears that a slight discrepancy occurs between the two solutions. As expected, the highest temperature of the Flamelet solution is lower than the equilibrium one, since the equilibrium is only approximated when solving the 1D counterflow diffusion equations for $\chi \to 0\,\mathrm{s}^{-1}$ but never really reached. Both profiles show similar trends, with a drop in temperature after $Z \approx 0.3$, however the equilibrium solution possesses a steeper decrease. This qualitative difference could be a result of the different problem formulation: minimization of Gibb's enthalpy in the case of chemical equilibrium and solution of a 1D flow problem in the Cantera Flamelet case.

Despite this difference in the flame temperature, the general trend is consistent in both formulations. Moreover, the species concentrations are the only variable present in the laminar table and hence their examination is also of interest. This is done in Figure 4.7, where the profiles of some major species are plotted over the axial direction x and over the mixture fraction. The set of curves for each species illustrates the effect that the scalar dissipation rate has on each profile. This is only to be examined qualitatively, and the exact value of χ is not significant for this analysis.

As expected, an increase in the scalar dissipation resembles a larger effective diffusivity and for that reason, CH_4 molecules are able to enter oxidizer-rich domains ($Z < 0.2$) at larger χ values. The increased mass fraction of CH_4 for higher dissipation values is also depicted in the concentrations of the other species. The CO_2, CO and H_2O mass fractions show a decrease as soon as the departure from chemical equilibrium becomes larger. This is explained by the fact that less methane reacts, leading to less mass being available for the formation of products and intermediate species.

Finally, an interesting observation, is that the profiles of CO_2 and H_2O (the two products of the stoichiometric methane/oxygen combustion) alter their form close to equilibrium ($\chi \to 0\,\mathrm{s}^{-1}$). Specifically, CO_2 appears to have a second local maximum, which is also observed in the theoretical equilibrium solution (Figure 4.3). In the case of H_2O, the thickness of the profile is reduced at lower dissipation values. This result is consistent with the observation described in Section 4.1 and is responsible for the temperature trend (Figure 4.4) to a large degree, due to water's high heat capacity.
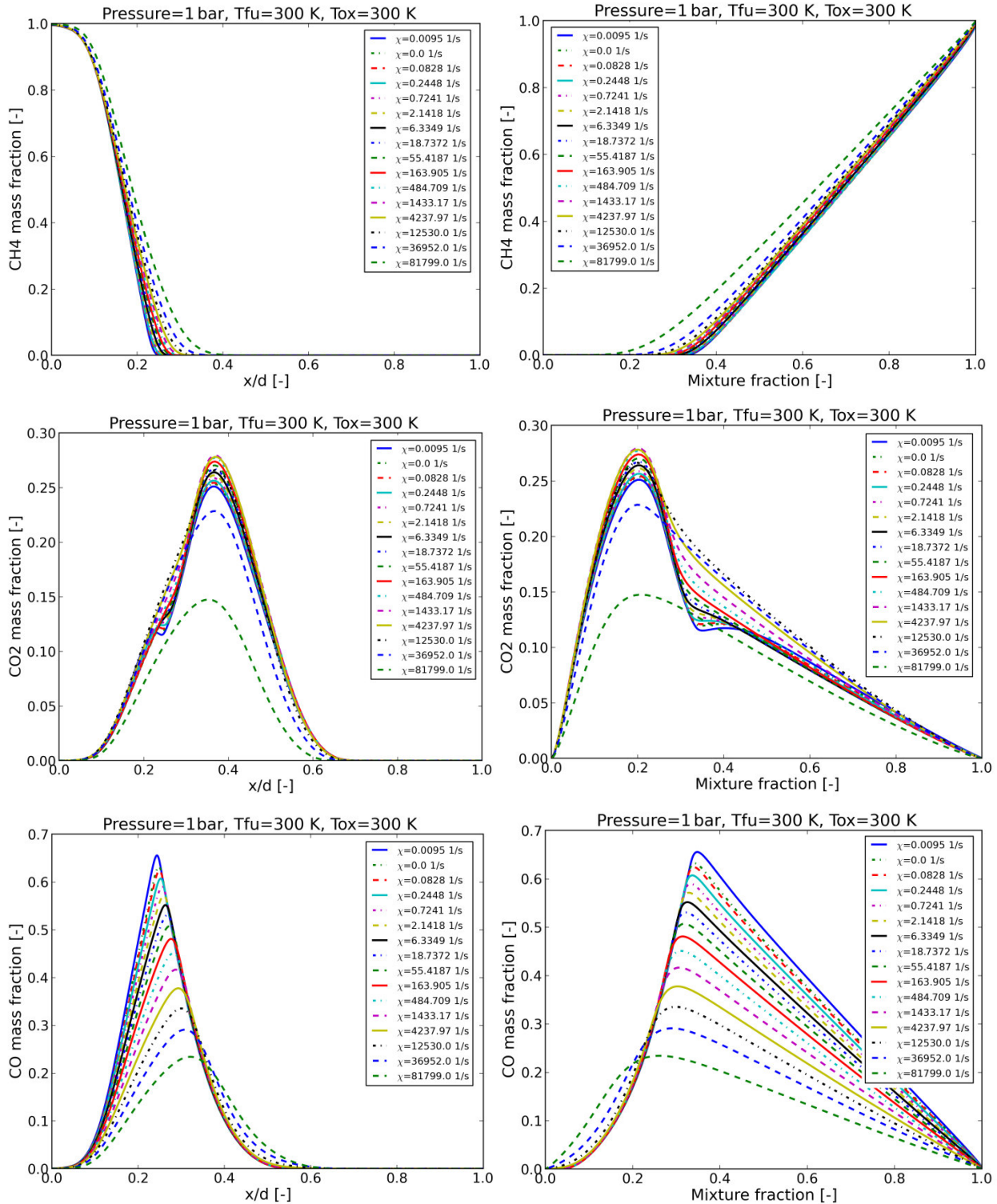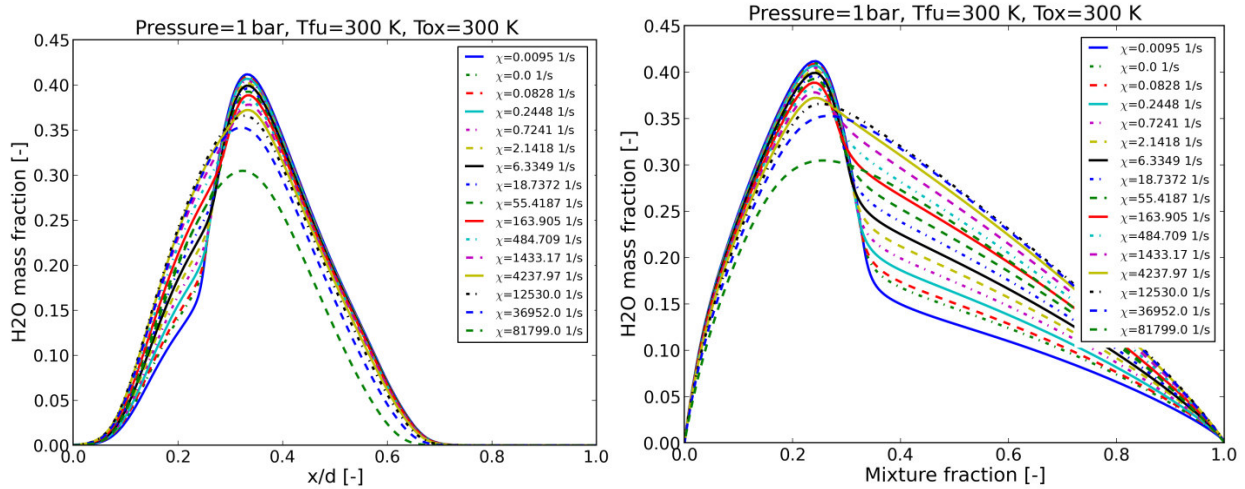
Figure 4.7: Major species' mass fraction over axial position (left) and mixture fraction (right) resulting from the laminar Flamelet table calculation.

4.3   Comparison with literature

In order to examine the validity of the laminar Flamelet results, temperature and mass fraction profiles obtained by the code were compared to data available in the literature. Although various research groups are working on the modeling of hydrocarbon combustion using the Flamelet model, few publications could be identified, showing the distribution of mass fractions and temperature as a function of the mixture fraction. In most cases, the CFD results are demonstrated, without previous description of the tabulated values in the Flamelet library.

In the work of Müller et al. [55], an LES simulation of the CH_4/O_2 combustion at 56.1 bar is undertaken, which corresponds to the experimental setup described in Singla et al. [56]. The oxygen and methane injection temperatures are at 85 K and 288 K respectively. Due to the inability of Cantera to perform calculations at temperatures lower than 200 K, the oxygen temperature was set to be at 200.5 K. Since no real gas effects are modeled neither in Cantera nor in the Flamelet generator "Flamemaster" used in [55][9], the difference in initial temperature should not affect the solution significantly. The reaction mechanism used in [55] is the GRI 3.0 mechanism (black solid line in the following plots), which is also compared to the reduced mechanism of Frassoldati et al. [57] (black dotted line).

---

[9] The software Flamemaster is used for generating the Flamelet tables [70]. This solves the Flamelet equations in the mixture fraction space, as opposed to Cantera, which solves the counterflow diffusion problem in the physical coordinates.

Figure 4.8 shows the temperature profile for the equilibrium solutions ($\chi \approx 0\,\mathrm{s}^{-1}$) obtained with the Flamelet generator developed in this thesis in comparison to the profile in Müller et al. [55]. The temperature plot from literature demonstrates a maximum of approximately 3560 K at a location of $Z \approx 0.2$. This is similar to the solution obtained with the Cantera code, which produces a maximal temperature of 3541 K at $Z = 0.2$. The characteristic "kink" described in Section 4.1 can also be seen in both profiles of Figure 4.8: Comparison of temperature profiles from the Cantera Flamelet generator (right) with results from Müller et al. (left) for 56.1 bar CH_4/O_2 nonpremixed combustion ($\boldsymbol{\chi \approx 0}$)., with the plot from Müller showing a slightly less intense effect.
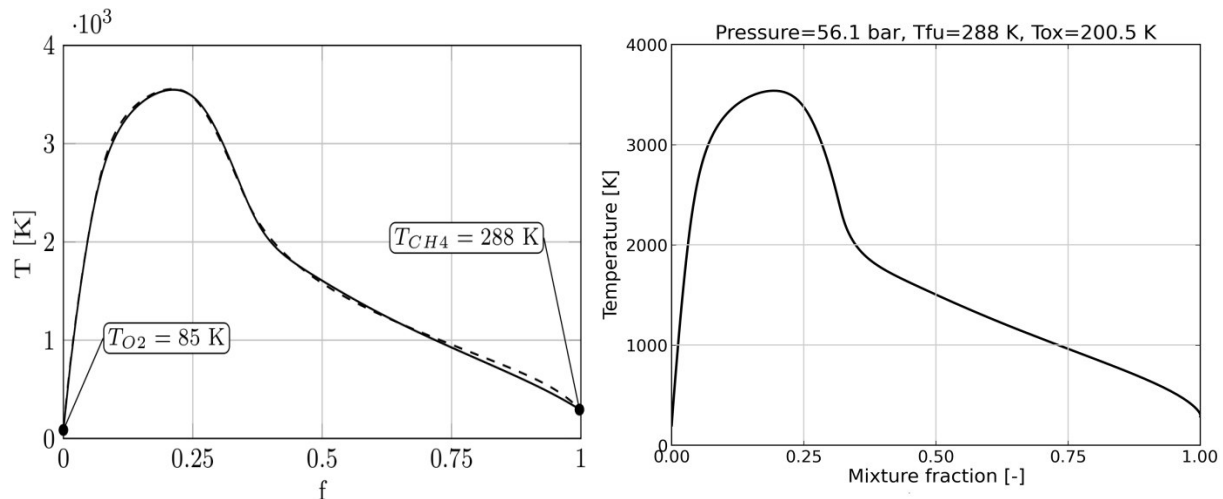
Figure 4.8: Comparison of temperature profiles from the Cantera Flamelet generator (right) with results from Müller et al. [55] (left) for 56.1 bar CH$_4$/O$_2$ nonpremixed combustion ($\boldsymbol{\chi \approx 0}$).

Apart from the temperature, the mass fractions of the chemical species are very important for the comparison, since they are tabulated in the Flamelet library and later on used in the CFD calculation. Figure 4.9 and Figure 4.10 show the profiles of the major (O_2, H_2O, CH_4, CO_2, CO) and minor species (H_2, OH) respectively as a function of the mixture fraction. The solutions of Müller et al. and of Cantera show a qualitative agreement with only a few differences. The Cantera solution shows a slightly larger CO mass fraction, with the discrepancy remaining under 3%. Moreover, in the range between $Z = 0$ and $Z \approx 0.15$, Cantera predicts that the CO_2 concentration exceeds the H_2O one, in contrast to the Flamemaster results. The most significant difference occurs in the mass fraction of H_2, which is underpredicted in the Cantera solution (Figure 4.10). A relative difference of 35% in the maximal value of H_2 is observed, which however has almost negligible effect in the temperature profile, since the H_2 is not so abundant in the domain ($Y_{H_2} < 0.065$). It is important to note, that the two "equilibrium" solutions compared in Figure 4.8 and Figure 4.9 correspond to different values of the scalar dissipation. In the literature solution, equilibrium was considered to be reached at $\chi = 10\,\mathrm{s}^{-1}$, whereas in the Cantera Flamelet

generator $\chi = 0.14\,\mathrm{s}^{-1}$ was the final value. The two methods however also use different definitions for the scalar dissipation: In Flamemaster it is given as a parameter for the solution of Eqs. (2.66)-(2.67), whereas Cantera calculates it *a posteriori* using Eq. (3.2).
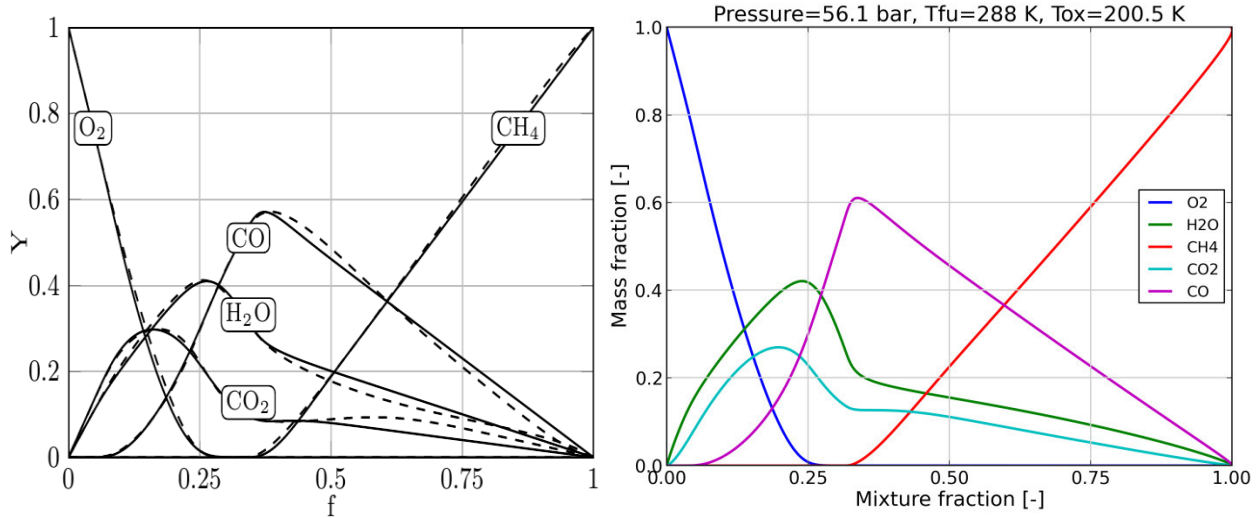
Figure 4.9: Comparison of the major species mass fractions from the Cantera Flamelet generator (right) with results from Müller et al. [55] (left) for 56.1 bar CH_4/O_2 nonpremixed combustion ($\chi \approx 0$).
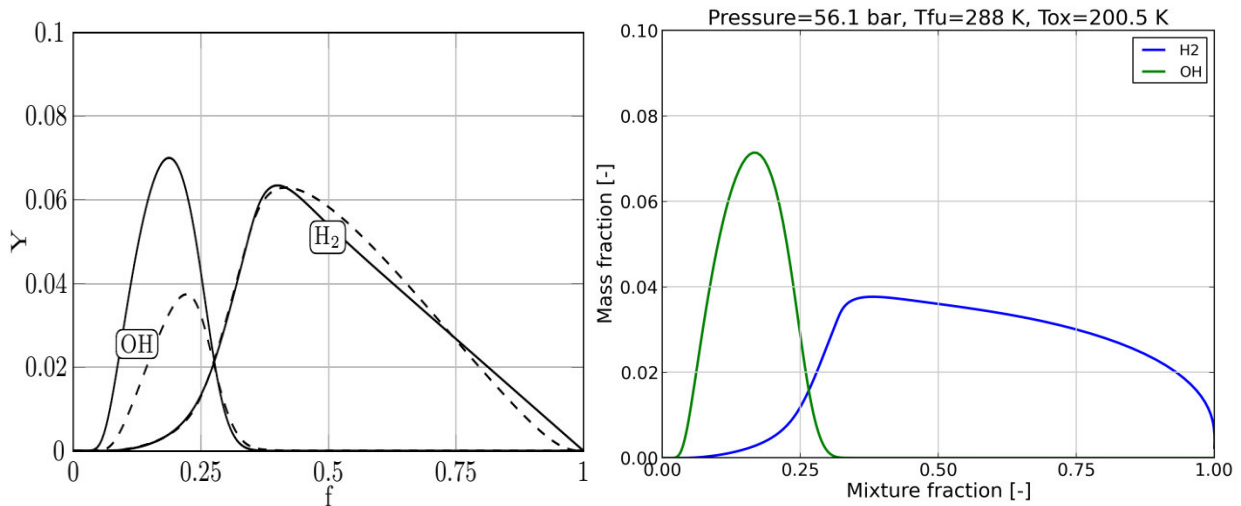
Figure 4.10: Comparison of the minor species mass fractions from the Cantera Flamelet generator (right) with results from Müller et al. [55] (left) for 56.1 bar CH_4/O_2 nonpremixed combustion ($\chi \approx 0$).

Apart from the equilibrium solution, the dependence of the temperature on the scalar dissipation is important in a Flamelet table. For that reason, the maximum temperature occurring in the 1D domain for each value of the scalar dissipation is plotted in Figure 4.11. The two solutions display a qualitative agreement in their form. The point of extinction

shows a measurable difference, since it is predicted at $\chi_q = 3 \cdot 10^5 \, s^{-1}$ by Cantera and at $\chi_q \approx 6 \cdot 10^5 \, s^{-1}$ by Flamemaster. This could be attributed to the different definition of the scalar dissipation, but is of minor importance, since such high values are not relevant for most conventional rocket propulsion applications.
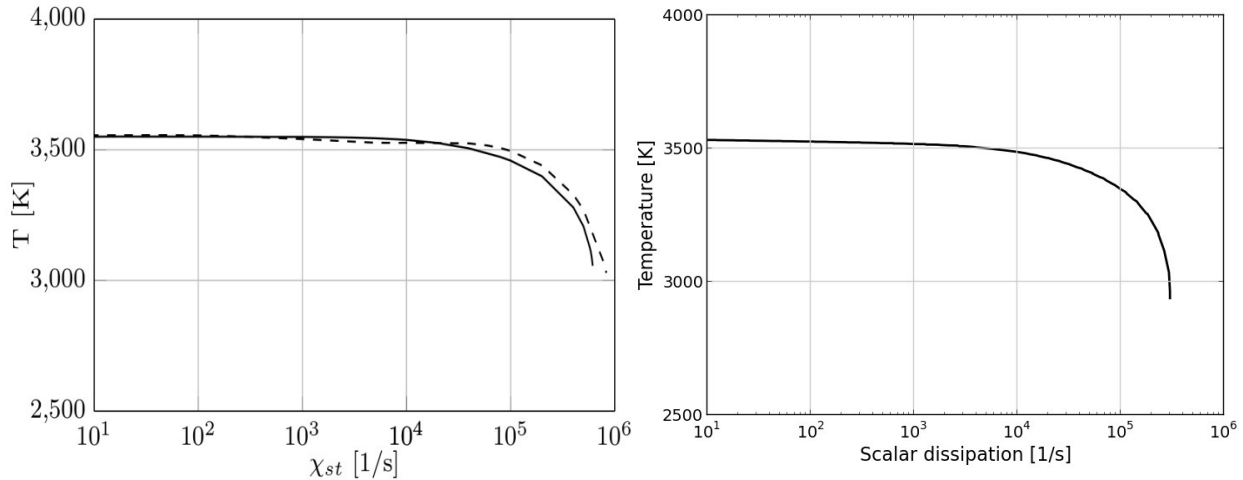
Figure 4.11: Comparison of the maximal temperature from the Cantera Flamelet generator (right) with results from Müller et al. [55] (left) for 56.1 bar CH$_4$/O$_2$ nonpremixed combustion.

4.4 Comparison with H$_2$/O$_2$ combustion

CH$_4$/O$_2$ is a promising propellant combination but some aspects of its combustion characteristics remain unsolved, in contrast to H$_2$/O$_2$ combustion, which is established in the field of space propulsion. For that reason, a comparison between the two propellants is considered to be important in order to gain more insight into the properties of methane.

4.4.1 Flame temperature

The first direct comparison between the chemical properties of the two propellants can be made when examining their temperature dependence on the mixture fraction. This is shown in Figure 4.12. The profiles for different values of the scalar dissipation are plotted, in order to demonstrate the qualitative effect that the departure from equilibrium has on the flame temperature.

It is quite interesting, that opposed to H$_2$/O$_2$, in the case of methane, the temperature curve seems to "flatten" out for higher values of χ, leading to a smoother profile and to the disappearance of the kink described in Section 4.1. Whereas the maximal temperature decreases with higher scalar dissipation, the temperature values for $Z > 0.3$ tend to increase, leading to this more uniform profile. This effect is not present in the case of hydrogen, where a scaling down of the profile occurs with increasing dissipation.

To examine the flame behavior over a wide range of conditions, the maximal temperature of the flame was inspected as a function of the scalar dissipation rate. The comparison between the two propellant combinations is outlined in Figure 4.13 and Figure 4.14.
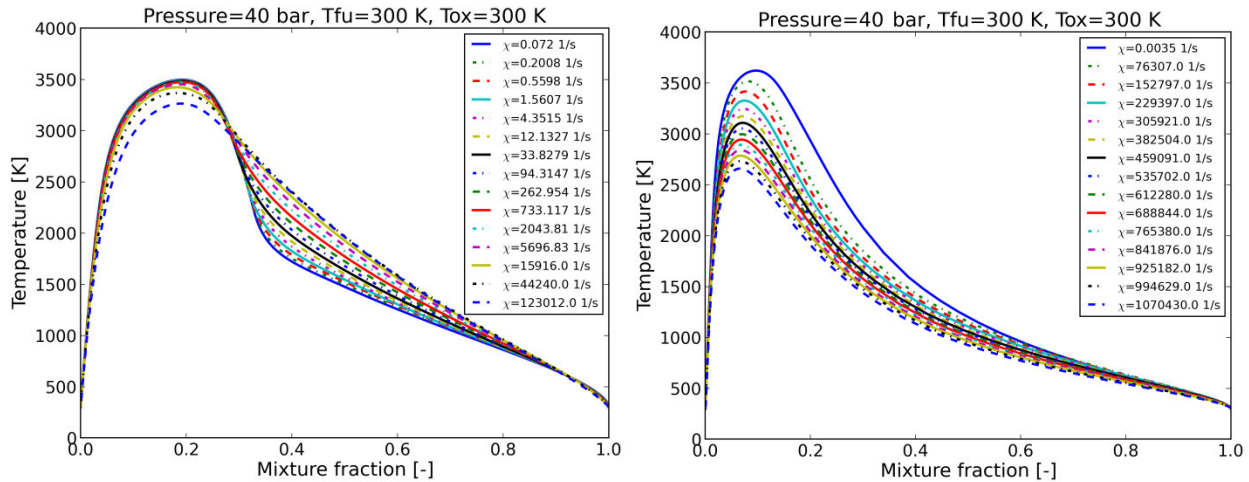
Figure 4.12: Dependence of the flame temperature on the mixture fraction for CH$_4$/O$_2$ (left) and H$_2$/O$_2$ (right) combustion.

As described in Section 3.4.5, the lowest value for the scalar dissipation rate is set at 0.01 s^{-1}. However, in the case of CH$_4$/O$_2$, convergence problems were detected especially for higher pressure levels. For that reason, the methane temperature profiles in Figure 4.13 and Figure 4.14 start from higher values of χ, which is entirely an effect of the Flamelet generation code and not a property of the fuel. It is caused however due to the highly complex reaction mechanism of methane, which makes the convergence of the code more challenging.

Figure 4.13 demonstrates the main differences in the combustion characteristics of the two propellants. First, it can be observed, that the H$_2$/O$_2$ combination has a higher flame temperature for all pressures, which was however expected due to it being more energetic than CH$_4$/O$_2$.

A second observation is that the exctinction point of H$_2$/O$_2$ occurs at higher values of the scalar dissipation rate. This effect is not significant in the RANS simulation of steady state rocket engine operations, since no flame extinction is expected and since the values of the scalar dissipation rate in the chamber are well below χ_q. In the case of LES, DNS and engine startup simulations, the flammability limits play an important role, and hence their knowledge is important for the prediction of certain transient phenomena like flame anchoring at ignition.
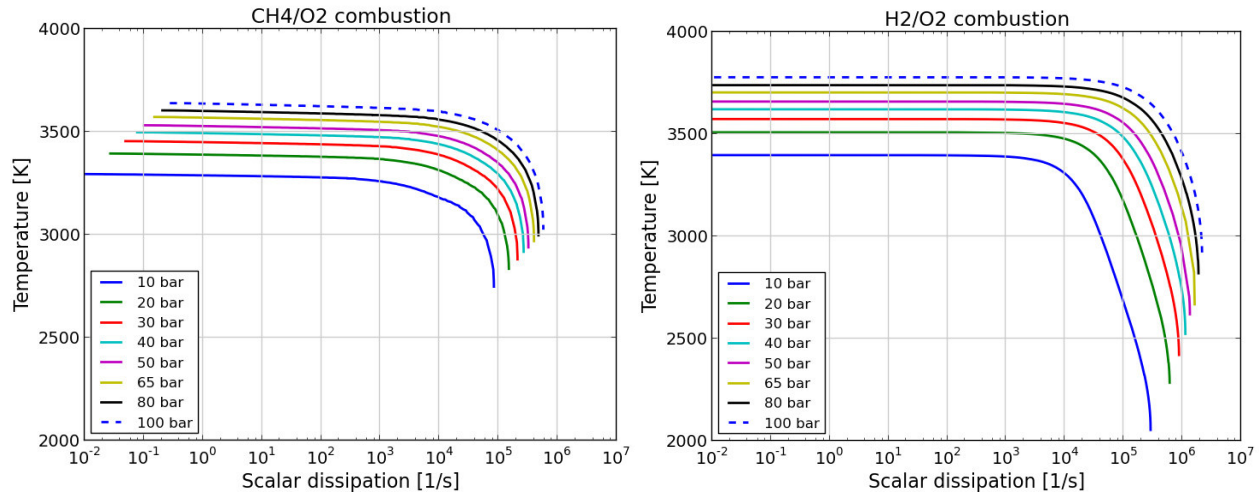
Figure 4.13: Maximal temperature as a function of the scalar dissipation for CH$_4$/O$_2$ (left) and H$_2$/O$_2$ (right) combustion at different pressure levels.
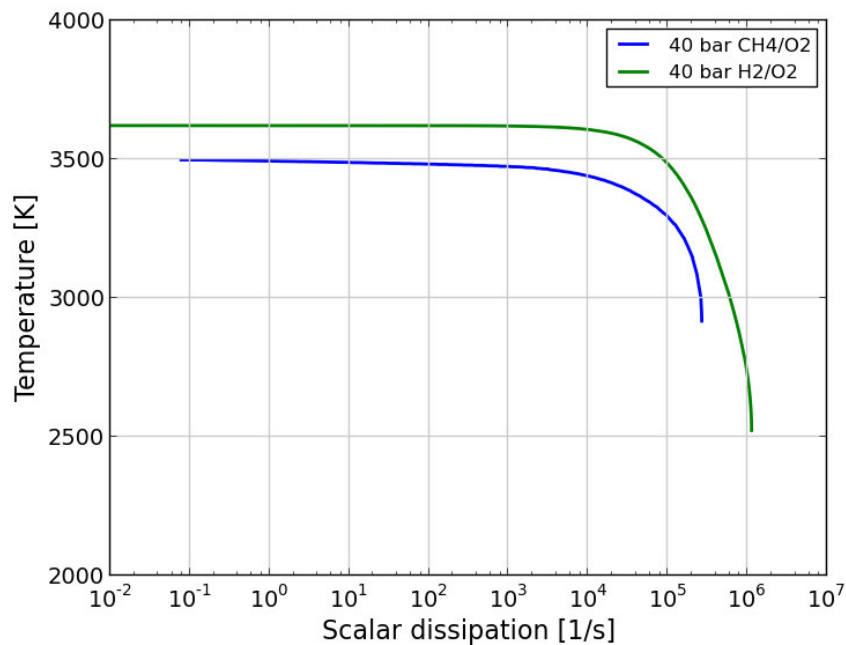
Figure 4.14: Maximal temperature as a function of the scalar dissipation for CH$_4$/O$_2$ and H$_2$/O$_2$ combustion at 40 bar.

Finally, it can be seen that H$_2$/O$_2$ departs from its maximal temperature at much higher scalar dissipation rates compared to CH$_4$/O$_2$. Only after $\sim 3 \cdot 10^3 \, s^{-1}$ in the 40 bar case (Figure 4.14[10]) does the temperature start decreasing due to the non-equilibrium effects. In the CH$_4$ case on the contrary, this happens at approximately $\sim 1 \, s^{-1}$. This serves as a

---

[10] A typical pressure level for space propulsion applications (40 bar) was chosen in Figure 4.14, which serves as a more direct comparison of the effects described above.

justification for the need for Flamelet models when dealing with the simulation of hydrocarbon engines. The separation from the maximal temperature (equilibrium temperature) takes place already at small values for χ, which means that a chemical equilibrium model is not sufficient. For H_2/O_2 rocket engines however, the equilibrium model is justifiable, since the temperature (and gas composition) does not depend so strongly on the scalar dissipation.

4.4.2 Species mass fractions

The discrepancy observed in the temperature profiles of CH_4/O_2 and H_2/O_2 (Figure 4.12) implies different mass fraction distribution as well. Due to the different species taking part in the combustion of the two mixtures, only the mass fractions of molecules being present in both reaction mechanisms can be compared.

To examine the differences between the two propellant combinations, the H_2O and OH mass fractions were plotted, as shown in Figure 4.15 and Figure 4.16. H_2O is a product of the stoichiometric reaction in both the methane and the hydrogen combustion. For that reason, high concentrations (>0.3) are experienced. In the case of H_2/O_2 combustion, the water mass fraction can reach up to 0.9 close to the stoichiometric point, whereas in the CH_4/O_2 case, it remains below 0.45, due to the presence of CO_2, which is also a product.

A notable difference is the shape of the curves for small values of the scalar dissipation. In the case of methane, a kink is formed close to equilibrium conditions, which is absent in the H_2/O_2 combustion. This effect is also responsible for the measurable difference in the shape of the temperature curve.

The OH profile on the other hand is very similar for both cases. Again, the magnitude of the mass fraction in the case of hydrogen is slightly higher. This is due to the more complex mechanism for the hydrocarbon combustion, through which OH can undergo further reactions, leading to a reduction of its concentration. Despite the differences observed in the form of the curves and the absolute concentrations, both propellant combinations have their maxima close to the stoichiometric mixture fraction (0.2 for methane and 0.11 for hydrogen), as expected.

After understanding these basic properties of the methane Flamelet tables, their implementation in 3D CFD simulations was carried out.
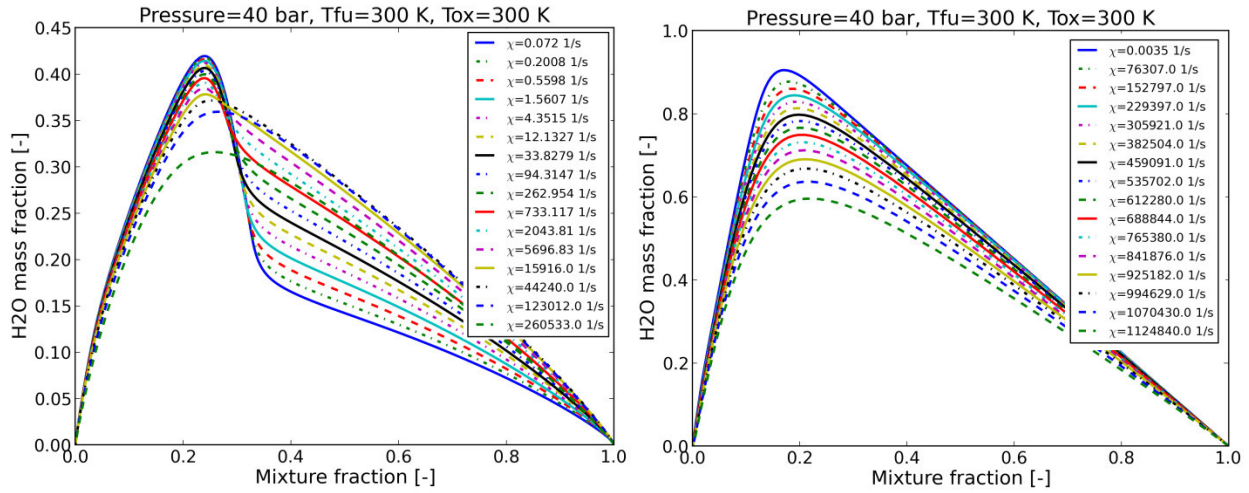
Figure 4.15: H₂O mass fraction as a function of mixture fraction at 40 bar for CH₄/O₂ (left) and H₂/O₂ (right) combustion.
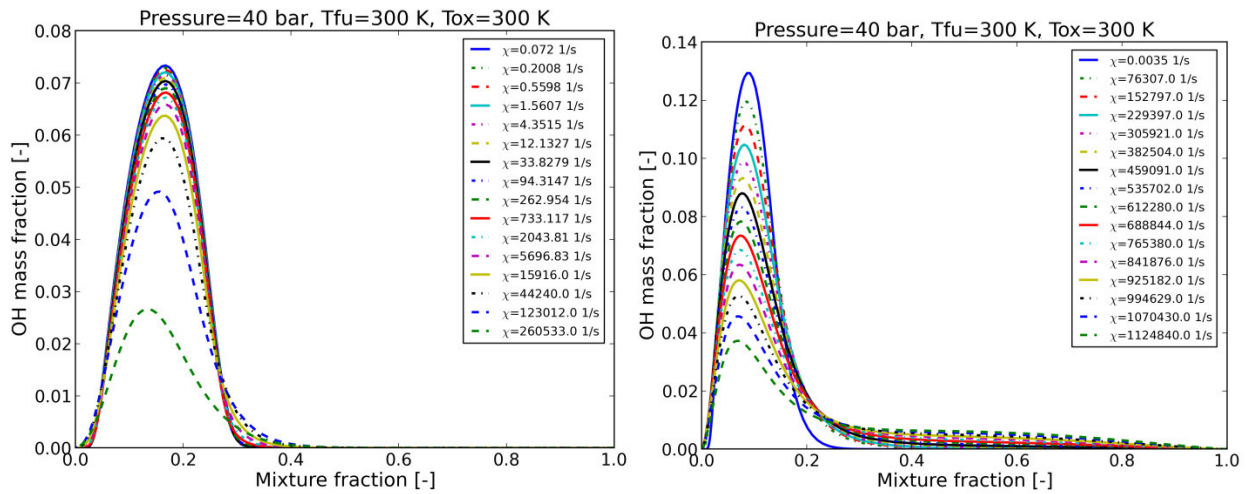
Figure 4.16: OH mass fraction as a function of mixture fraction at 40 bar for CH₄/O₂ (left) and H₂/O₂ (right) combustion.

5 Numerical simulation and results with CFX

To examine the validity of the Flamelet tables, two test cases of CH_4/O_2 combustion in rocket engines were simulated. The two load points differed regarding their geometry and their operational point. The results for a GOX/GCH$_4$ case (ISP-1 test case, described in Section 5.1) as well as a subcritical LOX/GCH$_4$ case (Romeo thrust camber, described in Section 5.2) were calculated. In order to highlight the properties of each load point, the inlet temperature and combustion chamber pressure for the oxidizer and the fuel are plotted in a p-T diagram for each of the two test cases. To account for the different critical points of methane and oxygen, the reduced temperature and pressure are used, defined as:

$$T_{red} = \frac{T}{T_{crit}} \tag{5.1}$$

$$p_{red} = \frac{p}{p_{crit}} \tag{5.2}$$

The critical properties of methane and oxygen are summarized in Table 5.1, and the saturation line can be seen in Appendix G.

Table 5.1: Critical properties of methane and oxygen.

Fuel	Critical pressure	Critical temperature
Methane	45.99 bar	190.56 K
Oxygen	50.43 bar	154.58 K
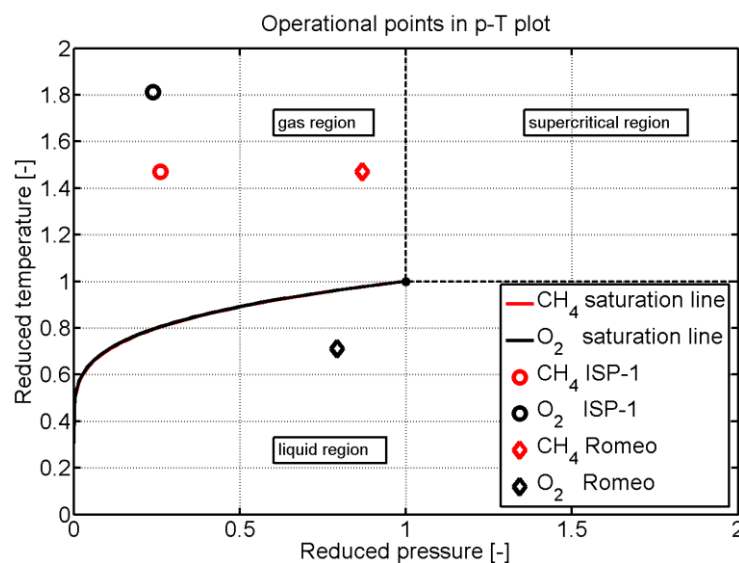
Figure 5.1: Operating points for the ISP-1 and Romeo test cases in a reduced p-T diagram.

5.1 ISP-1 test case

In the frame of the European Framework Program FP7, the In-Space Propulsion (ISP-1) project was initiated in 2009 with the objective of improving the knowledge and the techniques which are required to develop cryogenic propulsion systems for future missions [58]. This three years project started in September 2009 and closed in August 2012 and dealt with various technological issues associated to the development of low thrust cryogenic propulsion systems as well as launchers' upper stages.

The subjects addressed in the project were mainly LOX-methane combustion, the energy management of low thrust propulsion systems, the material compatibility and tribology in liquid oxygen, the hydrogen embrittlement, and the development of electrically driven cryogenic turbopumps [59].

5.1.1 Case description

Within the ISP-1 project, tests have been performed at the P6.1 research test facility at DLR Lampoldshausen with the DLR sub-scale combustion chamber model B. The purpose of this chamber's operation was focused on the generation of an experimental database for the verification of the numerical tools concerning O_2/CH_4 combustion. Specifically, the determination of the thermal loads, being one of the most significant investigations in subscale combustion chambers, was put into spotlight.

For this reason, the combustion chamber model B was designed with a calorimetric measurement method, which uses the water cooling cycle in order to calcsulate the thermal loads. As illustrated in Figure 5.2, the combustion chamber is divided in 5 separate segments. Each one of the segments has a length of 50 mm and possesses its own cooling cycle, with a water flow inlet and outlet. By measuring the temperature and pressure of the water at the inlet and the outlet of the cooling manifold, the difference in enthalpy can be calculated, which corresponds to the energy release in this segment of the chamber. With the knowledge of the contact area between water and combustion chamber, the average heat flux for this segment can be obtained. In the case of the nozzle, the radius of the contour does not remain constant and hence, the average heat flux is not scientifically relevant. Instead, only the heat release is measured [59].

The chamber has a length of 250 mm, and a radius of 25 mm. The nozzle consists of a converging and a diverging part (Laval nozzle), with changeable throat. In the configuration examined in Suslov [59], a throat diameter equal to 28 mm is present, leading to a

contraction ratio equal to 3.2[11]. A sketch of the thrust chamber's dimensions is given in Figure 5.3.

The injector head contains an igniter located in the center and 15 coaxial injectors without recess. 10 injectors are placed on an outer circle with diameter 38 mm, and the other 5 ones are located on an inner circle with diameter equal to 19 mm. This pattern design provides a smooth distribution on the local combustion zones and was chosen in order to achieve uniform thermal loads on the hot gas surface of the combustion chamber wall [59], [60]. Each coaxial injector has an inner diameter of 3 mm for the flow of the oxidizer and an annular ring with 4.8 mm outer and 4 mm inner diameter for the flow of the gaseous methane. The configuration of the injector head is shown in Figure 5.4.
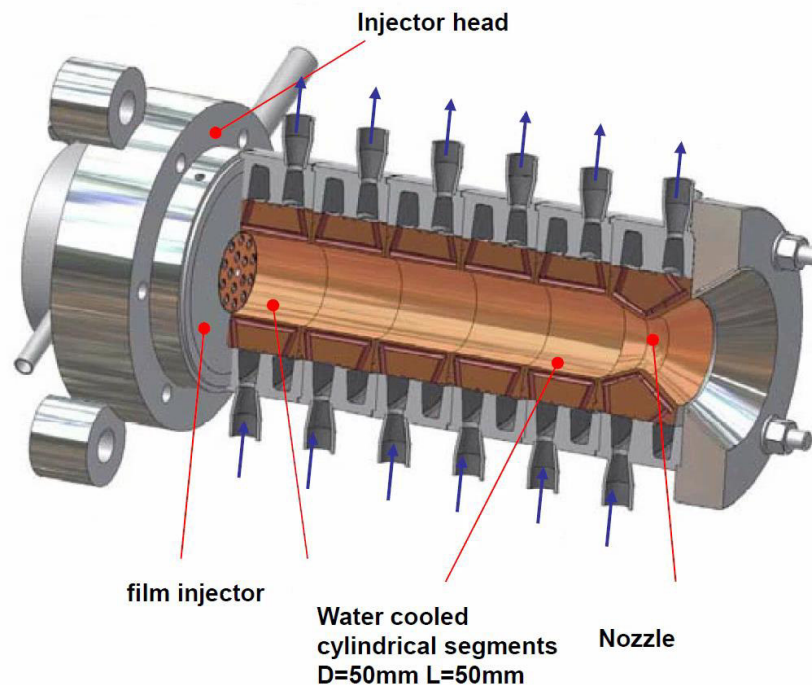
Figure 5.2: Combustion chamber model B of the ISP-1 project from Suslov [59].

The chamber was operated with gaseous oxygen and methane injected at ambient temperature. A low pressure regime was chosen, ranging from 10 to 12 bar. The testing campaign included experiments with methane film cooling, as well as reference cases without the use of film cooling. In the present thesis, a 10 bar case with oxidizer to fuel ratio equal to 3.35 is presented. Further information about the operating point is given in Table 5.2.

---

[11] The contraction ratio is defined as the ratio of the chamber cross section to the throat cross section.
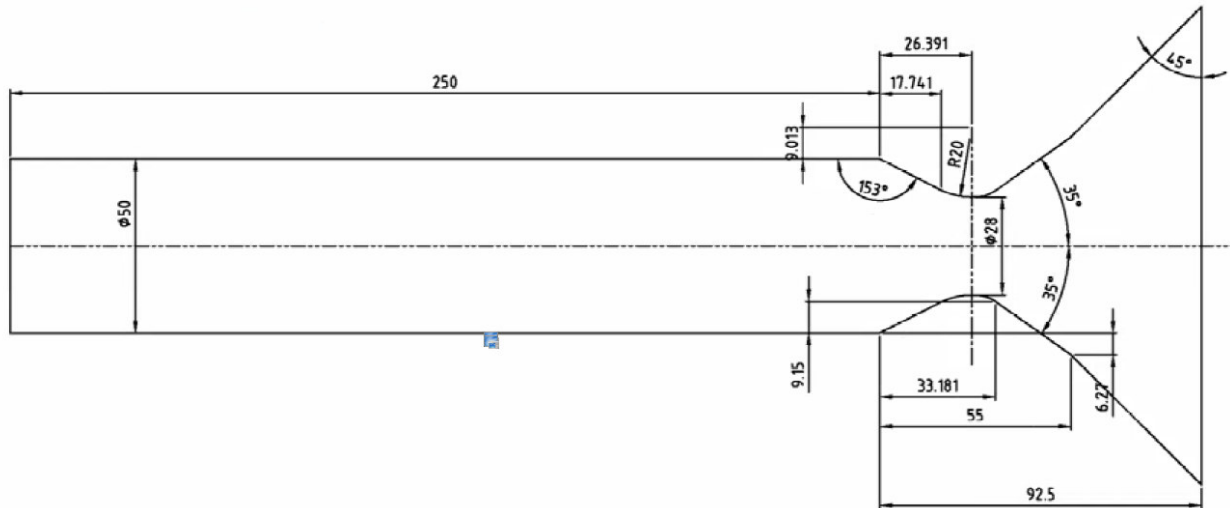
Figure 5.3: Sketch of the ISP-1 thrust chamber from Suslov [59].
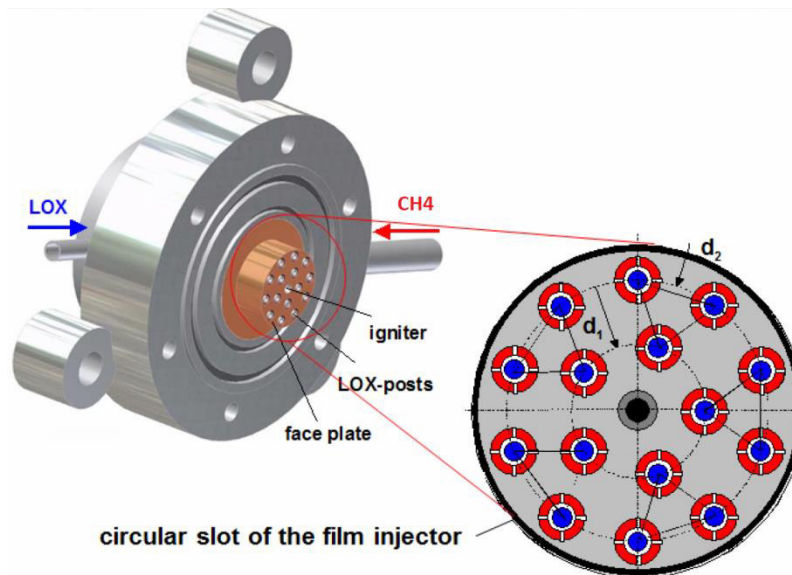
Figure 5.4: Injector head of the subscale combustion chamber B from Suslov [59].

Table 5.2: Operating point of the ISP-1 test case.

Pressure	10 bar
O/F	3.35
Oxygen mass flow rate	280.00 g/s
Methane mass flow rate	83.59 g/s
Oxygen inlet temperature	280 K
Methane inlet temperature	280 K

5.1.2 CFX setup

For the CFD simulation, ANSYS CFX was utilized and the computation took place in a 3D domain. In order to take advantage of the thrust chamber's symmetry, only a tenth of the ISP-1 engine was modeled. The corresponding geometry hence consisted of a 36° segment in azimuthal coordinate, as shown in Figure 5.5. In the same figure, the mesh of the injector element is illustrated. A structured mesh with approximately 2.45 million cells was used. The mesh was developed in the framework of a previous analysis (presented in Riedmann et al. [61]), so no mesh convergence testing was performed. The wall vicinity was resolved, so as to obtain y+ values smaller than 1 in the cells directly on the boundary.

A mass flow inlet was defined both for the oxidizer and the fuel inlets, whereas a pressure outlet was implemented at the nozzle exit. The reference pressure of the outlet was set at 0.1 Pa, a value which is however irrelevant for the converged solution, since the flow in the nozzle's divergent part is supersonic. For the planes at -18° and 18°, a symmetry boundary condition was applied. The faceplate wall was defined as adiabatic, whereas for the hot gas wall of the chamber, the temperature measured by the thermocouples was defined as a thermal boundary condition. The measured temperature profile can be seen in Figure 5.6. Finally, the roughness of the hot gas wall was set to 3.6 microns, a value which results from the experimental measurement and an additional correction to account for the chamber's duration of operation. All walls are defined as no slip walls.
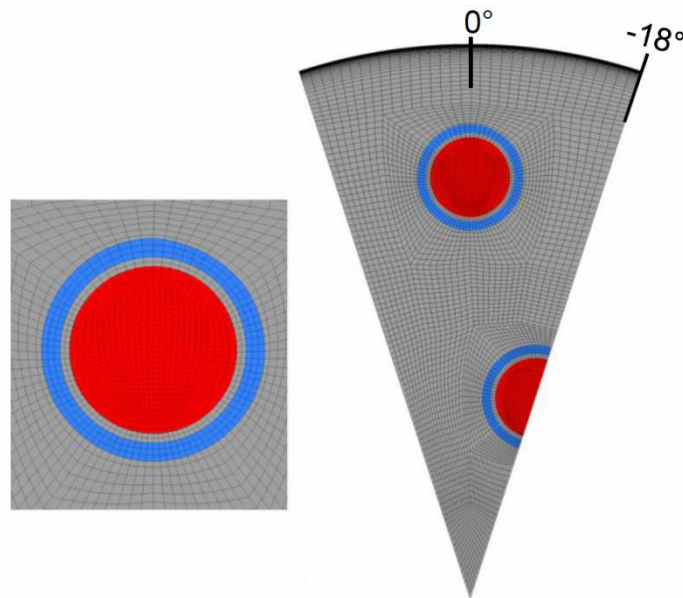
Figure 5.5: Injection element meshing for the CFX simulation of the ISP-1 test case from Riedmann et al. [61] (red: oxygen inlet, blue: methane inlet, grey: adiabatic wall).
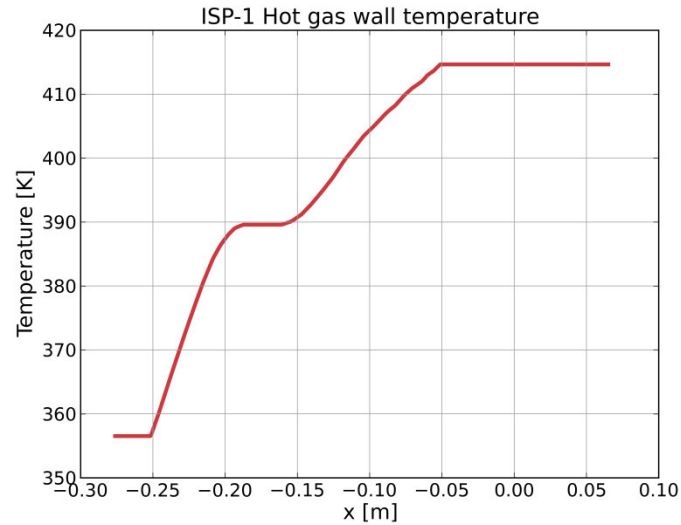
Figure 5.6: Wall temperature of the ISP-1 thrust chamber.

For the thermodynamic properties of the gas components, the NASA polynomials were used. The effect of the transport properties on the final result was examined, as shown in Section 5.1.3. The effect of constant values for λ, μ for each species was compared to the temperature dependent definition of λ, μ, i.e. $\lambda, \mu = f(T)$. Ideal gas and kinetic theory mixture laws for the transport properties were also compared to each other.

Finally, another parameter which underwent an analysis based on its influence on the wall heat flux, was the turbulent Prandtl number Pr_t. Since it poses the closure of the heat flux in the RANS equations, as shown in Eqs. (2.51) and (2.53), it directly affects the wall heat transfer.

5.1.3 Results

The first step before undertaking the CFD simulation of the ISP-1 engine was to compare the tables produced by CFX RIF with the ones from Cantera using the visualization tool TecPlot360. The two tables showed many similarities and a detailed comparison is given in Appendix E.

The CFX RIF table was tested first. The baseline solution with this table was carried out with the simplest possible setting, i.e. constant transport properties over temperature and an ideal (mass averaged) mixing law. The turbulent Prandtl number was set to be equal to 0.6. The second simulation involved adding a temperature dependency in the values of the transport properties (Eq. (2.29)), while keeping the remaining settings intact. The next step was to involve the effect of the kinetic theory mixing, which is described by Eqs. (2.30)-(2.34).

It was observed, that the additional modeling effort of the more complex kinetic-gas mixing substantially increased the computational time, without having a major impact on the results. For that reason, it was dismissed from further analysis. The final simulations included a variation of the turbulent Prandtl number ($Pr_t = 0.7$), while preserving the temperature dependence of the transport properties and the ideal mixing.

The wall heat flux profiles for the five cases are shown in the left subfigure of Figure 5.7 along with the experimental measurements. In order to perform a better comparison with the experimental values, the averaged profiles over each segment were calculated and are also illustrated in the right subfigure of Figure 5.7[12].
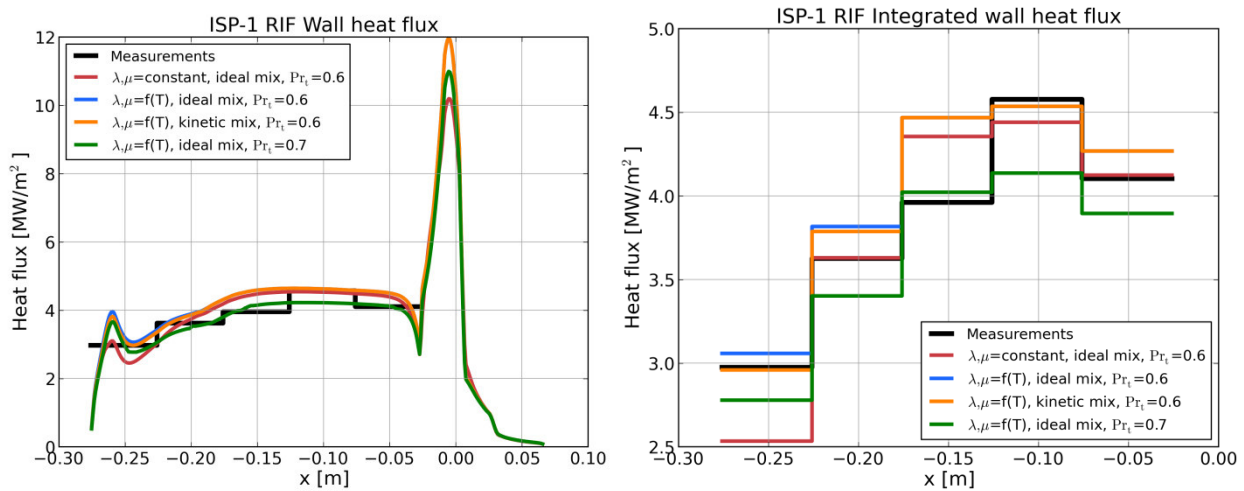
Figure 5.7: Heat flux profiles (left) and averaged heat flux profiles (right) for the ISP-1 chamber using the CFX RIF Flamelet tables.

All profiles show the same trend: The heat flux increases within the first segment up to a maximum before dropping again. The nature of this local maximum will be elaborated on later in this section, based on Figure 5.22. In the second half of the first segment (x>-0.25 m), a further increase is observed, which perpetuates up to the third segment. This increase seems to slow down and the heat flux appears to reach a plateau near the middle of the third segment, which indicates the end of combustion. Just before the beginning of the nozzle segment, a sharp drop is again observed. This drop is easily explained when observing the contour of the chamber in Figure 5.3. The interface between

---

[12] Clarification of the legend in the following figures:
- λ, μ = constant: temperature independent values for transport quantities
- $\lambda, \mu = f(T)$: temperature dependent values for transport quantities
- Ideal mix: ideal (mass averaged) mixing rule for transport quantities
- Kinetic mix: kinetic gas theory (Eqs. (2.30)-(2.34)) mixing rule for transport quantities

combustion chamber and nozzle has a sharp edge, without a smoothing radius. For that reason, the hot gas is strongly accelerated in this region, leading to a short drop in pressure and hence a rarefication of the boundary layer and reduced heat transfer to the wall. This sharp drop has an effect on the segment-averaged heat flux as well, as can be seen in the left subfigure of Figure 5.7, where the heat flux in the fifth segment is lower than the one in the fourth. This also agrees with the experimental measurements (black line) and hence makes the assumption of the heat flux decrease due to the sharp edge plausible.

For a more quantitative comparison among the simulations, a metric has been defined in order to represent the accumulated disagreement between experimental and calculated value for the five (5) segments of the chamber:

$$J = \sqrt{\frac{\sum_{i=1}^{5}(\dot{q}_{i,calc} - \dot{q}_{i,meas})^2}{5}}$$ (5.3)

It can be interpreted as the average error of each simulation and therefore lower values for J correspond to better agreement. Equivalently, a metric for the relative error is defined as:

$$J_{rel} = \sqrt{\frac{\sum_{i=1}^{5}\left(\frac{\dot{q}_{i,calc} - \dot{q}_{i,meas}}{\dot{q}_{i,meas}}\right)^2}{5}}$$ (5.4)

The results for the simulations using the RIF tables are given in Table 5.3.

Table 5.3: Comparison of heat flux agreement with experimental data for the simulation of ISP-1 using the CFX RIF tables.

Simulation settings	Metric J [MW/m^2]	Metric J_{rel} [%]
RIF table, λ, μ = constant, ideal mix, $Pr_t = 0.6$	0.272	8.11
RIF table, $\lambda, \mu = f(T)$, ideal mix, $Pr_t = 0.6$	0.257	6.57
RIF table, $\lambda, \mu = f(T)$, kinetic mix, $Pr_t = 0.6$	0.250	6.33
RIF table, $\lambda, \mu = f(T)$, ideal mix, $Pr_t = 0.7$	0.258	6.59

It can be observed, that even the simplest model (constant transport quantities) achieves a good agreement with the experimental (red line). The modeling assumption of temperature independent conductivity and viscosity is however physically non-intuitive and its satisfactory agreement with the experimental data is limited only to the last four (4) segments of the chamber. In the first segment, an underestimation of the heat flux is observed. This is attributed to the fact that the laminar transport properties are more

dominant close to the injector than further downstream. In the first segment, where the effect of turbulent conductivity is minor, the heat flux is underestimated because a much lower conductivity is used. The temperature at the wall can reach up to 500 K (Figure 5.10) in this region, whereas the model still utilizes the thermal conductivity values at 280 K. For example methane, which is abundant close to the faceplate, has a thermal conductivity of 0.033 W/(m·K) at 280 K and 0.067 W/(m·K) at 500 K. This sharp increase is true for other species as well and in the absence of a significant turbulent conductivity, the effect on the heat flux is dominant. For locations further downstream, where the turbulent thermal conductivity plays a more important role, the results obtained with the simple model, tend to approach the ones with variable transport quantities.

The results for the temperature dependent transport properties demonstrate the smallest deviation from the measurements. The first profile tested was for an ideal mixing, with the same turbulent Prandtl number equal to 0.6 (blue line). The heat flux matches the experimental values for the first segment with sufficient accuracy but then reaches much higher values than the measurements in the third segment, going up to 4.4 MW/m^2 compared to the measured 3.9 MW/m^2. Using the same temperature dependent conductivity and viscosity as well as the same Prandtl number, but with the kinetic gas mixing rule (orange line) produces virtually identical results as with the ideal-gas mixing rule. A minimal difference is observed only in the first segment. Since the computational effort required for the kinetic theory mixing is much higher, and the outcome did not improve the accuracy, this model was dismissed from further examination in the ISP-1 test case.

In general, the $Pr_t = 0.6$ simulations showed a sufficient agreement with the measured data but also a slight overestimation of the heat flux in the second and third segment. In order to potentially improve this discrepancy, the turbulent Prandtl number was modified. Since a value of 0.6 produced too high a value for the heat flux, it was increased to 0.7, which translates to a decrease in the turbulent heat conductivity. Hence the heat diffusion into the wall was expected to be lower. This effect was indeed observed, with the $Pr_t = 0.7$ simulation showing a significant decrease in heat flux compared to $Pr_t = 0.6$. In the first segment, the difference between the two solutions is still small, since the effect of the turbulent thermal conductivity is restricted and hence the heat flux is mainly determined by the laminar properties. For positions further downstream (segments 4-5) however, the predicted heat flux obtained much lower values than the measured ones. This lead to the $Pr_t = 0.6$ and $Pr_t = 0.7$ results having almost identical error metric (Table 5.3). The optimal solution was hence believed to lie at approximately $Pr_t = 0.65$.

For the simulation using the Cantera-generated Flamelet tables, only two settings were examined: temperature dependent transport properties with an ideal gas mixing and

$Pr_t = 0.6$ and $Pr_t = 0.7$ respectively. The simulation with temperature independent transport quantities was not carried out, since it is not motivating from a physical standpoint. The gas kinetic mixing rule was also avoided as explained, due to the longer computational time. The heat flux profiles and heat flux errors for the Cantera tables using the GRI 3.0 mechanism are shown in Figure 5.8 and Table 5.4.
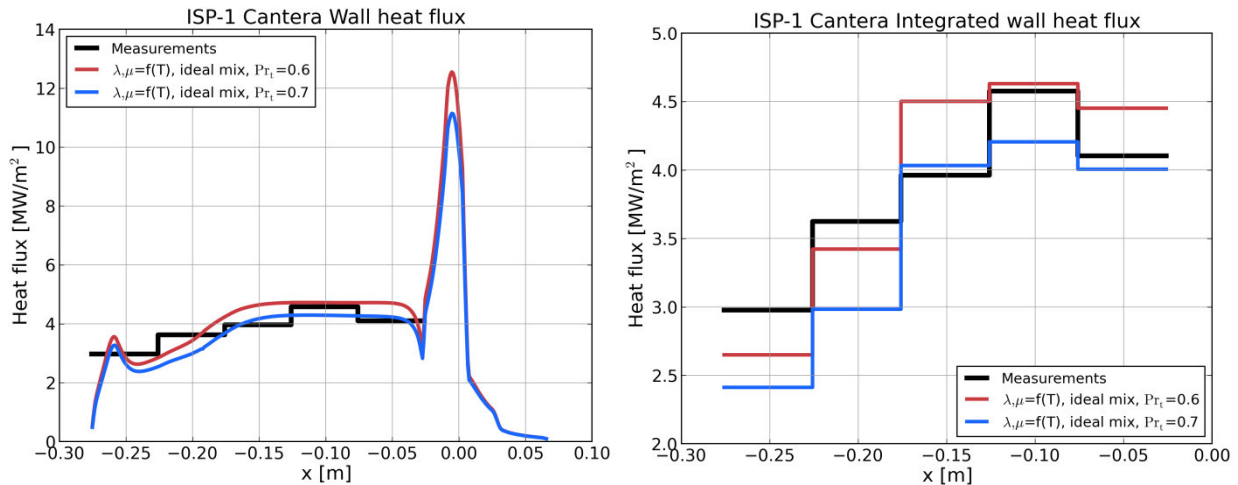
Figure 5.8: Heat flux profiles (left) and averaged heat flux profiles (right) for the ISP-1 chamber using the Cantera Flamelet tables.

Table 5.4: Comparison of heat flux agreement with experimental data for the simulation of ISP-1 using the Cantera tables.

Simulation settings	Metric J [MW/m^2]	Metric J_{rel} [%]
Cantera table, $\lambda, \mu = f(T)$, ideal mix, $Pr_t = 0.6$	0.334	9.06
Cantera table, $\lambda, \mu = f(T)$, ideal mix, $Pr_t = 0.7$	0.420	12.22

It is evident that the solution using the Cantera table and a turbulent Prandtl number equal to 0.6, produces the results with the best agreement. It is a reassuring result that both the RIF and Cantera simulations have an optimal solution for $Pr_t = 0.6$, since it is important that the chosen turbulent Prandtl number remains consistent for a specific propellant combination. The form of the heat flux profile stemming from the Cantera simulation is quite similar to the one of the RIF tables. For a direct comparison, the results from the simulation with the RIF table and the Cantera table for the same settings ($\lambda, \mu = f(T)$, ideal mix, $Pr_t = 0.6$) are plotted in Figure 5.9.
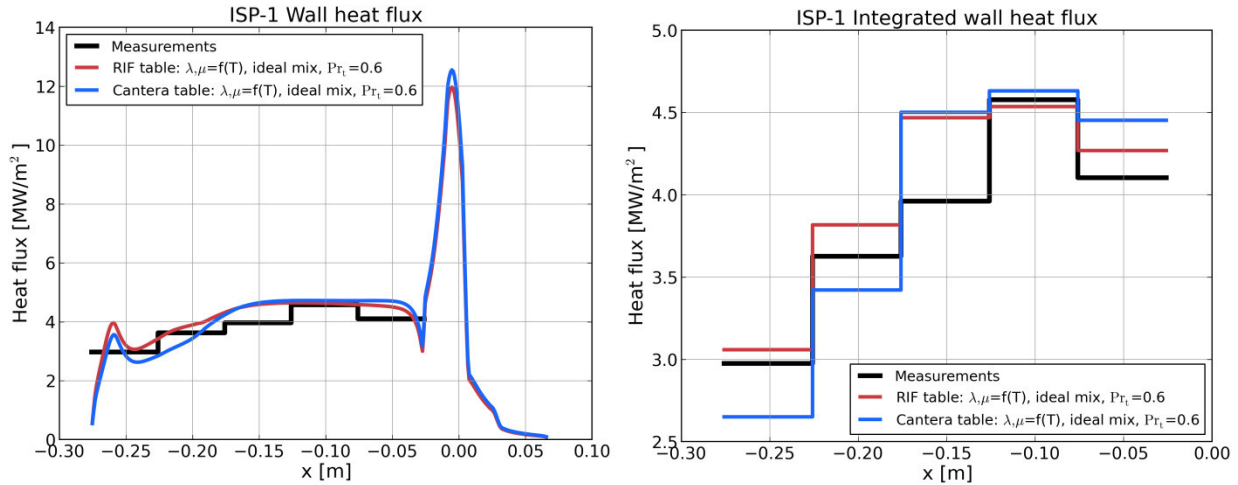
Figure 5.9: Comparison of heat flux profile using the RIF and the Cantera Flamelet tables for the ISP-1 chamber.

The main difference occurs in the first two segments of the chamber, where the Cantera results underpredict the heat flux values. In order to qualitatively understand this disagreement and be able to identify the main differences between the two tables, the profiles of some characteristic flow and material variables were examined at the thrust chamber wall. The heat flux is directly connected to the thermal conductivity and temperature of the hot gas at the wall location and hence these two quantities are compared in Figure 5.10.
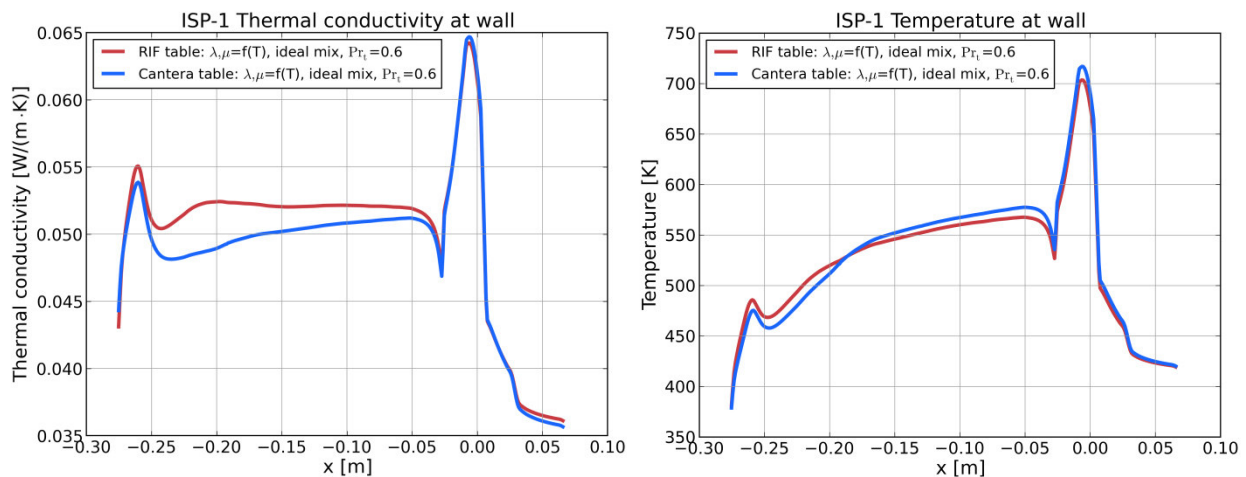
Figure 5.10: Thermal conductivity (left) and gas temperature (right) profiles at the chamber wall for the ISP-1 test case.

The temperature profiles for both the RIF and the Cantera simulations are very similar, whereas the thermal conductivity demonstrates a larger discrepancy in the first three segments which progressively decreases further dowstream. The thermal conductivity is a function of the gas composition and therefore, it is expected that the gas mixture mass

fractions, i.e. the values obtained by the Flamelet table, differ in the two simulations. This can imply that either the input values of the tables, specifying the gas state (mixture fraction, mixture fraction variance and scalar dissipation rate) or the tabulated values themselves are responsible.

The mixture fraction and scalar dissipation profiles at the wall of the thrust chamber (Figure 5.11) show that the input variables of the Flamelet tables are almost identical for both simulations and hence the observed discrepancy must be a consequence of different tabulated values for the species' mass fractions.
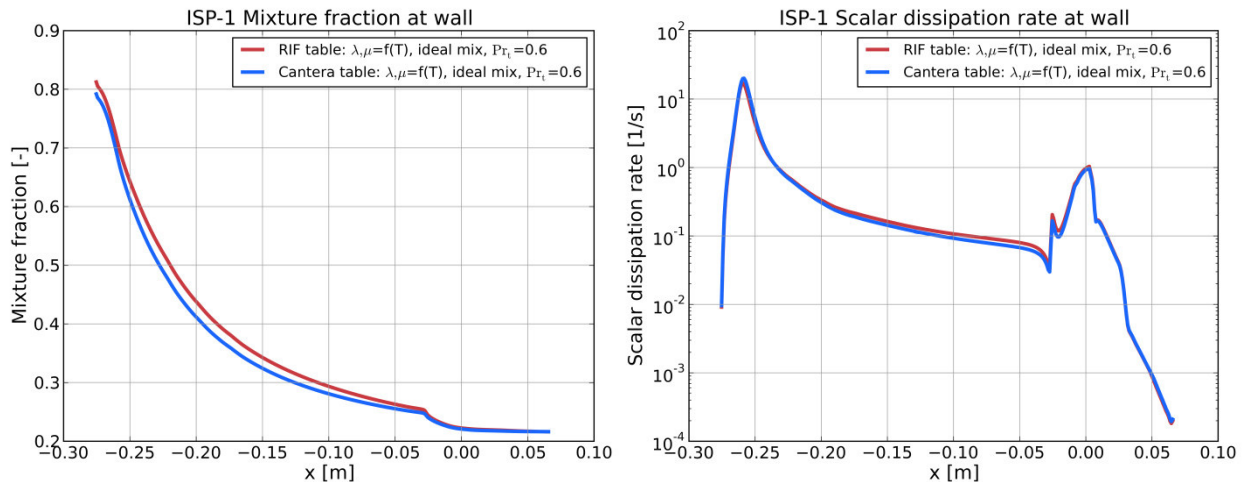
Figure 5.11: Mixture fraction (left) and scalar dissipation rate (right) profiles at the chamber wall for the ISP-1 test case.

This assumption was confirmed when the tabulated mass fractions were closely examined. In Figure 5.12, the mass fractions of the major species are plotted for $\chi = 1\,\text{s}^{-1}$. A comparison of the Cantera and RIF values occurs at $Z = 0.5$, which corresponds to mixture fraction values within the first two segments of the chamber. The mass fractions of CO and H_2O show a significant divergence: The Cantera table predicts a larger value for the CO mass fraction and a higher value for the H_2O fraction compared to the RIF one. This is actually observed in the CFD results as well, as shown in Figure 5.13, where the mass fractions of CO and H_2O directly at the hot gas wall are plotted along the axis.
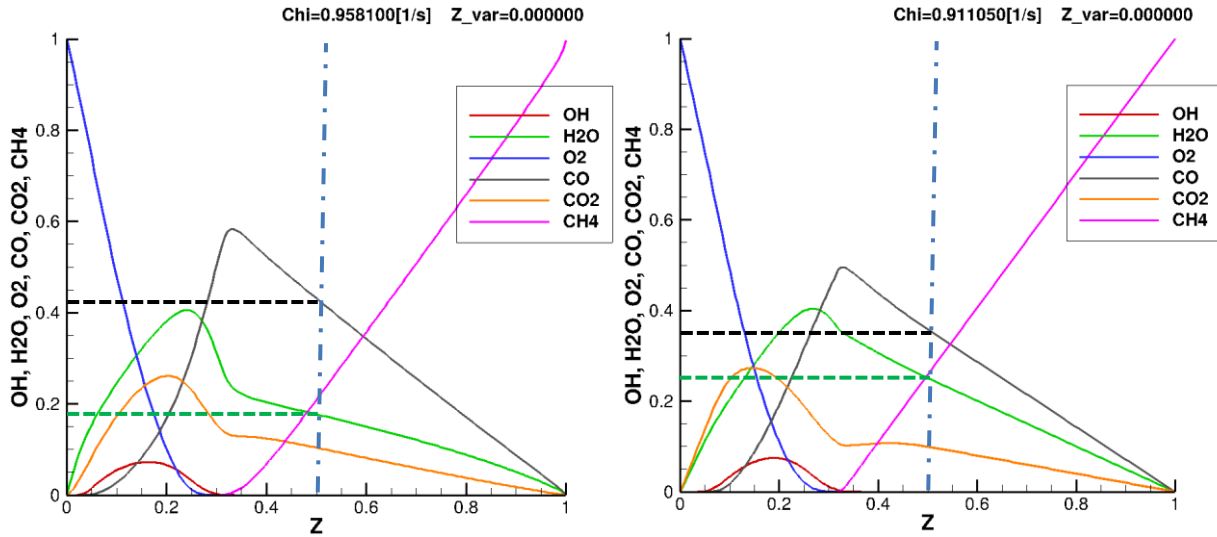
Figure 5.12: Flamelet table mass fractions for the ISP-1 test case: $\chi = 1 \, s^{-1}$, $\widetilde{Z''}_{norm} = 0$ (Cantera table: left, RIF table: right)
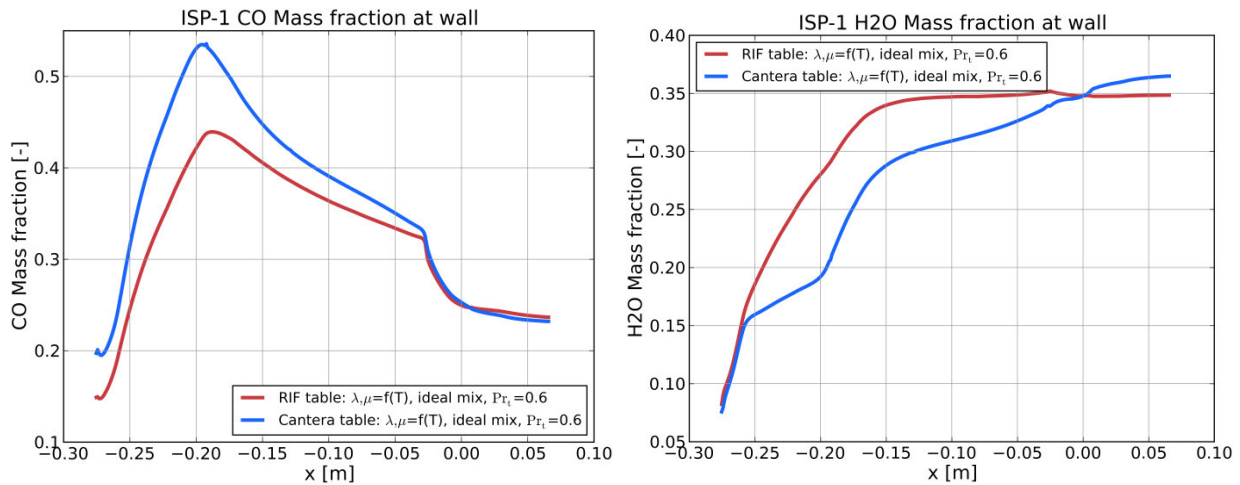
Figure 5.13: CO (left) and H_2O (right) mass fractions at the chamber wall for the ISP-1 test case.

This is indeed also the source of the observed contrast between the RIF and Cantera heat flux results. As Figure 5.14 displays, H_2O has a much larger thermal conductivity compared to CO for a wide temperature range. The higher H_2O mass fraction predicted in the RIF simulation is hence the source of the larger thermal conductivity of the gas mixture at the wall. This is also the main cause for the observed difference in the heat flux.

A further slight distinction between the two simulations is noted at the maximal value of the heat flux in the location of the nozzle throat. There Cantera predicts a slightly higher value, but this effect cannot be analyzed with respect to its validity, since no measurements are available at this location.
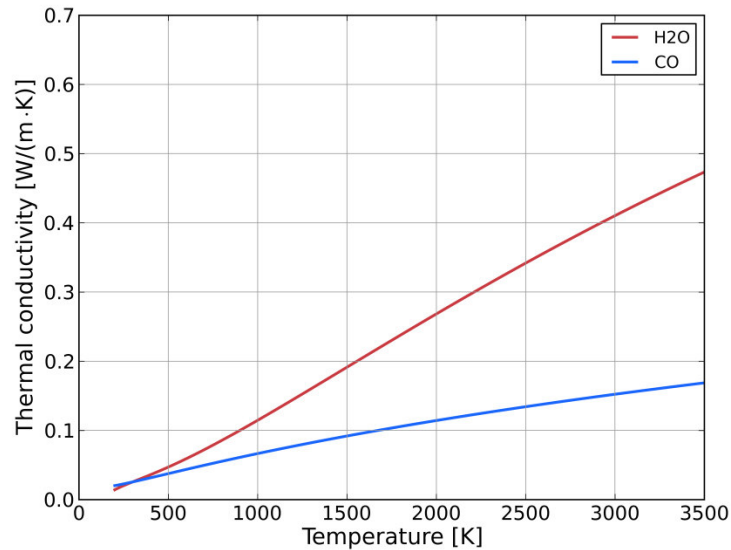
Figure 5.14: Thermal conductivity of H$_2$O and CO as a function of temperature.

Moreover, the experimental values provide information only for the average heat flux of one segment, so there is no insight about the azimuthal distribution of the heat flux. Nontheless, in order to examine the difference in the heat flux results between the two Flamelet libraries, the heat flux profile along the circumferential direction of the chamber was investigated. Six (6) planes were included at following locations: x=-0.270 m, x=-0.226 m, x=-0.176 m, x=-0.126 m, x=-0.076 m, x=-0.026 m. The respective profiles for the Cantera and RIF libraries are shown in Figure 5.15.

One can observe, that up to the 3rd plane (x=-0.176 m, orange line), the two tables provide similar results. The profiles show a maximum close to the 0° mark, which is due to the injector element located at the outer ring. The effect of the second injector element, located at -18° on the inner ring however is damped, due to the larger distance between the injector and the wall, leading to a symmetric profile. Starting on the 4th plane downstream of the injector however, a qualitative difference compared to the positions closer to the injector is observed. Both the Cantera and the RIF results have a local minimum at 0°, accompanied by two local maxima left and right to it, with the effect in the Cantera simulation being more dominant. This "caving in" of the profile can be attributed to the cold oxygen from the injector main jet coming in contact with the wall, thereby temporarily decreasing the gas temperature and leading to this local decrease in the heat flux.

This is indeed verified when inspecting the O$_2$ mass fraction at the wall, as presented in Figure 5.16. It is visible in the left subfigure, that the O$_2$ mass fraction becomes significant at locations downstream of -0.15 m both for the Cantera and the RIF tables. Finally, as the right subfigure proves, the O$_2$ is mainly located close to 0° and its concentration is much

lower at higher azimuthal locations, which is compliance with the local minimum illustrated in Figure 5.15.
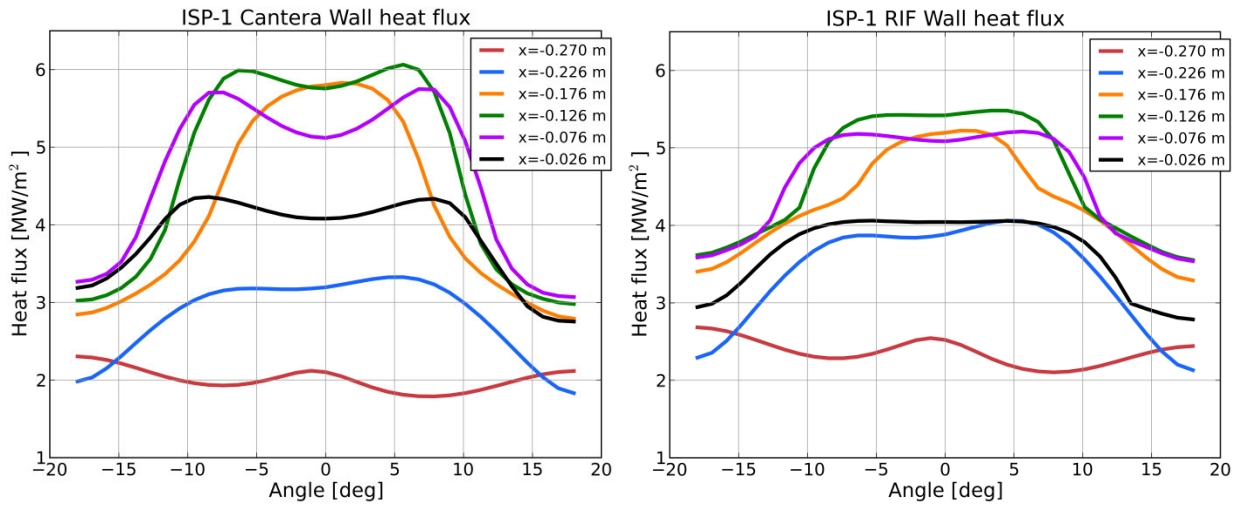
Figure 5.15: Azimuthal heat flux profile in the ISP-1 combustion chamber for the Cantera (left) and RIF (right) Flamelet results.
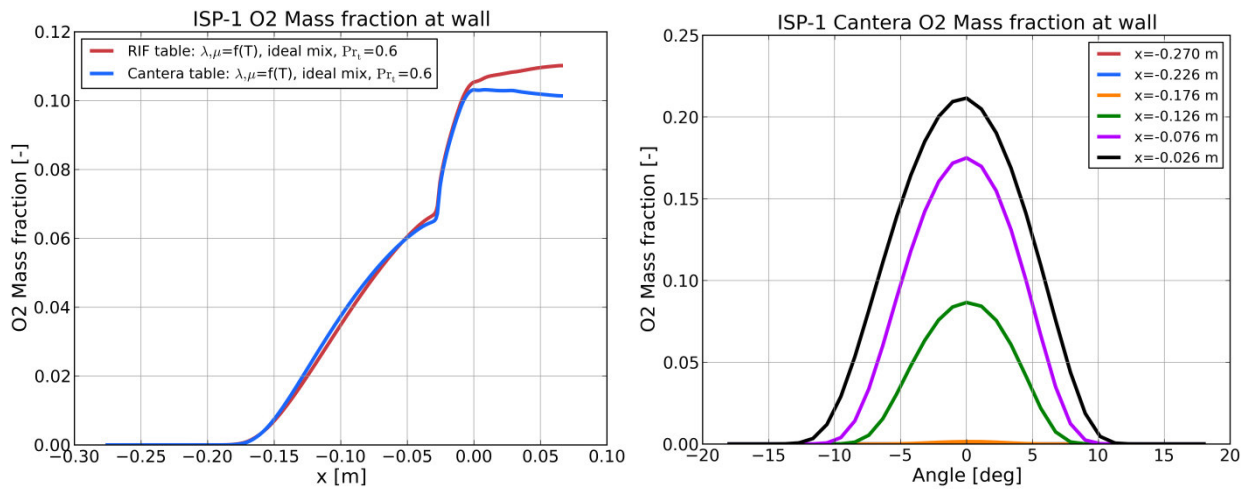
Figure 5.16: O$_2$ mass fraction at the wall along the chamber axis (left) and the azimuthal direction (right) for the ISP-1 combustion chamber.

Apart from the heat flux, a comparison was carried out for the temperature field, OH mass fraction and scalar dissipation field within the thrust chamber. The maximal occurring values for these variables within the ISP-1 chamber, are listed in Table 5.5. (From this point on, the notation "RIF results" and "Cantera results" will be used for the ISP-1 test case, which implies same settings for both simulations: $\lambda, \mu = f(T)$, ideal mix, $Pr_t = 0.6$).

The temperature distribution at the chosen planes as well as in the nozzle segment are plotted in Figure 5.17 for both simulations.

87
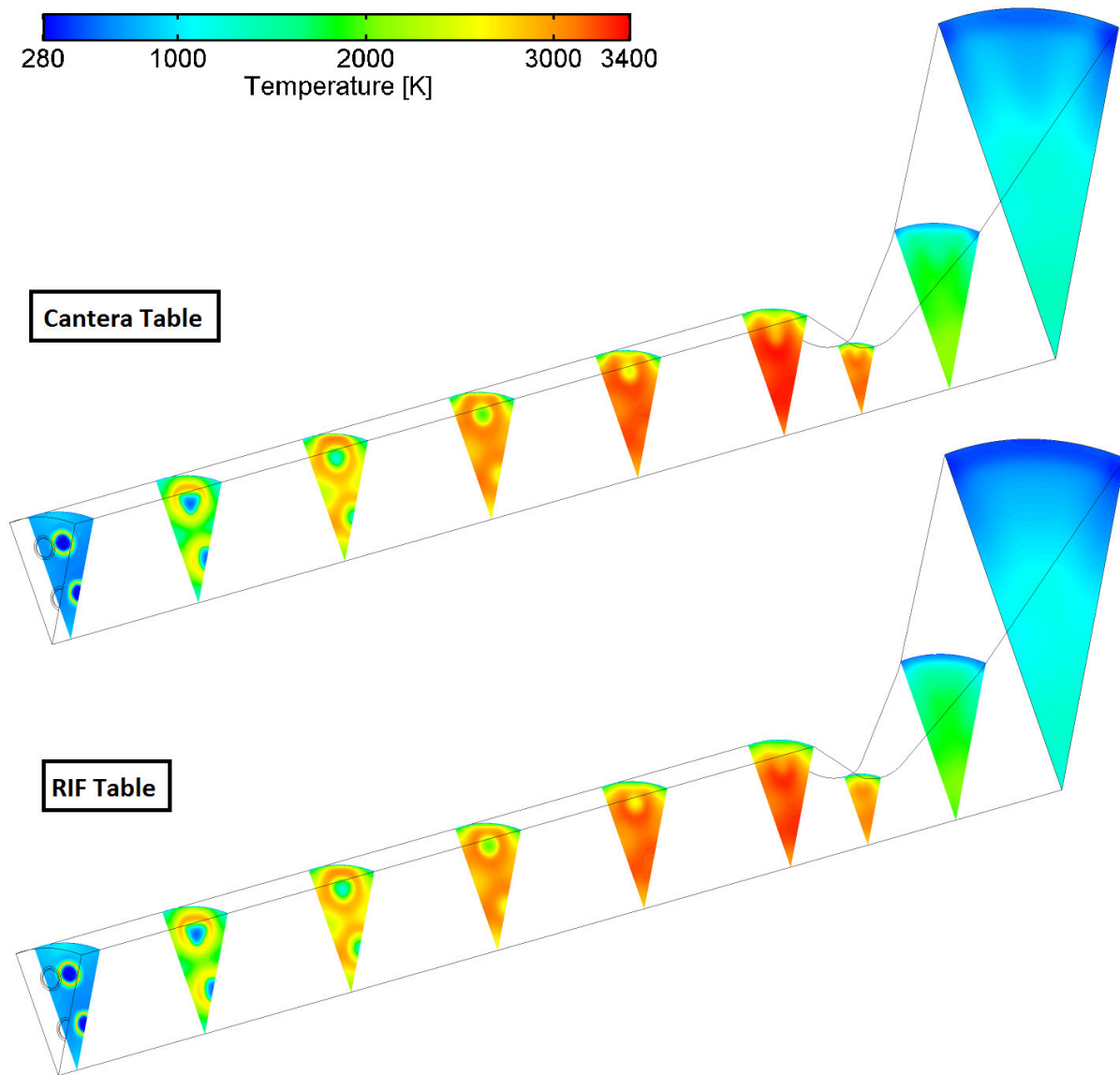
Figure 5.17: Temperature distribution on selected planes of the ISP-1 thrust chamber for the Cantera (up) and RIF (down) Flamelet results.

Table 5.5: Maximal occurring temperature, OH mass fraction and scalar dissipation rate in the ISP-1 test case for the RIF and Cantera tables.

	Max. T	Max. Y_{OH}	Max. χ
RIF results	3285.51 K	0.0748	28798.7 s^{-1}
Cantera results	3328.41 K	0.0740	27849.4 s^{-1}
Difference	1.306 %	1.069 %	3.409 %

It is evident, that the differences between RIF and Cantera results remain below 2% in the case of the maximal flame temperature and OH mass fraction and only exceeds 3% for the scalar dissipation rate. The similarity in the results is also illustrated in the contour plots of the temperature field (Figure 5.18 and Figure 5.19) and the OH mass fraction (Figure 5.20).

Apart from the slightly higher value for the maximal temperature in the chamber, the two tables demonstrate almost identical results for the temperature. In the case of the OH field, a small difference can be observed close to the injector located at the 0° plane. OH is an indicator for the flame and hence starts developing at the interface between O_2 and CH_4, i.e. in annular form around the main O_2 stream. For locations further downstream, the OH is no longer concentrated only on this annulus but rather diffuses into other regions as well. It can be seen in Figure 5.20, that in the case of Cantera, the point where the two sides of the annulus (projected on this 2D plane) attach is closer to the injector than for the RIF results. This implies a higher mass transport for the OH molecule in the case of the Cantera case.
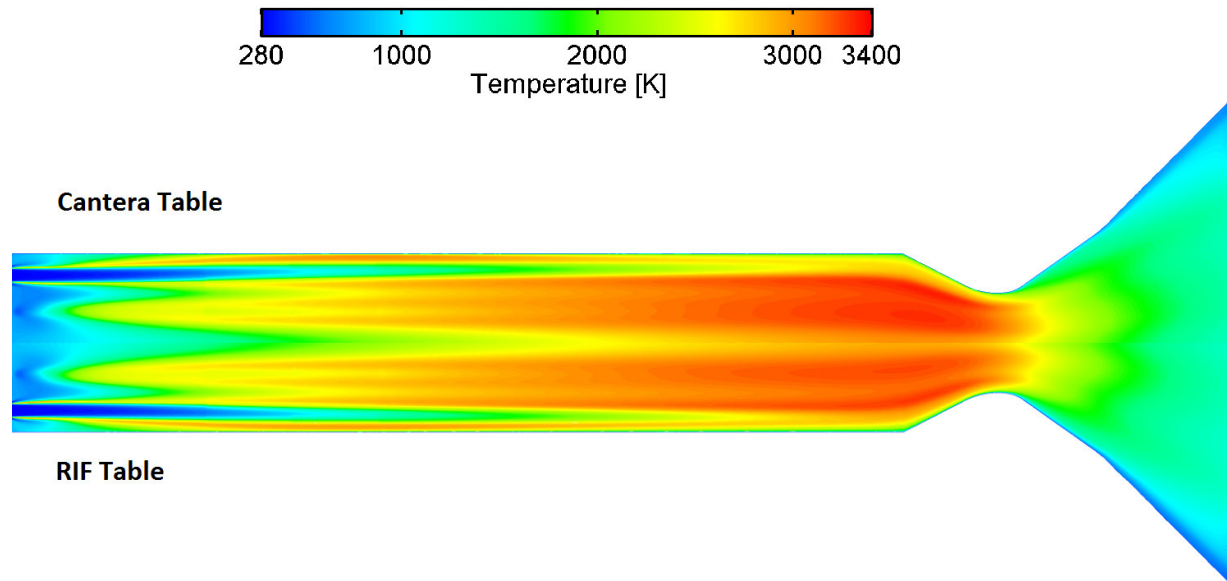
Figure 5.18: Temperature field at the 0° plane of the ISP-1 thrust chamber. Comparison between Cantera results (up) and RIF results (down).
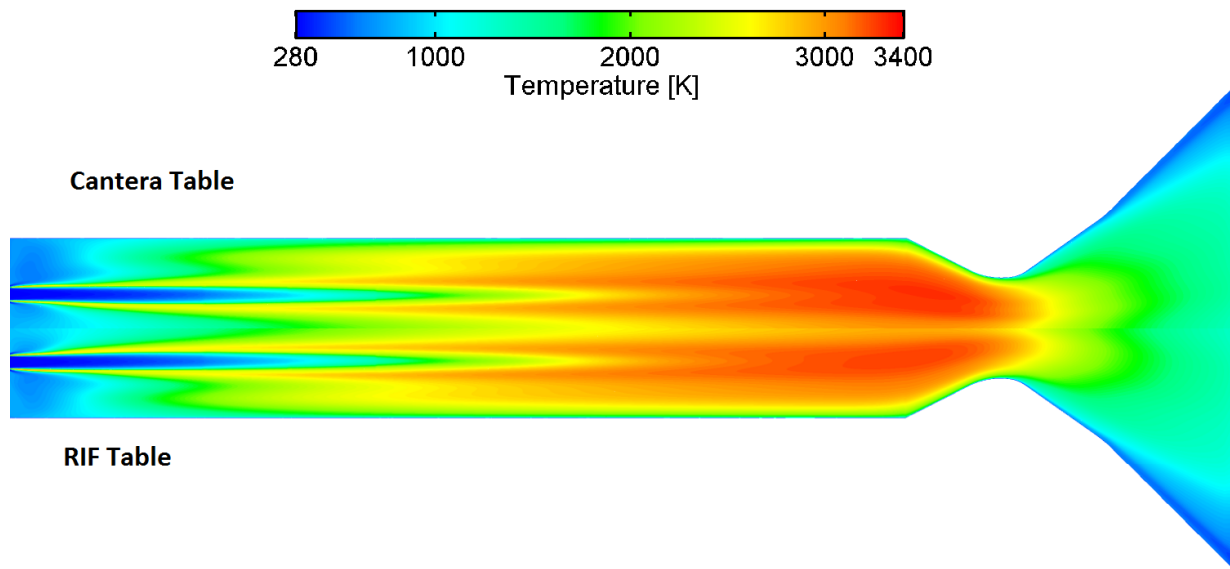
Figure 5.19: Temperature field at the -18° plane of the ISP-1 thrust chamber. Comparison between Cantera results (up) and RIF results (down).
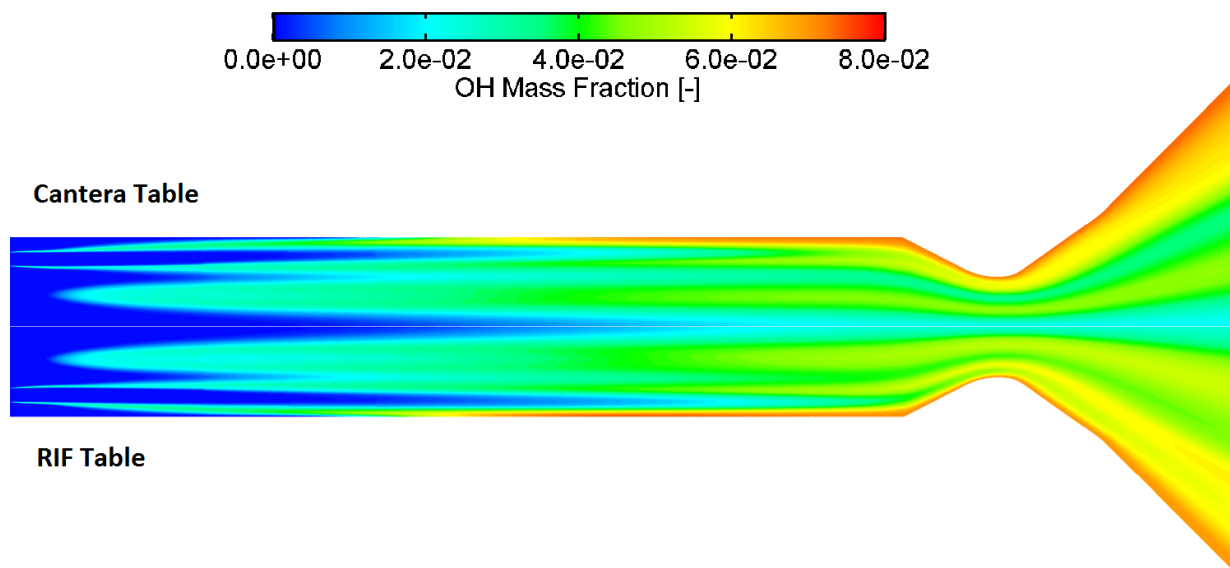
Figure 5.20: OH mass fraction field at the 0° plane of the ISP-1 thrust chamber. Comparison between Cantera results (up) and RIF results (down).

Another quantity which is significant when using the Flamelet tables, is the scalar dissipation rate. Its field on the wall of the chamber is shown in Figure 5.21. The profiles of Cantera and RIF display an identical profile and hence only the Cantera results are illustrated. The scalar dissipation rate increases right after the faceplate, then drops again and remains almost constant for the rest of the combustion chamber, before reaching a maximum again in the vicinity of the nozzle throat.
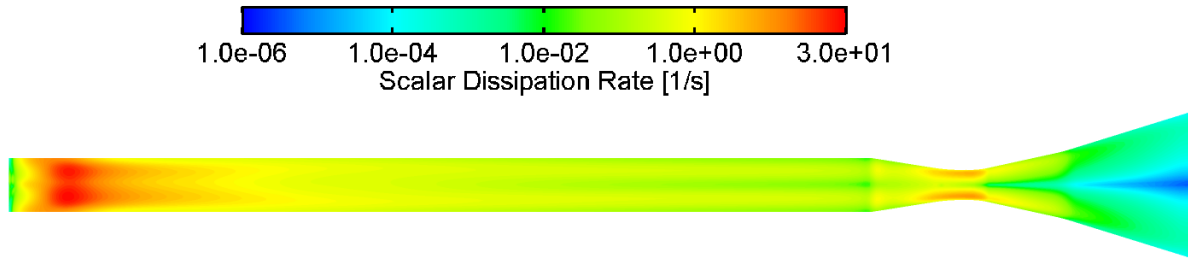
Figure 5.21: Scalar dissipation rate on the hot gas wall of the ISP-1 thrust chamber. Comparison between Cantera results (up) and RIF results (down).

The local maximum of the scalar dissipation rate close to the injector, appears at the same location as the maximum of the wall heat flux, as seen in Figure 5.9: Comparison of heat flux profile using the RIF and the Cantera Flamelet tables for the ISP-1 chamber.. In order to examine the cause of this maximum, the streamlines of the flow were plotted, along the 2D plane at 0°. It was found, that the aforementioned location corresponds to a stagnation point of the flow. This is because of the radial impulse of the coaxial injector, which pushes part of the propellant outwards, until it collides with the wall. This increases turbulence and therefore the heat exchange with the wall, as well as the scalar dissipation rate, since the latter one is calculated according to Eq. (2.64).
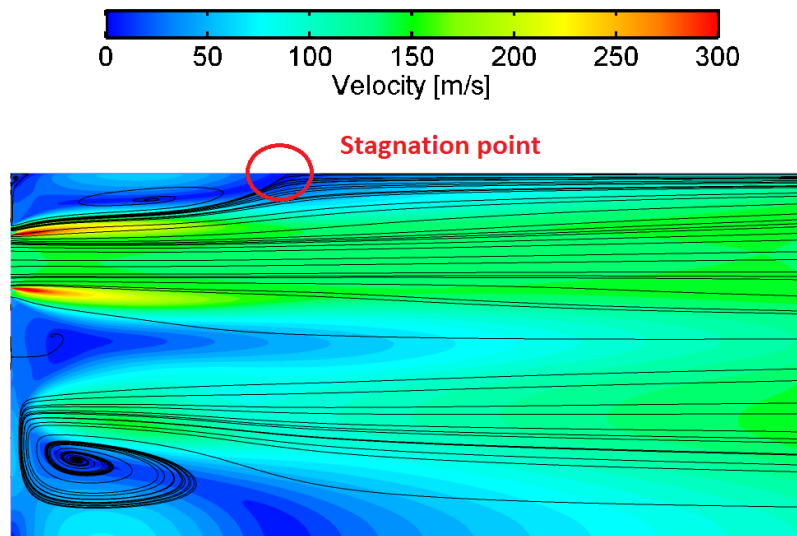
Figure 5.22: Stagnation streamline in the ISP-1 chamber.

Apart from the heat flux measurements, a further set of experimental data that can be used for the validation of the simulation comes from the pressure sensors. In total, four pressure sensors are installed within the combustion chamber, each one located at the middle axial position of the corresponding chamber segment. No data for the fifth chamber segment exists in the report by Suslov [59]. Furthermore, a pressure sensor is placed at the nozzle's throat. The pressure within the chamber drops from 10.180 bar in the first segment down to

10.136 bar in the fourth segment, which corresponds to a 0.42% decrease. The average value of all the tests with the same load point is used here, which have very consistent data, with the statistical deviation remaining underneath 0.02 bar.

A comparison between these experimental values and the CFX results is given in Figure 5.23. The error bars have been omitted since they are below 0.2% of the mean value. The CFX results, both with the RIF and with the Cantera tables, underestimate the pressure in the chamber. A combination of the Cantera table and a turbulent Prandtl number equal to 0.6, demonstrates the best agreement with the pressure data. It predicts a drop of 1.9%, with a pressure of 10.12 bar and 9.92 bar at the first and fourth segments respectively.

All four cases plotted in Figure 5.23 show very good agreement with the pressure measurement at the nozzle, which is equal to 5.71 bar.
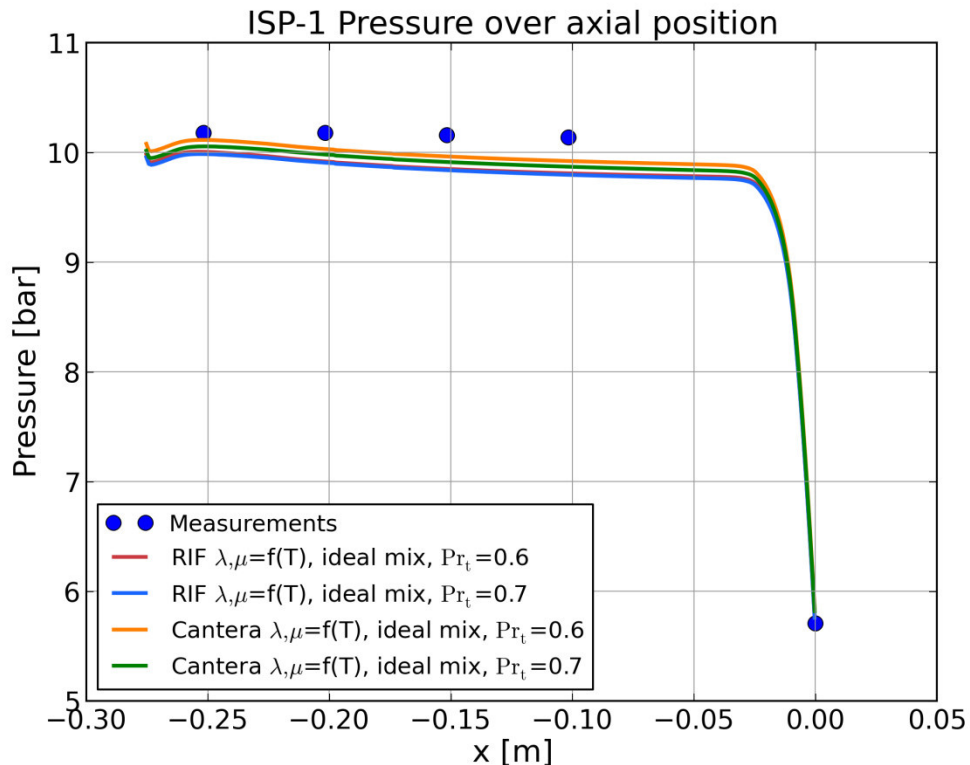
Figure 5.23: Pressure profile in the ISP-1 combustion chamber.

The slightly lower pressure (compared to the experimental values) has an effect on the efficiency of the ISP-1 chamber as well. The efficiency of the characteristic velocity was examined for the Cantera and RIF simulations according to the process described in Appendix F. The results are summarized in Table 5.6 and it is evident that that the calculated efficiency is much lower than typical values in aerospace applications (93%-

99%). Since no experimental values for the value of are available for the ISP-1 case, it could not be determined whether this low value was an artefact of the CFD simulation or if it represented the reality.

Table 5.6: Calculated combustion efficiency for the ISP-1 test case.

	η_{c^*} [%]	η_{c^*} with enthalpy correction [%]
RIF results	88.91	90.22
Cantera results	89.48	90.78

To sum up, the results obtained with the Cantera-generated Flamelet libraries were able to capture the heat flux and pressure profiles of the ISP-1 test case similarly to the respective RIF ones. The slight differences observed between the two methods are attributed mainly to the different species being modeled and the different reaction mechanism. It is hence evident, that Cantera could effectively substitute the RIF table generation process and was hence used for the simulation of the Romeo test case as well.

5.2 Romeo subscale case

The LOX/Methane propellant combination is a strong candidate for future low cost expendable and reusable launch vehicles. For that reason, Airbus Defence and Space is also currently investing in several liquid rocket propulsion demonstrator models in order to obtain experience, increase the Technology Readiness Level (TRL) of the specific technology and assess this propellant for future space transportation applications. Within this framework, subscale element tests have been carried out in order to demonstrate the performance and structural soundness and to verify the design baseline for the future full-scale hardware [7].

In 2007 the first LOX/GCH$_4$ sub-scale thrust chamber tests were performed by Airbus Defence and Space (at the time Astrium-ST) at the P8 test bench in Lampoldshausen. The key objectives were to establish a solid data base for wall heat flux evaluation and combustion characteristics under representative full-scale operational conditions [62].

5.2.1 Test case

Within the frame of the present work, a subscale rocket engine (Romeo engine), developed by Airbus Defence and Space was simulated. The hardware configuration consists of a calorimeter combustion chamber, comprising twenty individually water-cooled segments along the chamber axis and the nozzle.

The chamber has a diameter equal to 80 mm and a characteristic length of 0.84 m. The contraction and expansion ratios are 2.5 and 5 respectively. The injector head includes 19 coaxial injector elements, 18 of which are distributed on two concentric circles and one of them located on the center axis. Liquid oxygen and gaseous methane are injected into the chamber through the injectors. The chamber pressure is set at 40 bar, leading to subcritical conditions for the oxygen (critical pressure 50.4 bar [8]), which is at 100 K during injection. Methane on the other hand is injected at 280 K in gaseous form. The O/F for the simulated test case was set to be fuel-rich, at 3.4.

5.2.2 CFX setup

The computational domain in ANSYS CFX was defined as a 30° segment able to capture the symmetry properties of the chamber and the injector. The mesh was taken from the work performed by Riedmann et al. [61] and consists of 3.5 million cells.

The boundary conditions were very similar to the ones described in the ISP-1 test case (Section 5.1.2), with two mass flow inlets, a pressure outlet at the exit, adiabatic faceplate wall and symmetry planes at -15° and 15°. The hot gas chamber wall was given a

temperature profile along the axis. Its roughness was also defined as a function of the axial distance, as measured during the test campaign at the P8 test bench.

For the combustion simulation, the Flamelet model with the CFX RIF and Cantera tables was once again used. The transport properties of the individual species were defined to be temperature dependent, since it was found from the ISP-1 results, that this formulation captures the physical processes in the chamber more realistically.

The main difference compared to the GOX/GCH4 ISP-1 case, is the presence of LOX in the injector of the Romeo engine. Due to the conditions being subcritical, the oxygen changes phase within the chamber (evaporation from liquid to gaseous form). For that reason, the two models described in Section 2.2.4 were implemented and compared to each other. For the Real Gas Properties, a table with data from the GASPAK database [63] was imported, covering a temperature range from 60 K to 5000 K and pressures from 0.03 bar to 250 bar.
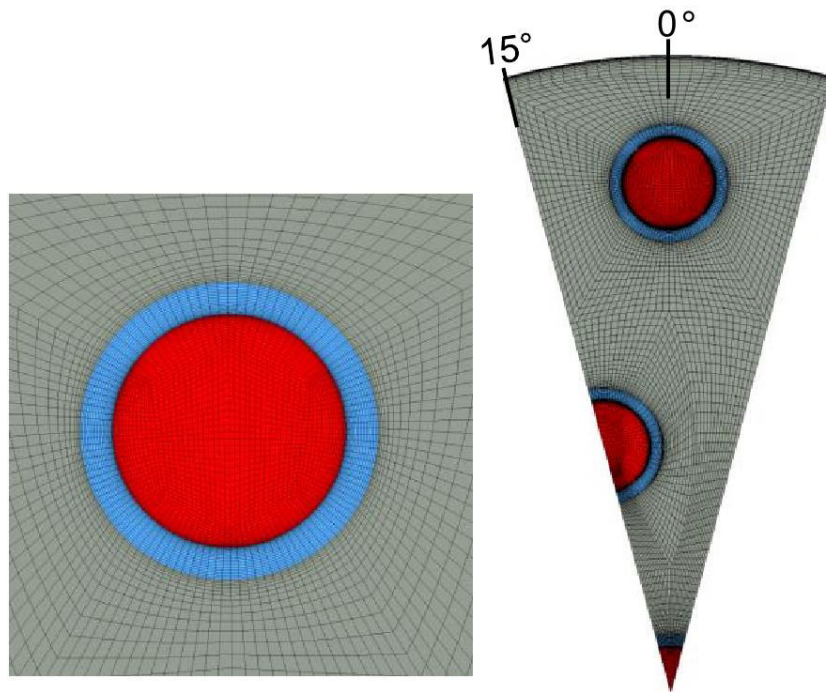
Figure 5.24: Injection element meshing for the CFX simulation of the Romeo subscale test case from Riedmann et al. [61] (red: oxygen inlet, blue: methane inlet, grey: adiabatic wall).

5.2.3 Results

For the first approach of the Romeo test case, the two models for the description of LOX were examined. For that reason three separate setups were implemented:

- Constant properties liquid with the RIF Flamelet table
- Constant properties liquid with the Cantera Flamelet table
- RGP model with the Cantera Flamelet table

For a more effective comparison, all remaining settings were kept identical and the turbulent Prandtl number was defined equal to 0.6.

The first comparison carried out included the density field within the chamber. The results for the two models (RGP and constant properties liquid) in the case of the Cantera table are given in Figure 5.25. It is evident, that the two methods predict a similar length of the "cold" liquid O_2 jet which implies that the assumptions met in the "constant properties liquid" model can sufficiently be used in the case of subcritical LOX.
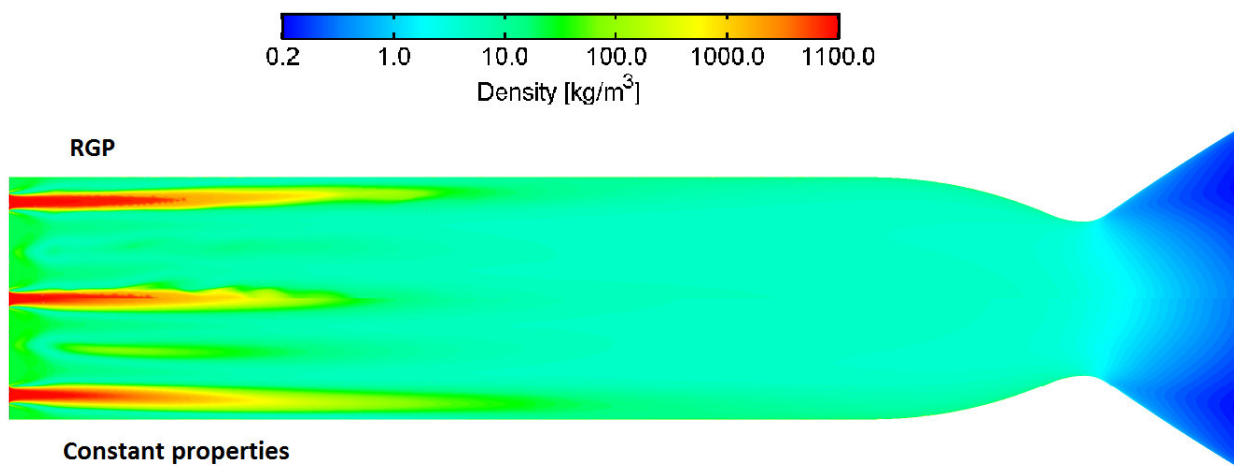
Figure 5.25: Density field in the Romeo subscale chamber for the RGP (up) and "constant properties liquid" (down) models using the Cantera table.

The results for the heat flux (normalized with the average experimental value at the nozzle throat) are presented in Figure 5.26 and Figure 5.27. All three setups manage to produce heat flux profiles that capture the trend of the experimental data. Not only in the combustion chamber but also within the nozzle, the simulation results predict heat flux values similar to the measured ones. Also at the location of the throat, where the highest heat flux appears, the simulation captures the correct value within the experimental statistical variation. A larger discrepancy occurs only in the divergent part of the nozzle. In this segment, the predicted heat flux by the simulations remains significantly lower than the experimental values (error close to 38%).
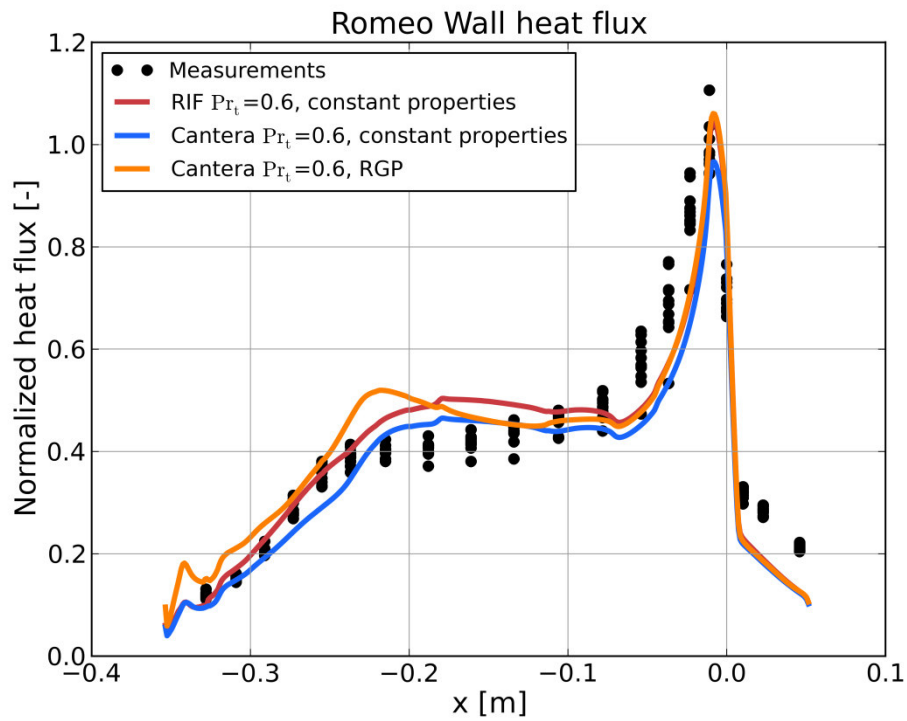
Figure 5.26: Wall heat flux results for the Romeo subscale test case.
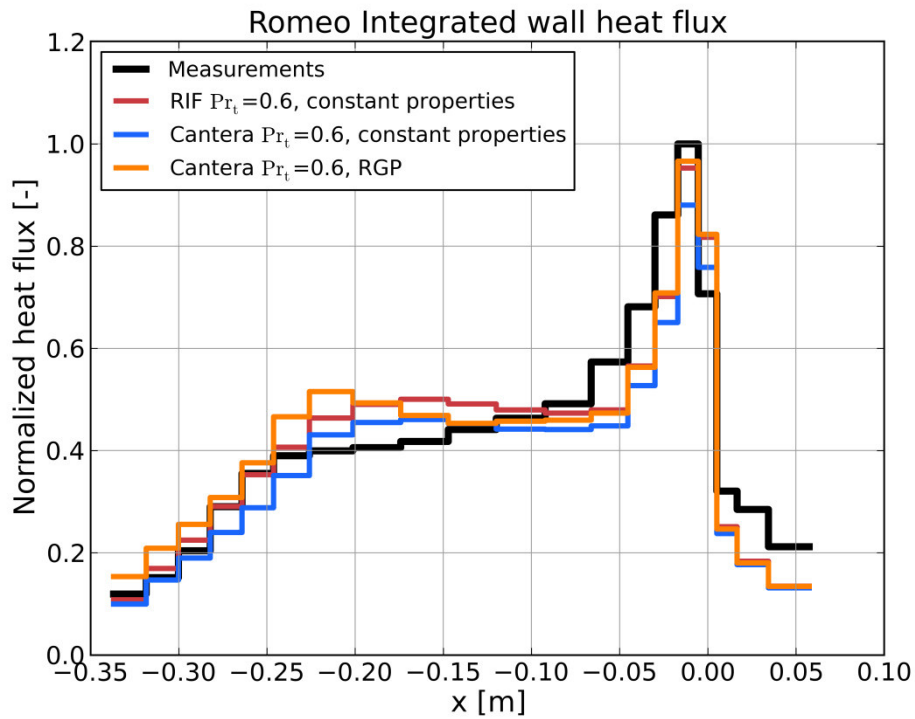
Figure 5.27: Integrated wall heat flux results for the Romeo subscale test case.

Just like in the case of the ISP-1 simulation, the main difference between the RIF (red line) and the Cantera table (blue line) for the constant properties liquid model, lies in the magnitude of the heat flux. The RIF results demonstrate slightly higher heat flux values, which can be attributed to the larger H_2O and lower CO concentration as elaborated in Section 5.1.3.

The RGP method also meets the heat flux measurements in the first part of the combustion chamber and in the nozzle. Especially at the throat location, it produces a value very close to the average experimental one. However, it is observed that in the vicinity of the combustion chamber's middle point, it leads to an overestimation of the heat transfer which creates a local maximum. The nature of this local abnormality was identified by examining the profiles of the thermal conductivity, and temperature at the chamber wall, as illustrated in Figure 5.28. Close to the local maximum of the heat flux (x=-0.22 m), the temperature in the RGP simulation is higher. This fact, in combination with the local maximum observed in the thermal conductivity at the same location (left subfigure in Figure 5.28) is pinpointed as the source of the higher heat flux. It is interesting, that the RGP results showcase a drop in the thermal conductivity in the middle of the chamber (x=-0.15 m) which is not present in the case of the "constant properties liquid". As Figure 5.29 indicates, this observed effect can be attributed to the higher O_2 concentration at the wall, which effectively reduces the thermal conductivity. The presence of more O_2 in the wall is a result of the different thermodynamic and transport properties stemming from the RGP table.
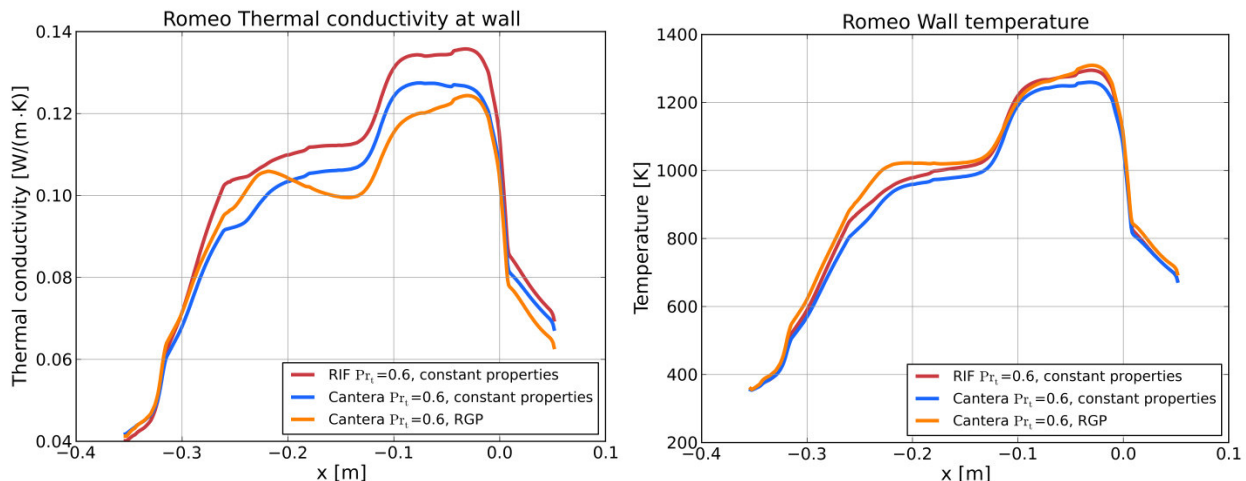
Figure 5.28: Thermal conductivity (left) and temperature (right) profiles at the chamber wall of the Romeo subscale test case.
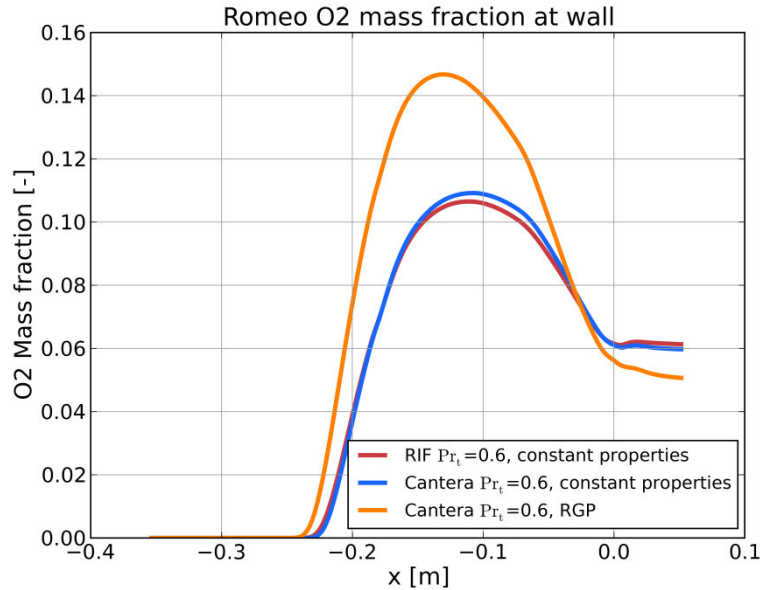
Figure 5.29: O₂ mass fraction at the chamber wall of the Romeo subscale test case.

Some representative values of the Romeo simulations are summarized in Table 5.7. The error metric J shows that all three setups lead to a similar deviation from the experimental results, with the "constant properties liquid" method combined with the RIF table providing the best agreement. Similar results are also observed regarding the maximal temperature. The main issue connected to the results lies in the obtained values for the combustion efficiency and the chamber pressure. Specifically, the "constant properties liquid" model predicts an efficiency lower than 88%, whereas the efficiency in the RGP model lies at 91%[13]. The lower combustion efficiency is directly connected to the values of p_c. An underestimation of the pressure by up to 9.5% (4 bar in the case of the constant properties liquid) is detected. For comparison, the average experimental combustion efficiency is reported at approximately 98%.

Table 5.7: Summary of simulation results of the Romeo subscale test case.

Settings	J [MW/m²]	J_{rel} [%]	η_{c^*} [%]	T_{max} [K]	p_c [bar]
Measurements	0.00	0.00	98.00	-	42.30
RIF table, $Pr_t = 0.6$, const. prop.	3.05	17.04	87.63	3425	38.30
Cantera table, $Pr_t = 0.6$, const. prop.	3.56	18.53	87.98	3443	38.49
Cantera table, $Pr_t = 0.6$, RGP	3.30	21.56	91.00	3481	39.78

---

[13] The efficiency of the characteristic velocity with the enthalpy correction is examined throughout this section, since it is more representative than the adiabatic value. Its calculation is described in Appendix F.

To examine the nature of the lower efficiency, the results of the "constant properties liquid" model were further investigated. The first intriguing property observed was the amount of unburnt oxygen remaining at the exit of the nozzle. This is visible in Figure 5.30, where the respective profiles of the average O_2 and CH_4 mass fractions are plotted as a function of the axial position. Both the RIF and Cantera results show that approximately 8% O_2 is remnant at the nozzle outlet, although the load point is at a fuel-rich propellant ratio, with $O/F = 3.4$.
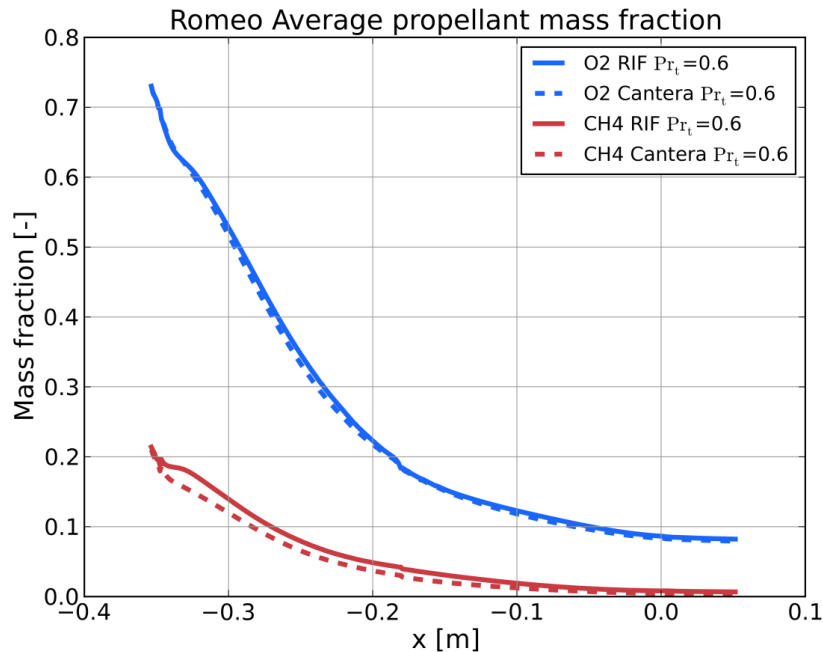
Figure 5.30: Average O_2 and CH_4 mass fraction in the Romeo subscale thrust chamber.

The potential confusion of this result is cleared when examining the theoretical equilibrium solution in the case of CH_4/O_2 combustion. As explained in Chapter 4 and again shown in Figure 5.31, no CH_4 is present in the equilibrium solution for some O/F values, even at fuel-rich conditions. Although the stoichiometric O/F is at approximately 4.0, already at $O/F \approx$ 1.3 the CH4 is depleted. For higher O/F, neither CH_4 nor O_2 is present and for values upwards of $O/F \approx 2.8$ (still fuel-rich), only O_2 prevails in the equilibrium solution. This comes in contradiction to the H_2/O_2 case, where CH4 is always present in non-zero concentration at fuel-rich conditions (right subfigure in Figure 5.31). This difference in the chemistry of the two propellant combinations is attributed to the decomposition of CH_4 even in the absence of O_2, which leads to its depletion even when the mixture is fuel-rich. Hence, in the Romeo case ($O/F = 3.4$), the equilibrium solution predicts that approximately 4.35% O_2 and 0% CH_4 remain.
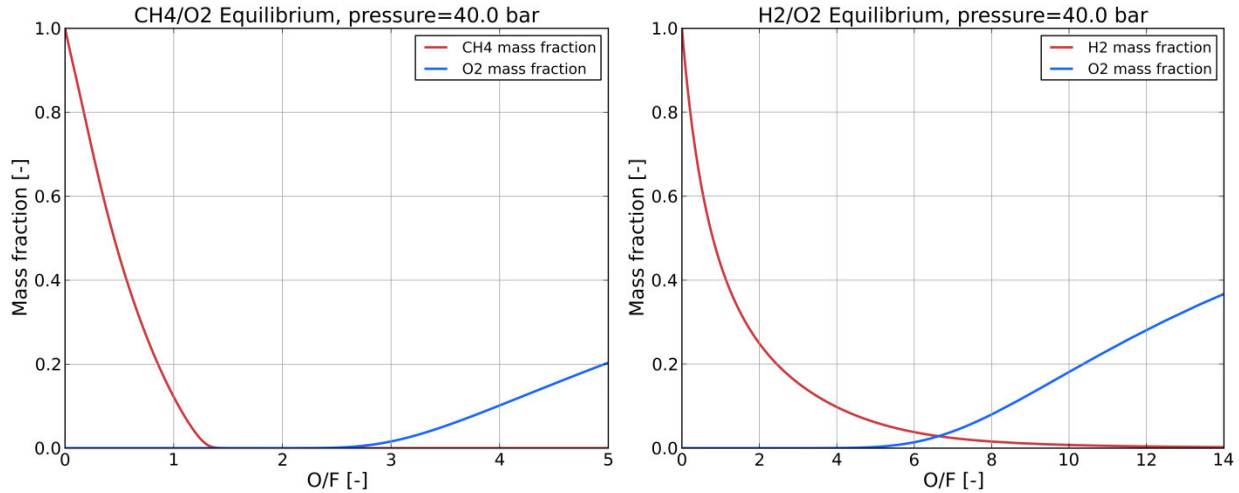
Figure 5.31: CH_4/O_2 (left) and H_2/O_2 (right) theoretical equilibrium solutions as a function of the O/F.

Of course, within the thrust chamber, the effect of turbulence and non-infinite fast chemistry results in a departure from equilibrium. Still however, the presence of 8% O_2 is considered to be excessive and was attributed to a poor mixing within the chamber. In order to improve the mixing within the thrust chamber, following measures were taken:

- Increase of the turbulent intensity at the propellant inlets from 10% to 20%.
- Decrease of the turbulent Prandtl and Schmidt numbers from 0.6 to 0.5.

In the first case it is expected that the increased degree of turbulence near the inlet will lead to a more thorough mixing of the oxidizer and inlet and hence result to a higher pressure and efficiency and a lower O_2 concentration at the exit. The second case is based on the fact that a lower Schmidt number directly translates to a higher value for the turbulent diffusivity which in turn is expected to raise the degree of mixing. A significant disadvantage of CFX when undertaking the change of Sc_t is the fact that the turbulent Prandtl number is altered as well at the same time, due to the constraint $Le_t = 1$.

As predicted, both measures seem to increase the mixing within the chamber and consequently improve the efficiency of the characteristic velocity. At the same time, the remaining O_2 and CH_4 at the outlet seem to reduce. Unfortunately, the decrease of the turbulent Schmidt number leads to a larger departure of the simulated heat flux from the experimental measurements. The two effects are summarized in Table 5.8. It is however evident, that a further decrease of the Prandtl/Schmidt number does not lead to an additional improvement of the efficiency and the pressure. The efficiency seems to reach a plateau close to $Pr_t = 0.3$ as well as the pressure at the throat, which barely exceeds 40 bar. At the same time, the oxygen mass fraction at the nozzle exit reaches the theoretical equilibrium solution of approximately 4%.

Table 5.8: Summary of simulation results in the parametric improvement of the mixing in the Romeo subscale test case.

Simulation settings	J [MW/m^2]	J_{rel} [%]	η_{c^*} [%]	p_c [bar]	O$_2$ at exit [%]	CH$_4$ at exit [%]
Measurements	0.00	0.00	98.00	41.80	-	-
RIF, $Pr_t = 0.6$	3.05	17.04	87.63	38.30	8.22	0.68
Cantera, $Pr_t = 0.6$	3.56	18.53	87.98	38.49	7.93	0.34
Cantera, $Pr_t = 0.6$, 20% intensity	3.98	27.22	90.21	39.24	6.02	0.07
Cantera, $Pr_t = 0.5$	3.35	27.49	90.12	39.41	6.09	0.06
Cantera, $Pr_t = 0.4$	8.06	54.74	91.77	39.97	4.87	$1.6 \cdot 10^{-3}$
Cantera, $Pr_t = 0.3$	14.05	100.00	92.33	40.07	4.22	$5.6 \cdot 10^{-8}$

The negative effect of these two measures is evident when examining the heat flux profiles in Figure 5.32 and Figure 5.33. An overestimation of the heat transfer to the wall is observed, mainly due to the larger turbulent conductivity in the case of lower Pr_t and Sc_t numbers. In the case of a higher turbulent intensity, the effect of higher heat flux is limited in the first part of the combustion chamber and is damped for positions further downstream. The heat flux results for are not shown, since they possess a much larger error, reaching up to 100% in some positions.
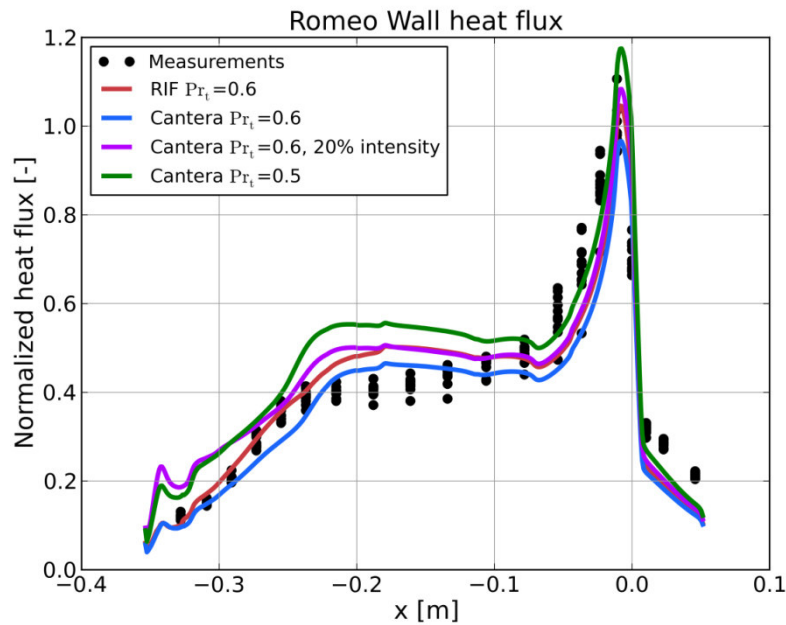
Figure 5.32: Heat flux profiles in the parametric improvement of the mixing in the Romeo subscale test case.
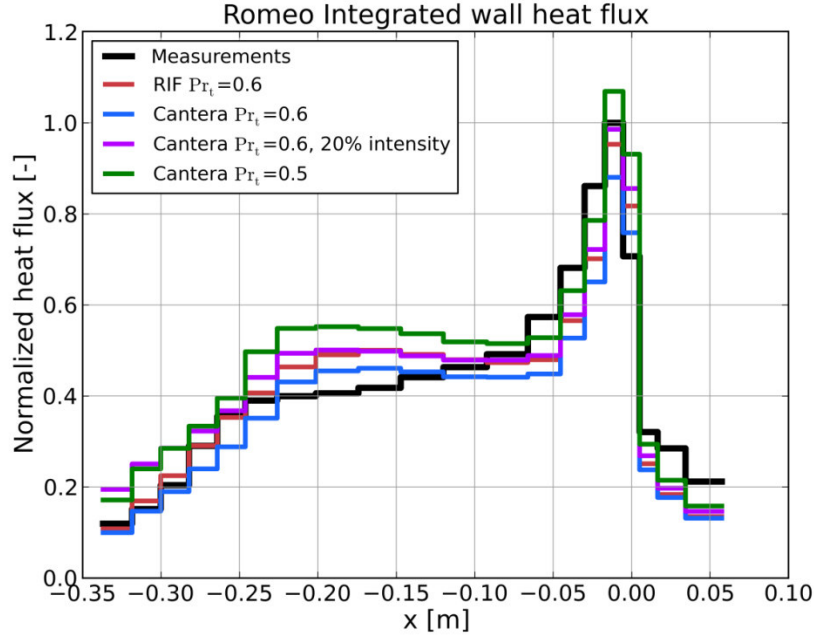
Figure 5.33: Integrated heat flux profiles in the parametric improvement of the mixing in the Romeo subscale test case.

A further indicator that the low combustion efficiency and incomplete combustion of the propellants in the chamber are triggered by the poor mixing occurs when examining the unmixedness of the hot gas. The unmixedness is a dimensionless number which describes the degree of mixing in the chamber. For an ideal mixture, it reaches the value 0, whereas for totally unmixed compounds, it is equal to 1. The umixedness is not a property of every point in the computational domain but is rather defined for a group of points, since it is a merit for the variation of the mixture ratio among those points. Assuming that the unmixedness U is examined for a group of N points located on a surface, then the following expression can be used for its calculation:

$$U = \frac{\langle Z''^2 \rangle}{\langle Z \rangle (1 - \langle Z \rangle)} \tag{5.5}$$

In Eq. (5.5), $\langle Z \rangle$ represents the average mixture fraction value and $\langle Z''^2 \rangle$ the variance of the mixture fraction on the surface.

$$\langle Z \rangle = \frac{1}{N} \sum_{i=1}^{N} Z_i \tag{5.6}$$

$$\langle Z''^2 \rangle = \frac{1}{N} \sum_{i=1}^{N} (\langle Z \rangle - Z_i)^2 \tag{5.7}$$

103

In the present thesis, the unmixedness was evaluated at planes normal to the axial coordinate, leading to a profile of U along the chamber axis. It is expected that the value of U close to the injector should be high, due to the lack of mixing. In the ideal case of perfect mixing (and hence high combustion efficiency), U should approach 0 close to the nozzle exit. Indeed, this is observed in the Romeo subscale simulation results as seen in Figure 5.34. A decrease of the turbulent Prandtl and Schmidt numbers causes an improved unmixedness in the chamber, serving as a proof that the mixing is indeed more efficient in those cases.
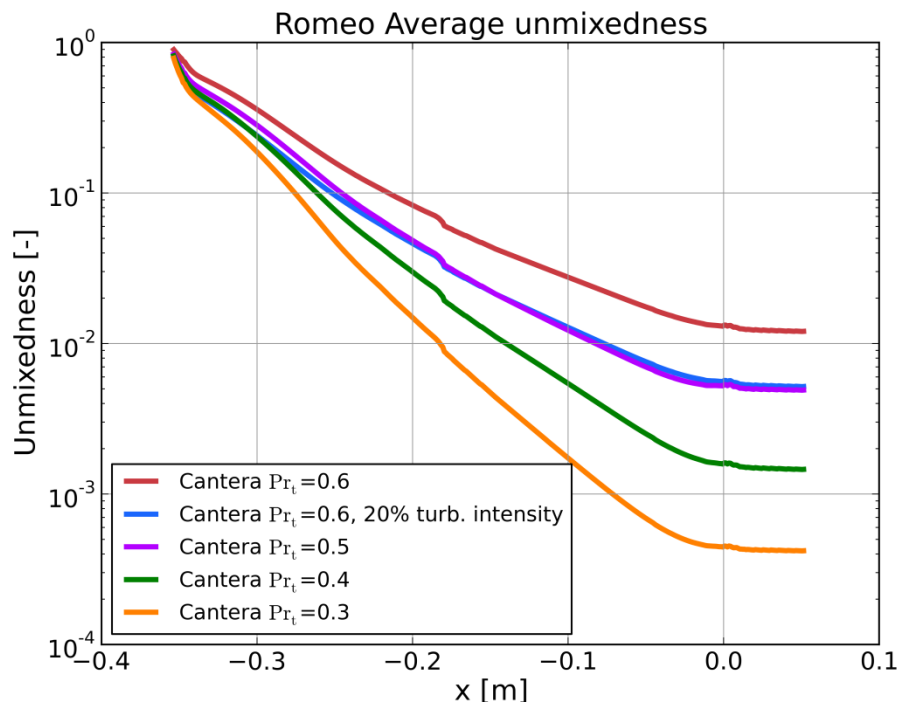
Figure 5.34: Unmixedness profiles within the Romeo thrust chamber.

Apart from modifying the turbulent intensity and the turbulent Prandtl and Schmidt numbers, another reaction mechanism was also examined. Specifically, the skeletal mechanism by Zhukov et al. [64] was implemented, which is suitable for high pressure methane combustion. With this new mechanism, a table was generated in Cantera and loaded into the CFX simulation. A slight increase of the combustion pressure and efficiency was indeed observed. The combination of the new reaction mechanism with the use of the RGP model provided with the best results even at a Prandtl number of 0.6. These are summarized in Table 5.9, along with the results using the GRI 3.0 mechanism, for direct comparison.

Table 5.9: Summary of simulation results using the reaction mechanism by Zhukov et al. [64] in the Romeo subscale test case.

Simulation settings	J [MW/m^2]	J_{rel} [%]	η_{c^*} [%]	p_c [bar]	O$_2$ at exit [%]	CH$_4$ at exit [%]
Measurements	0.00	0.00	98.00	41.80	-	-
GRI 3.0, constant properties	3.56	18.35	87.98	38.49	7.93	0.34
GRI 3.0, RGP	3.30	21.56	91.00	39.78	8.15	0.13
Zhukov, constant properties	3.08	17.06	89.15	38.98	6.96	0.13
Zhukov, RGP	3.85	31.51	91.86	40.12	7.20	0.03

An efficiency close to 92% is achieved with the RGP model and the skeletal mechanism of Zhukov. On the other hand, a larger deviance from the measurements is observed in Figure 5.35. An overestimation of the heat flux in the first part of the chamber takes place. This is attributed to the higher temperature values at the wall and the local maximum in the profile of the thermal conductivity, as shown in Figure 5.36.
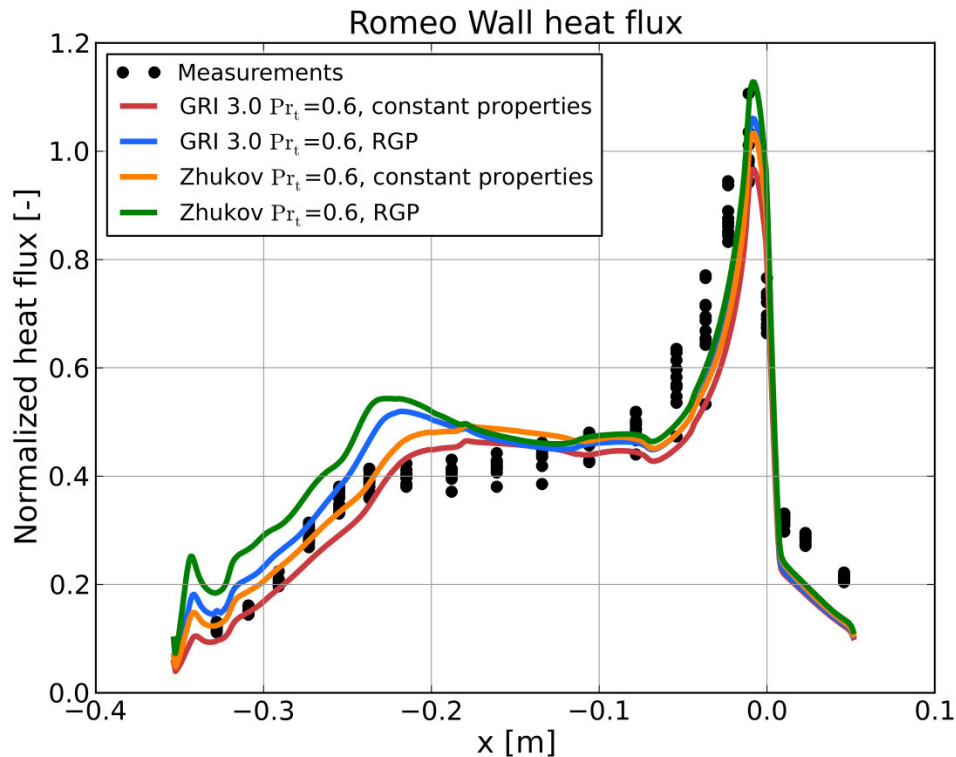
Figure 5.35: Heat flux results for the simulation of the Romeo test case with the skeletal mechanism by Zhukov et al. [64].
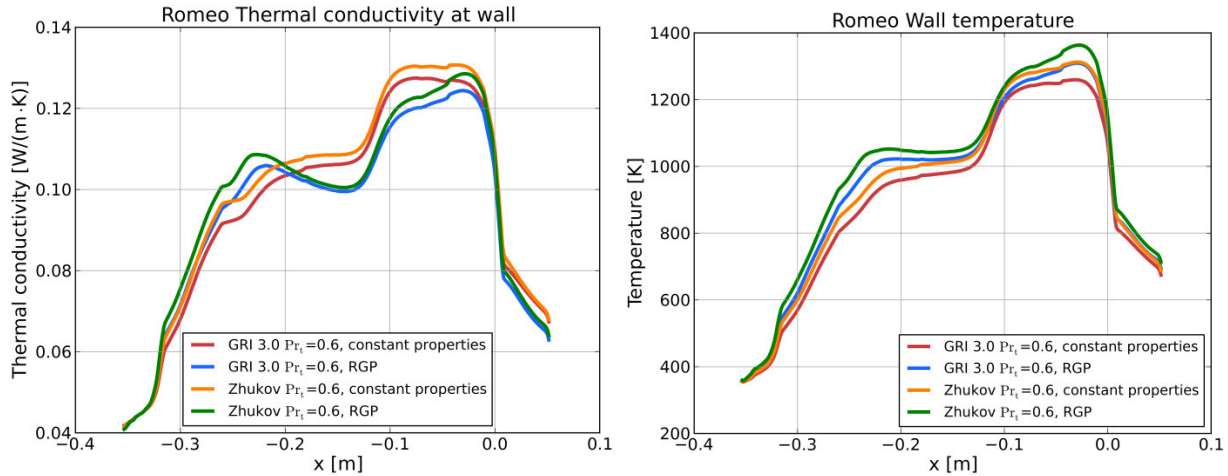
Figure 5.36: Thermal conductivity (left) and temperature (right) profiles at the wall of the Romeo chamber for the simulations using the skeletal mechanism by Zhukov et al. [64].

The overall superior performance of the RGP model in predicting the pressure and the combustion efficiency is also illustrated in Figure 5.37, where the static pressure profiles along the combustion chamber axis, as well as the unmixedness are plotted for the simulations with the GRI 3.0 and Zhukov mechanism.
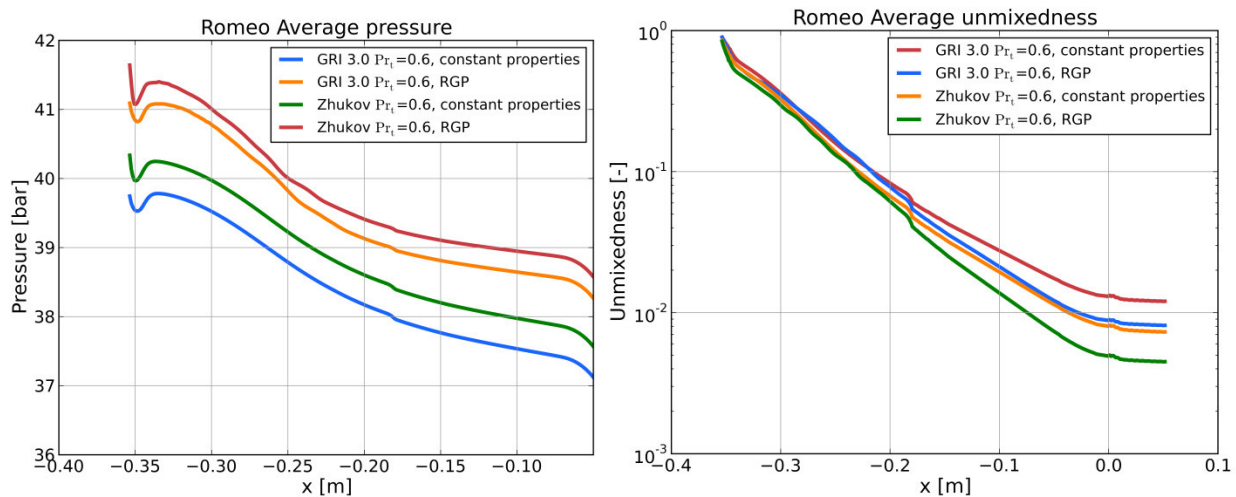
Figure 5.37: Average pressure (left) and unmixedness (right) profile along the Romeo thrust chamber for the simulations using the skeletal mechanism by Zhukov et al. [64].

Despite the efforts to increase the efficiency, values larger than 92% could not be obtained. Further ideas that were tested since they could potentially improve this effect include:

- The pressure level of the table generation: The Flamelet tables were generated at a pressure level of 40 bar. It was assumed that using a higher pressure level, could lead to a higher combustion pressure as well. This was examined, by generating a Flamelet table with Cantera at 45 bar, but did not deliver a significant improvement, since an efficiency of approximately 89% was achieved. In general, a pressure

dependent table would pose a more complete formulation of the Flamelet model. This would allow including pressure dependent effects, especially in the vicinity of the nozzle. It is further hypothesized that the large deviation of the heat flux results from the measurements in the divergent part of the nozzle, is connected to the pressure level of the Flamelet tables. The tables are created at 40 bar but the pressure in the nozzle drops as low as 1 bar.

- Further modeling of the heat capacity: In case the values used for the heat capacity of the major species were to contain errors, then they would propagate and lead to a wrong temperature and hence pressure of the gas in the thrust chamber. For that reason, the implemented NASA polynomials were cross checked with the values from NIST for the major species (O_2, CH_4, CO_2, CO, H_2O). No errors were detected and hence this topic was dismissed. However apart from the heat capacity of individual species, the mixing rules are also a topic requiring further modeling. It may be possible that the mass averaging rule for the heat capacity is no longer suitable for hydrocarbon chemistry.

Additional changes that could improve the results of CH_4/O_2 combustion simulations in rocket engine applications are mentioned in Chapter 6.

6 Conclusion and outlook

Acquiring a comprehensive understanding about methane/oxygen combustion is a necessary step for the implementation of this propellant in future launcher propulsion systems. For that reason, an effort to increase the accuracy of the mixture's combustion modeling was undertaken in this thesis. Being able to numerically simulate the physical and chemical phenomena within a CH_4/O_2 thrust chamber can lead to a more efficient design of potential thrusters.

Due to the complex reaction mechanism of hydrocarbons in general and consequently methane as well, finite rate chemistry modeling is usually either not efficient, when a large number of species is included, or not precise, in the case of a reduced mechanism. To overcome this issue, the Flamelet model was applied in this thesis, which overcomes the issue of additional transport equations for the species. This is achieved by calculating the mixture fraction, its variance and the scalar dissipation rate within the flow field and subsequently interpolating the tabulated values of the species' mass fractions as a function of those three flow quantities. Hence the turbulent combustion problem is reduced into a mixing problem and higher computational speeds are achieved. At the same time, including the scalar dissipation rate implies that non-equilibrium effects can be modeled in the simulation. This is essential for hydrocarbon combustion, where the chemical processes are not infinitely fast and hence the assumption of chemical equilibrium is not justified.

The main objective of the thesis was the development of a modular Flamelet table generator able to operate with the CH_4/O_2 propellant combination. This tool represents the preprocessing module of the combustion simulation, since it serves the purpose of "filling" the libraries which are later on loaded into the CFD simulation. The method applied for the table generation in this thesis was the solution of one-dimensional counterflow diffusion flames. This implies solving multiple instances of one-dimensional stagnation flows where the oxidizer and the fuel are injected from inlets placed opposite to each other and react. The resulting profile for the mixture fractions along the axis is then tabulated as a function of the mixture fraction, which is also a resulting variable in the 1D flow field. The Flamelet model assumes namely that the interaction zone of the propellants is much thinner than the scale of the smallest eddies, and hence it can be approximated by a 1D flow configuration. This is the reason, why the counterflow flame can be used for the generation of the tables.

To perform this preprocessing step, the open source chemistry tool "Cantera" was successfully utilized. Using the Python interface and based on an existing code developed for H_2/O_2 Flamelet tables, a flexible tool was programmed allowing the user full control over the applied settings. The reaction mechanism is one of the settings that can be modified in the

table generation process, but the GRI 3.0 mechanism was chosen as a standard. The code runs the counterflow diffusion flame problem for different values of the scalar dissipation. The scalar dissipation in not an input of the simulation but is rather calculated after the problem is solved, i.e. *a posteriori*.

The first step lies in generating the "laminar" table, where a tabulation of the mass fractions as a function of the mixture fraction and the scalar dissipation occurs. The range of the scalar dissipation values must be defined and is limited by the equilibrium value (lower limit) and the extinction value (upper limit): The tool was programmed in a way to gradually reduce the value of the scalar dissipation until it approaches zero. An exact value of zero represents equilibrium but cannot be achieved numerically. For that reason higher values close to $0.01 \ s^{-1}$ were defined as the target value. When this target "equilibrium" value is reached, the scalar dissipation is again increased until reaching a point of flame extinction. This quenching limit represents the point where the diffusion of heat due to the strain rate becomes so high, that a flame cannot be sustained. Having defined the upper limit for the dissipation, 60 values are chosen between the equilibrium value and the quenching value and the counterflow diffusion flame is solved for those points.

In order to introduce the effect of turbulence in the table, the mixture fraction variance was introduced. The process of extending the laminar table by one extra dimension was done by means of PPDF integration. For this integration, a Python module was programmed, able to describe β-PDF and Gauss PDF alike. This integration leads to the final Flamelet library, in a format compatible with the commercial CFD solver ANSYS CFX.

The differences between the Python/Cantera tool and other commercial Flamelet generators were identified. The main discrepancy lies in the set of equations that each generator solves. In the tool developed in the present thesis, solves the counterflow flame equations, which are a 1D, axisymmetric formulation of the laminar Navier Stokes Equations. In the case of other commercial tools (like CFX-RIF), the "Flamelet equations" are solved, in which the flow is solved not in physical coordinates (as in Cantera) but in the mixture fraction coordinates. This is advantageous since it does not require a subsequent transformation from the physical space to the mixture fraction as is done in the Cantera code. At the same time, in the "Flamelet equations", the scalar dissipation is indeed an input variable, defined *a priori*, in contrast to the Cantera tool, where it is calculated as a function of the flow variables *a posteriori*. A further restriction of Cantera is its inability to include inlet temperatures lower than 200 K. Despite those disadvantages, the Cantera tool has a much higher degree of flexibility, allowing the user to choose among different reaction mechanisms, modifying the mechanisms by excluding certain species, allowing a detailed description of the species' transport and thermodynamic properties. The tables obtained with the new tool were compared to the ones of CFX-RIF as well as with tables found in literature and demonstrated a sufficient agreement, hence leading to their verification.

Before applying the obtained libraries in a 3D CFD calculation of rocket engines, a more detailed look into the tabulated values was given. This helped to pinpoint some of the fundamental peculiarities of the methane/oxygen combustion, which could be relevant in rocket engine applications. Specifically, it was found that the dissociation of methane is so dominant, that even in fuel-rich configurations, all the methane is depleted and only oxygen remains after the end of combustion. This counter-intuitive property is not present in hydrogen/oxygen combustion, mainly due to the limited dissociation of hydrogen in the absence of oxygen. The second observation was that the mass fractions and temperature of the combustion products are highly dependent on the scalar dissipation rate. In the case of H_2/O_2 it was seen, that no significant effect in the composition occurs even for higher values of the scalar dissipation, which justifies why the equilibrium model is sufficient. For CH_4/O_2 on the other hand, the influence of the scalar dissipation (departure from equilibrium) is much higher, which is explained by the more complex reaction mechanism and the slower rates of the reactions.

The next step involved testing the Flamelet libraries in a CFD simulation of rocket engines. For that reason, the ISP-1 case, operated at 10 bar with GOX/GCH$_4$ at a fuel-rich O/F of 3.4 was examined. A comparison of the tables originating from Cantera and the ones of CFX-RIF was put on focus. Apart from the differences between the different tables, also the modeling of the transport properties was analyzed. It was found that a temperature depending description of the thermal conductivity and molecular viscosity of each chemical species is necessary to capture the heat flux profiles at the wall and is more physically intuitive than the temperature independent modeling. As far as the mixing rule for the transport quantities is concerned, it was established that the mass averaged mixing is sufficient and produces almost identical results with more complex rules like the Wilke and Brokaw, which are connected to much larger computational times.

Both the Cantera and the RIF tables were able to sufficiently capture the heat flux profiles at the wall of the calorimetric chamber. However, some slight differences were observed. The Cantera heat flux at the wall appeared to be slightly lower than the RIF one. This effect was further investigated on and it was found that the discrepancy is a result of the different CO and H_2O concentrations predicted by the two different tables. H_2O has a much larger thermal conductivity than CO and is more abundant in the boundary layer of the RIF tables, leading to the higher heat flux. This variation between the two tables was attributed to the different reaction mechanism as well as on the different means of table generation (counterflow flame versus Flamelet equations).

The second test case examined was the Romeo test, a subscale rocket engine developed at Airbus Defence and Space operating with subcritical LOX and GCH$_4$ at approximately 40 bar. Additional modeling effort was introduced with this test case, since it requires the description of the liquid oxygen. For this purpose two models were examined: the "constant

liquid properties" model, where all the properties of oxygen (density, heat capacity, thermal conductivity and molecular viscosity) are defined as constants and the "real gas properties" model, in which the thermodynamic and transport properties are tabulated as a function of temperature and pressure and called during the runtime. The second model is also able to include gaseous oxygen in the calculation but requires larger computational times. Having established the differences between Cantera and RIF tables, the focus was mainly placed on the Cantera tables created with the GRI 3.0 mechanism. Interestingly, both models managed to accurately predict the heat flux profiles at the wall but produced very low values for the combustion efficiency ranging from 88% (constant properties liquid) to 91% (real gas properties).

The cause of the low pressure and consequently low efficiency was identified as the poor mixing within the combustion chamber. It was namely found that a large amount of oxygen remained unburnt in the nozzle outlet, amounting to a mass fraction of approximately 8%. Operating at an O/F equal to 3.4, it was expected that some oxygen would be remnant at the exit but it was expected to be closer to 4%. For that reason, efforts to improve the degree of mixing were carried out, by increasing the turbulent intensity at the propellant inlets and decreasing the turbulent Schmidt number in order to induce a higher turbulent diffusivity. Both effects showed an improvement of the mixing and the combustion efficiency, which came with a compromise of the heat flux profiles at the wall. In the case of the higher turbulence at the inlet, an overestimation of the heat transfer close to the faceplate is observed, whereas in the case of a lower Schmidt number, the whole heat flux level is amplified. This occurs mainly due to a restriction imposed by CFX, according to which the Schmidt number is equal to the Prandtl number, and hence a decrease of its value leads to a higher turbulent conductivity as well. Despite additional efforts to further improve the combustion efficiency, including a different reaction mechanism in Cantera and a different pressure level at the table generation process, no significant effect was observed.

The low combustion pressure is an effect observed in hydrocarbon combustion not only when the Flamelet model is involved but also with finite rate and eddy dissipation models in other studies carried out within Airbus Defence and Space. There appears to be some physical or chemical effect which is not captured by the models currently available. In this context, some suggestions are made which could provide a solution to the problem.

- **Separate definition of the turbulent Prandtl and Schmidt numbers**. Unfortunately, the assumption of a unity turbulent Lewis number implemented in CFX, does not allow an independent definition of the Schmidt number. The very existence of this modeling parameter is one of the main disadvantages of the RANS model and the additional constraint imposed by CFX complicates the modeling even further. Having a low turbulent Schmidt number and a moderately high turbulent Prandtl number would lead to a higher diffusivity of the species (promoting better

mixing) without an additional increase in the heat flux. The standard parameters available in CFX do not enable this independent definition of the two numbers, so an editing via the Fortran interface is suggested.

- **Position dependent Prandtl and Schmidt numbers**. The definition of the two closure parameters of the RANS model as field-dependent quantities could provide an improvement in the case of CH4/O2 thrust chambers. It is namely a stretched assumption, that a constant value along the whole chamber describes the turbulent heat and mass transfer effectively. Different values may be suitable for different regions (close or further away from the wall, combustion chamber vs nozzle, etc.) for more accurate modeling. However, a physical process determining how the optimal profile of the two numbers in the chamber should look like is missing and should not be achieved via the trial and error approach. Either a scaling law for the turbulent numbers as a function of flow quantities or a further transport equation for them is required to introduce a scientifically accurate variable Prandtl and Schmidt number.

- **New mixing laws**. The mixing laws for the thermodynamic quantities (specifically the heat capacity) in CFX are based on a mass averaging. Although this provides satisfying results in the case of H_2/O_2 combustion, it could be insufficient in the case of CH_4/O_2. Assuming that the real heat capacity of the mixture is lower than what the mass averaging method predicts then the mass averaging method overpredicts the heat capacity leading to a lower temperature and pressure in the combustion chamber. A reason for that could be the mixing enthalpy, which is completely ignored in the case of an ideal mixing, but which could potentially have an influence on the final temperature of the mixture. This effect could be present in the case of hydrocarbon chemistry, where heavier molecules are present compared to the "simpler" H_2/O_2 mixture. Before searching for a more complex mixing law, this idea could be tested by intentionally decreasing the heat capacity of the reacting species and observing whether this artificial "mixing law" brings the desired effect.

- **Better resolution of the injector.** By resolving the post-tip of the coaxial injector, the interaction between the oxidizer and fuel jets can be simulated more realistically. In the present thesis, no cells are placed between the fuel and oxidizer inlets and hence their mixing occurs solely based on shear forces. In the case of additional cells, vortices can be modeled, which could under circumstances increase the degree of mixing in the vicinity of the faceplate and hence lead to a higher combustion pressure. Finally, the injector itself could be resolved, in order to include the effect of a fully developed flow. This could also be introduced by prescribing a parabolic profile in the inlet of the propellants.

To sum up, the Flamelet generator developed with Cantera was validated successfully for CH_4/O_2 combustion. The results obtained from the table generation gave important insights into the combustion properties of the mixture. Applying the tables in rocket engine applications lead to a satisfactory description of the chemical phenomena in the thrust

chamber and provided with good results for the wall heat flux. However, some open questions regarding the low combustion efficiency still remain and need to be further examined in order to fully understand the peculiarities of the CH_4/O_2 propellant combination.

Appendix A: GRI 3.0 reaction mechanism

The GRI 3.0 reaction mechanism was developed for the calculation of combustion processes involving methane or natural gas. It consists of 53 species and 325 elementary reactions. A detailed description of the mechanism is given in Smith et al. [23]. The species modeled are the following:

H_2, H, O, O2, OH, H_2O, HO_2, H_2O_2, C, CH, CH_2, $CH_2(S)$, CH_3, CH_4, CO, CO_2, HCO, CH_2O, CH_2OH, CH_3O, CH_3OH, C_2H, C_2H_2, C_2H_3, C_2H_4, C_2H_5, C_2H_6, HCCO, CH_2CO, HCCOH, N, NH, NH_2, NH_3, NNH, NO, NO_2, N_2O, HNO, CN, HCN, H_2CN, HCNN, HCNO, HOCN, HNCO, NCO, N_2, AR, C_3H_7, C_3H_8, CH_2CHO, CH_3CHO

The reactions included in the mechanism can be found underneath:

$2 O + M \iff O_2 + M$	$O_2 + CH_2O \iff HO_2 + HCO$
$O + H + M \iff OH + M$	$H + O_2 + M \iff HO_2 + M$
$O + H_2 \iff H + OH$	$H + 2 O_2 \iff HO_2 + O2$
$O + HO_2 \iff OH + O_2$	$H + O_2 + H_2O \iff HO_2 + H_2O$
$O + H_2O_2 \iff OH + HO_2$	$H + O_2 + N_2 \iff HO_2 + N_2$
$O + CH \iff H + CO$	$H + O_2 + AR \iff HO_2 + AR$
$O + CH_2 \iff H + HCO$	$H + O_2 \iff O + OH$
$O + CH_2(S) \iff H_2 + CO$	$2 H + M \iff H_2 + M$
$O + CH_2(S) \iff H + HCO$	$2 H + H_2 \iff 2 H_2$
$O + CH_3 \iff H + CH_2O$	$2 H + H_2O \iff H_2 + H_2O$
$O + CH_4 \iff OH + CH_3$	$2 H + CO_2 \iff H_2 + CO_2$
$O + CO (+ M) \iff CO_2 (+ M)$	$H + OH + M \iff H_2O + M$
$O + HCO \iff OH + CO$	$H + HO_2 \iff O + H_2O$
$O + HCO \iff H + CO_2$	$H + HO_2 \iff O_2 + H_2$
$O + CH_2O \iff OH + HCO$	$H + HO_2 \iff 2 OH$
$O + CH_2OH \iff OH + CH_2O$	$H + H_2O_2 \iff HO_2 + H_2$
$O + CH_3O \iff OH + CH_2O$	$H + H_2O_2 \iff OH + H_2O$
$O + CH_3OH \iff OH + CH_2OH$	$H + CH \iff C + H_2$
$O + CH_3OH \iff OH + CH_3O$	$H + CH_2 (+ M) \iff CH_3 (+ M)$
$O + C_2H \iff CH + CO$	$H + CH_2(S) \iff CH + H_2$
$O + C_2H_2 \iff H + HCCO$	$H + CH_3 (+ M) \iff CH_4 (+ M)$
$O + C_2H_2 \iff OH + C_2H$	$H + CH_4 \iff CH_3 + H_2$
$O + C_2H_2 \iff CO + CH_2$	$H + HCO (+ M) \iff CH_2O (+ M)$
$O + C_2H_3 \iff H + CH_2CO$	$H + HCO \iff H_2 + CO$
$O + C_2H_4 \iff CH_3 + HCO$	$H + CH_2O (+ M) \iff CH_2OH (+ M)$
$O + C_2H_5 \iff CH_3 + CH_2O$	$H + CH_2O (+ M) \iff CH_3O (+ M)$
$O + C_2H_6 \iff OH + C_2H_5$	$H + CH_2O \iff HCO + H_2$
$O + HCCO \iff H + 2 CO$	$H + CH_2OH (+ M) \iff CH_3OH (+ M)$

O + CH$_2$CO <=> OH + HCCO

O + CH$_2$CO <=> CH$_2$ + CO$_2$

O$_2$ + CO <=> O + CO$_2$

H + CH$_3$O <=> H2 + CH$_2$O

H + CH$_3$O <=> OH + CH$_3$

H + CH$_3$O <=> CH$_2$(S) + H$_2$O

H + CH$_3$O (+ M) <=> CH$_3$OH (+ M)

H + CH$_3$O <=> H + CH$_2$OH

H + CH$_3$OH <=> CH$_2$OH + H$_2$

H + CH$_3$OH <=> CH$_3$O + H$_2$

H + C$_2$H (+ M) <=> C$_2$H$_2$ (+ M)

H + C$_2$H$_2$ (+ M) <=> C$_2$H$_3$ (+ M)

H + C$_2$H$_3$ (+ M) <=> C$_2$H$_4$ (+ M)

H + C$_2$H$_3$ <=> H$_2$ + C$_2$H$_2$

H + C$_2$H$_4$ (+ M) <=> C$_2$H$_5$ (+ M)

H + C$_2$H$_4$ <=> C$_2$H$_3$ + H$_2$

H + C$_2$H$_5$ (+ M) <=> C$_2$H$_6$ (+ M)

H + C$_2$H$_5$ <=> H$_2$ + C$_2$H$_4$

H + C$_2$H$_6$ <=> C$_2$H$_5$ + H$_2$

H + HCCO <=> CH$_2$(S) + CO

H + CH$_2$CO <=> HCCO + H$_2$

H + CH$_2$CO <=> CH$_3$ + CO

H + HCCOH <=> H + CH$_2$CO

H$_2$ + CO (+ M) <=> CH$_2$O (+ M)

OH + H$_2$ <=> H + H$_2$O

2 OH (+ M) <=> H$_2$O$_2$ (+ M)

2 OH <=> O + H$_2$O

OH + HO$_2$ <=> O$_2$ + H$_2$O

OH + H$_2$O$_2$ <=> HO$_2$ + H$_2$O

OH + C <=> H + CO

OH + CH <=> H + HCO

OH + CH$_2$ <=> H + CH$_2$O

OH + CH$_2$ <=> CH + H$_2$O

OH + CH$_2$(S) <=> H + CH$_2$O

OH + CH$_3$ (+ M) <=> CH$_3$OH (+ M)

OH + CH$_3$ <=> CH$_2$ + H$_2$O

OH + CH$_3$ <=> CH$_2$(S) + H$_2$O

OH + CH$_4$ <=> CH$_3$ + H$_2$O

OH + CO <=> H + CO$_2$

OH + HCO <=> H$_2$O + CO

OH + CH$_2$O <=> HCO + H$_2$O

OH + CH$_2$OH <=> H$_2$O + CH$_2$O

OH + CH$_3$O <=> H$_2$O + CH$_2$O

OH + CH$_3$OH <=> CH$_2$OH + H$_2$O

OH + CH$_3$OH <=> CH$_3$O + H$_2$O

H + CH$_2$OH <=> H$_2$ + CH$_2$O

H + CH$_2$OH <=> OH + CH$_3$

H + CH$_2$OH <=> CH$_2$(S) + H$_2$O

OH + C$_2$H$_2$ <=> C$_2$H + H$_2$O

OH + C$_2$H$_2$ <=> CH$_3$ + CO

OH + C$_2$H$_3$ <=> H$_2$O + C$_2$H$_2$

OH + C$_2$H$_4$ <=> C$_2$H$_3$ + H$_2$O

OH + C$_2$H$_6$ <=> C$_2$H$_5$ + H$_2$O

OH + CH$_2$CO <=> HCCO + H$_2$O

2 HO$_2$ <=> O$_2$ + H$_2$O$_2$

HO$_2$ + CH$_2$ <=> OH + CH$_2$O

HO$_2$ + CH$_3$ <=> O2 + CH$_4$

HO$_2$ + CH$_3$ <=> OH + CH$_3$O

HO$_2$ + CO <=> OH + CO$_2$

HO$_2$ + CH$_2$O <=> HCO + H$_2$O$_2$

C + O$_2$ <=> O + CO

C + CH$_2$ <=> H + C$_2$H

C + CH$_3$ <=> H + C$_2$H$_2$

CH + O$_2$ <=> O + HCO

CH + H$_2$ <=> H + CH$_2$

CH + H$_2$O <=> H + CH$_2$O

CH + CH$_2$ <=> H + C$_2$H$_2$

CH + CH$_3$ <=> H + C$_2$H$_3$

CH + CH$_4$ <=> H + C$_2$H4

CH + CO (+ M) <=> HCCO (+ M)

CH + CO$_2$ <=> HCO + CO

CH + CH$_2$O <=> H + CH$_2$CO

CH + HCCO <=> CO + C$_2$H$_2$

CH$_2$ + O$_2$ => OH + H + CO

CH$_2$ + H$_2$ <=> H + CH$_3$

2 CH$_2$ <=> H$_2$ + C$_2$H$_2$

CH$_2$ + CH$_3$ <=> H + C$_2$H$_4$

CH$_2$ + CH$_4$ <=> 2 CH$_3$

CH$_2$ + CO (+ M) <=> CH$_2$CO (+ M)

CH$_2$ + HCCO <=> C$_2$H$_3$ + CO

CH$_2$(S) + N$_2$ <=> CH$_2$ + N$_2$

CH$_2$(S) + AR <=> CH$_2$ + AR

CH$_2$(S) + O$_2$ <=> H + OH + CO

CH$_2$(S) + O$_2$ <=> CO + H$_2$O

CH$_2$(S) + H$_2$ <=> CH$_3$ + H

CH$_2$(S) + H$_2$O (+ M) <=> CH$_3$OH (+ M)

CH$_2$(S) + H$_2$O <=> CH$_2$ + H$_2$O

CH$_2$(S) + CH$_3$ <=> H + C$_2$H$_4$

CH$_2$(S) + CH$_4$ <=> 2 CH$_3$

CH$_2$(S) + CO <=> CH$_2$ + CO

OH + C_2H <=> H + HCCO

OH + C_2H_2 <=> H + CH_2CO

OH + C_2H_2 <=> H + HCCOH

CH_3 + O_2 <=> O + CH_3O

CH_3 + O_2 <=> OH + CH_2O

CH_3 + H_2O_2 <=> HO_2 + CH_4

2 CH_3 (+ M) <=> C_2H_6 (+ M)

2 CH_3 <=> H + C_2H_5

CH_3 + HCO <=> CH_4 + CO

CH_3 + CH_2O <=> HCO + CH_4

CH_3 + CH_3OH <=> CH_2OH + CH_4

CH_3 + CH_3OH <=> CH_3O + CH_4

CH_3 + C_2H_4 <=> C_2H_3 + CH_4

CH_3 + C_2H_6 <=> C_2H_5 + CH_4

HCO + H_2O <=> H + CO + H_2O

HCO + M <=> H + CO + M

HCO + O_2 <=> HO_2 + CO

CH_2OH + O_2 <=> HO_2 + CH_2O

CH_3O + O_2 <=> HO_2 + CH_2O

C_2H + O_2 <=> HCO + CO

C_2H + H_2 <=> H + C_2H_2

C_2H_3 + O_2 <=> HCO + CH_2O

C_2H_4 (+ M) <=> H_2 + C_2H_2 (+ M)

C_2H_5 + O_2 <=> HO_2 + C_2H_4

HCCO + O_2 <=> OH + 2 CO

2 HCCO <=> 2 CO + C_2H_2

N + NO <=> N_2 + O

N + O_2 <=> NO + O

N + OH <=> NO + H

N_2O + O <=> N_2 + O_2

N_2O + O <=> 2 NO

N_2O + H <=> N_2 + OH

N_2O + OH <=> N_2 + HO_2

N_2O (+ M) <=> N_2 + O (+ M)

HO_2 + NO <=> NO_2 + OH

NO + O + M <=> NO_2 + M

NO_2 + O <=> NO + O_2

NO_2 + H <=> NO + OH

NH + O <=> NO + H

NH + H <=> N + H_2

NH + OH <=> HNO + H

NH + OH <=> N + H_2O

NH + O_2 <=> HNO + O

NH + O_2 <=> NO + OH

NH + N <=> N_2 + H

CH_2(S) + CO2 <=> CH_2 + CO_2

CH_2(S) + CO_2 <=> CO + CH_2O

CH_2(S) + C_2H_6 <=> CH_3 + C_2H_5

NH_2 + O <=> OH + NH

NH_2 + O <=> H + HNO

NH_2 + H <=> NH + H_2

NH_2 + OH <=> NH + H_2O

NNH <=> N_2 + H

NNH + M <=> N_2 + H + M

NNH + O2 <=> HO_2 + N_2

NNH + O <=> OH + N_2

NNH + O <=> NH + NO

NNH + H <=> H_2 + N_2

NNH + OH <=> H_2O + N_2

NNH + CH_3 <=> CH_4 + N_2

H + NO + M <=> HNO + M

HNO + O <=> NO + OH

HNO + H <=> H_2 + NO

HNO + OH <=> NO + H_2O

HNO + O_2 <=> HO_2 + NO

CN + O <=> CO + N

CN + OH <=> NCO + H

CN + H_2O <=> HCN + OH

CN + O_2 <=> NCO + O

CN + H_2 <=> HCN + H

NCO + O <=> NO + CO

NCO + H <=> NH + CO

NCO + OH <=> NO + H + CO

NCO + N <=> N_2 + CO

NCO + O_2 <=> NO + CO_2

NCO + M <=> N + CO + M

NCO + NO <=> N_2O + CO

NCO + NO <=> N_2 + CO_2

HCN + M <=> H + CN + M

HCN + O <=> NCO + H

HCN + O <=> NH + CO

HCN + O <=> CN + OH

HCN + OH <=> HOCN + H

HCN + OH <=> HNCO + H

HCN + OH <=> NH_2 + CO

H + HCN (+ M) <=> H_2CN (+ M)

H_2CN + N <=> N_2 + CH_2

C + N_2 <=> CN + N

CH + N_2 <=> HCN + N

CH + N_2 (+ M) <=> HCNN (+ M)

NH + H$_2$O <=> HNO + H$_2$

NH + NO <=> N$_2$ + OH

NH + NO <=> N$_2$O + H

C + NO <=> CO + N

CH + NO <=> HCN + O

CH + NO <=> H + NCO

CH + NO <=> N + HCO

CH$_2$ + NO <=> H + HNCO

CH$_2$ + NO <=> OH + HCN

CH$_2$ + NO <=> H + HCNO

CH$_2$(S) + NO <=> H + HNCO

CH$_2$(S) + NO <=> OH + HCN

CH$_2$(S) + NO <=> H + HCNO

CH$_3$ + NO <=> HCN + H$_2$O

CH$_3$ + NO <=> H$_2$CN + OH

HCNN + O <=> CO + H + N$_2$

HCNN + O <=> HCN + NO

HCNN + O$_2$ <=> O + HCO + N$_2$

HCNN + OH <=> H + HCO + N$_2$

HCNN + H <=> CH$_2$ + N$_2$

HNCO + O <=> NH + CO$_2$

HNCO + O <=> HNO + CO

HNCO + O <=> NCO + OH

HNCO + H <=> NH$_2$ + CO

HNCO + H <=> H2 + NCO

HNCO + OH <=> NCO + H$_2$O

HNCO + OH <=> NH$_2$ + CO$_2$

HNCO + M <=> NH + CO + M

HCNO + H <=> H + HNCO

HCNO + H <=> OH + HCN

HCNO + H <=> NH$_2$ + CO

HOCN + H <=> H + HNCO

HCCO + NO <=> HCNO + CO

CH$_3$ + N <=> H2CN + H

CH$_3$ + N <=> HCN + H$_2$

NH$_3$ + H <=> NH$_2$ + H$_2$

NH$_3$ + OH <=> NH$_2$ + H$_2$O

NH$_3$ + O <=> NH$_2$ + OH

NH + CO$_2$ <=> HNO + CO

CN + NO$_2$ <=> NCO + NO

NCO + NO$_2$ <=> N$_2$O + CO$_2$

N + CO$_2$ <=> NO + CO

O + CH$_3$ => H + H$_2$ + CO

O + C$_2$H$_4$ <=> H + CH$_2$CHO

CH2 + N$_2$ <=> HCN + NH

CH$_2$(S) + N$_2$ <=> NH + HCN

C + NO <=> CN + O

O + C$_2$H$_5$ <=> H + CH$_3$CHO

OH + HO$_2$ <=> O$_2$ + H$_2$O

OH + CH$_3$ => H$_2$ + CH$_2$O

CH + H$_2$ (+ M) <=> CH$_3$ (+ M)

CH$_2$ + O$_2$ => 2 H + CO$_2$

CH$_2$ + O$_2$ <=> O + CH$_2$O

CH$_2$ + CH$_2$ => 2 H + C$_2$H$_2$

CH$_2$(S) + H$_2$O => H$_2$ + CH$_2$O

C$_2$H$_3$ + O$_2$ <=> O + CH$_2$CHO

C$_2$H$_3$ + O$_2$ <=> HO$_2$ + C$_2$H$_2$

O + CH$_3$CHO <=> OH + CH$_2$CHO

O + CH$_3$CHO => OH + CH$_3$ + CO

O$_2$ + CH$_3$CHO => HO$_2$ + CH$_3$ + CO

H + CH$_3$CHO <=> CH$_2$CHO + H$_2$

H + CH$_3$CHO => CH$_3$ + H$_2$ + CO

OH + CH$_3$CHO => CH$_3$ + H$_2$O + CO

HO$_2$ + CH$_3$CHO => CH$_3$ + H$_2$O$_2$ + CO

CH$_3$ + CH$_3$CHO => CH$_3$ + CH$_4$ + CO

H + CH$_2$CO (+ M) <=> CH$_2$CHO (+ M)

O + CH$_2$CHO => H + CH$_2$ + CO$_2$

O$_2$ + CH$_2$CHO => OH + CO + CH$_2$O

O$_2$ + CH$_2$CHO => OH + 2 HCO

H + CH$_2$CHO <=> CH$_3$ + HCO

H + CH$_2$CHO <=> CH$_2$CO + H$_2$

OH + CH$_2$CHO <=> H$_2$O + CH$_2$CO

OH + CH$_2$CHO <=> HCO + CH$_2$OH

CH$_3$ + C$_2$H$_5$ (+ M) <=> C$_3$H$_8$ (+ M)

O + C$_3$H$_8$ <=> OH + C$_3$H$_7$

H + C$_3$H$_8$ <=> C$_3$H$_7$ + H$_2$

OH + C$_3$H$_8$ <=> C$_3$H$_7$ + H$_2$O

C$_3$H$_7$ + H$_2$O$_2$ <=> HO$_2$ + C$_3$H$_8$

CH$_3$ + C$_3$H$_8$ <=> C$_3$H$_7$ + CH$_4$

CH$_3$ + C$_2$H$_4$ (+ M) <=> C$_3$H$_7$ (+ M)

O + C$_3$H$_7$ <=> C$_2$H$_5$ + CH$_2$O

H + C$_3$H$_7$ (+ M) <=> C$_3$H$_8$ (+ M)

H + C$_3$H$_7$ <=> CH$_3$ + C$_2$H$_5$

OH + C$_3$H$_7$ <=> C$_2$H$_5$ + CH$_2$OH

HO$_2$ + C$_3$H$_7$ <=> O$_2$ + C$_3$H$_8$

HO$_2$ + C$_3$H$_7$ => OH + C$_2$H$_5$ + CH$_2$O

CH$_3$ + C$_3$H$_7$ <=> 2 C$_2$H$_5$

Appendix B: Transport properties

The temperature dependence of the transport properties μ and λ influences the heat exchange between the hot gas in the boundary layer and the thrust chamber walls. The modeling of these parameters is discussed in Section 2.2.3.

A tabulation of the parameters $A - D$ in Eq. (2.29) can be found in Svehla [26]. Another method lies in using the transport properties of the GRI 3.0 mechanism. As described in Section 3.2.2, the GRI 3.0 mechanism is imported in Cantera and consists of three files: the reactions list, the thermodynamic data and the kinetic/transport properties. The transport properties file is used by Cantera to determine the viscosity and heat conductivity of the individual species and the mixture by utilizing the equations in Section 3.2.2.

A comparison between the data from Cantera and the GRI 3.0 mechanism (which stem from the Chapman-Enskog model) and the NASA Lewis CEA data presented in Svehla (which result from experimental measurements) can be seen in Figure B.1.

Within the relevant temperature range for rocket engine applications (200 K-3500 K), the values calculated in Cantera show a satisfactory agreement with the experimental fit. A discrepancy is observed for higher temperatures (T>1500 K) especially for hydrogen. However, it is important to mention, that these molecular properties are mainly important in the boundary layer, where the gas temperature rarely exceeds 1000 K. Up to this temperature value, the two methods give almost identical results.

A drawback observed in the parameters of NASA Lewis CEA is that the coefficients for certain species and mainly radicals, are defined only for the higher temperature range >1000 K. This is understandable, because the specific species do not occur for low temperatures, due to rapid recombination. In a CFD calculation however, the mass fraction of those species, can be non-zero even at lower temperatures. Using the exponential function from Eq. (2.29) in this lower temperature range would lead to an extrapolation of the data and to non-physical data for μ and λ. This effect is illustrated in Figure B.2. The heat conductivity for the hydrogen and oxygen radicals (H and O respectively) is plotted as a function of temperature. Both species are defined only for the higher temperature range in Svehla [26]. Extrapolating the data for lower temperatures leads to unphysical profiles and could eventually produce even negative values for the transport properties.
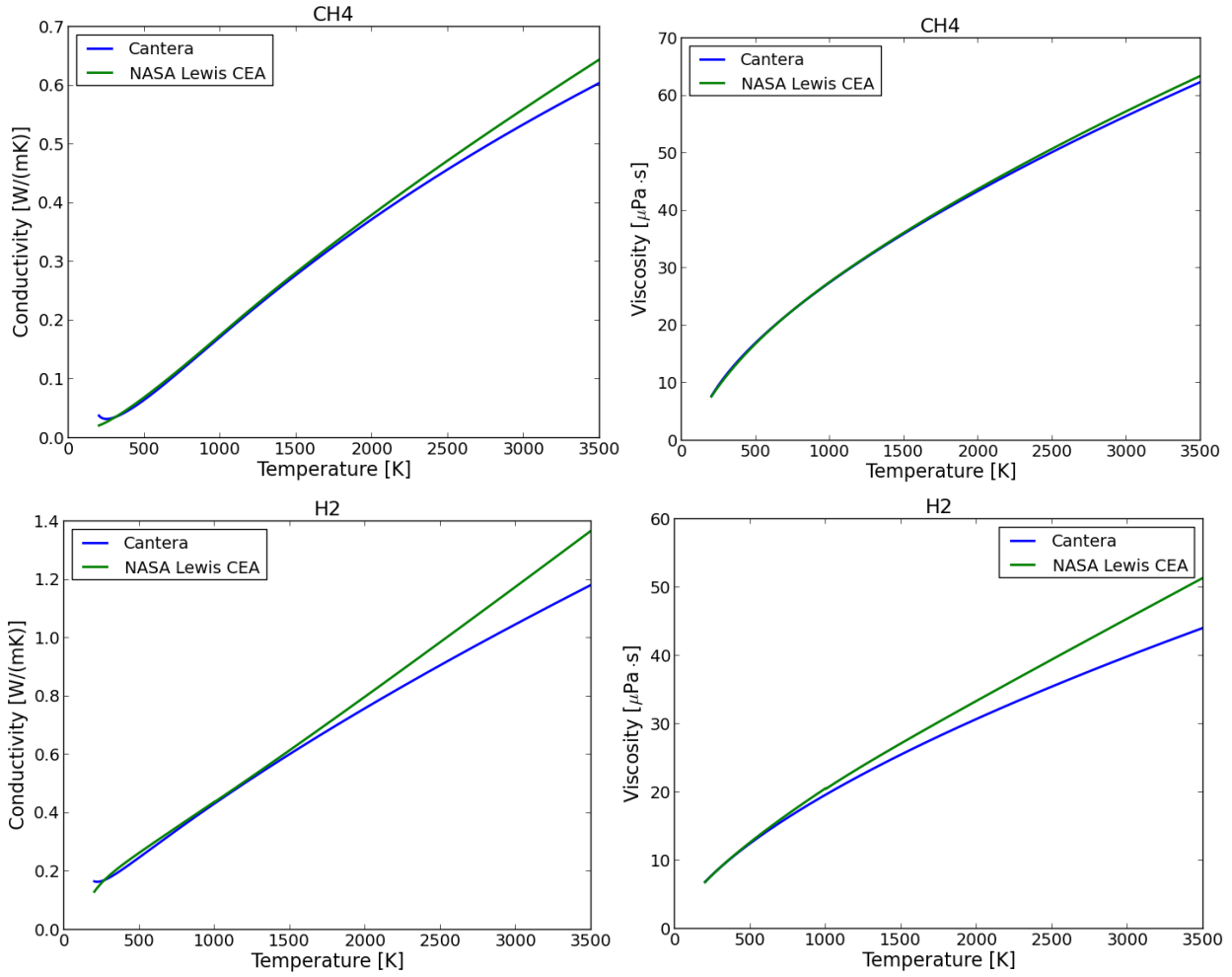
Figure B.1: Heat conductivity (left) and dynamic viscosity (right) temperature profiles for methane (up) and hydrogen (down) molecules.
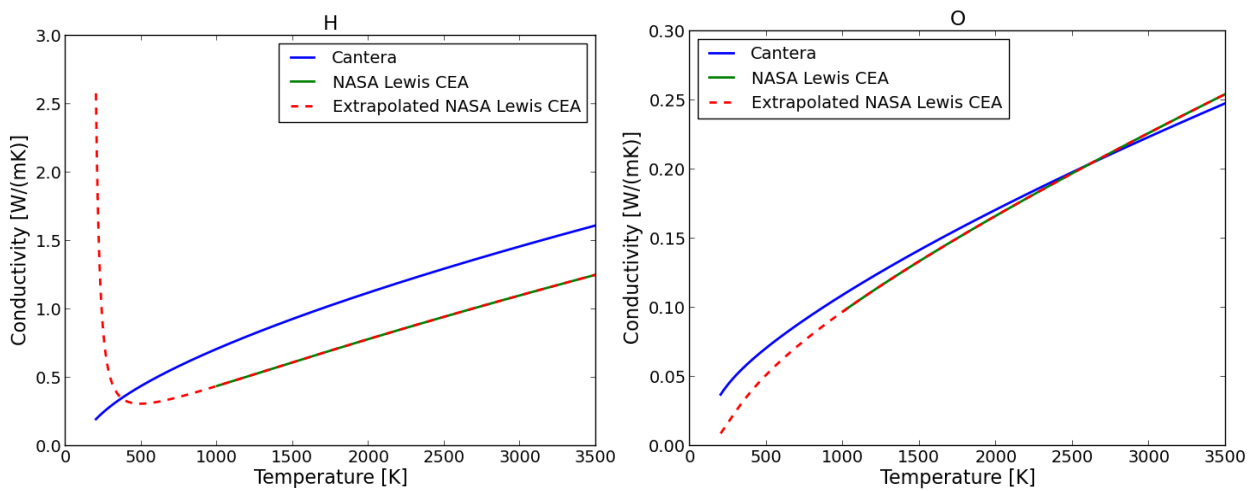
Figure B.2: Heat conductivity profiles as a function of temperature for hydrogen (left) and oxygen (right) radicals.

To avoid this issue, the values taken from Cantera were used for the ANSYS CFX calculations. A fit for the temperature profiles was performed in Python, leading to the parameters $A - D$ for the formula of Eq. (2.29). In order to generate the fit, the built-in function "curve_fit" was utilized in Pyhton. The temperature dependent profile was then implemented in CFX in the form of an "Expression" for each species.

Appendix C: Numerical treatment of β-PDF

In order to produce the turbulent Flamelet table from the laminar calculation results obtained with Cantera, the integration in Eq. (C.1) has to be performed.

$$\int_0^1 P(Z) \cdot Y_i(Z) \, \mathrm{d}Z \qquad\qquad (C.1)$$

Carrying out the integration causes a singularity to appear at $Z = 0$ if $\alpha < 1$ and one at $Z = 1$ if $\beta < 1$, as described in Section 3.5. To perform the numerical integration with the trapezoidal rule, no singularities are allowed and for that reason, the PDF is modified close to the location of singularity. To demonstrate this process, an example is used, with a β-PDF having the parameters $\alpha = \beta = 0.3$, as illustrated in Figure C.1.

Examining the values of the PDF close to the origin, one observes, that the value becomes infinite only for $Z = 0$ and is finite for any other mixture fraction $Z = 0 + \epsilon$. This is therefore the only value that needs to be replaced to avoid the singularity. The condition for replacing the value at origin, is that the area of the analytic PDF between the first $(Z_1 = 0)$ and second $(Z_2 = 0.02$ in this example) grid points has to be equal to the area of the approximating function. This ensures, that the condition

$$\int_0^1 P(Z) \, \mathrm{d}Z = 1$$

holds for the approximating function as well. Hence this requires that the two shaded areas in Figure C.1 are equal. Expressed in another way, the area of the trapezoid ABCD should be equal to the integral

$$\int_{Z_1=0}^{Z_2} P(Z) \, \mathrm{d}Z \qquad\qquad (C.2)$$

and from this condition, the replacement value x can be obtained:

$$\frac{[x + P(Z_2)]}{2} \cdot (Z_2 - Z_1) = \int_{Z_1=0}^{Z_2} P(Z) \, \mathrm{d}Z \qquad\qquad (C.3)$$

And with $Z_1 = 0$:

$$x = \frac{2}{Z_2} \cdot \int_0^{Z_2} P(Z) \, \mathrm{d}Z - P(Z_2) \qquad (C.4)$$
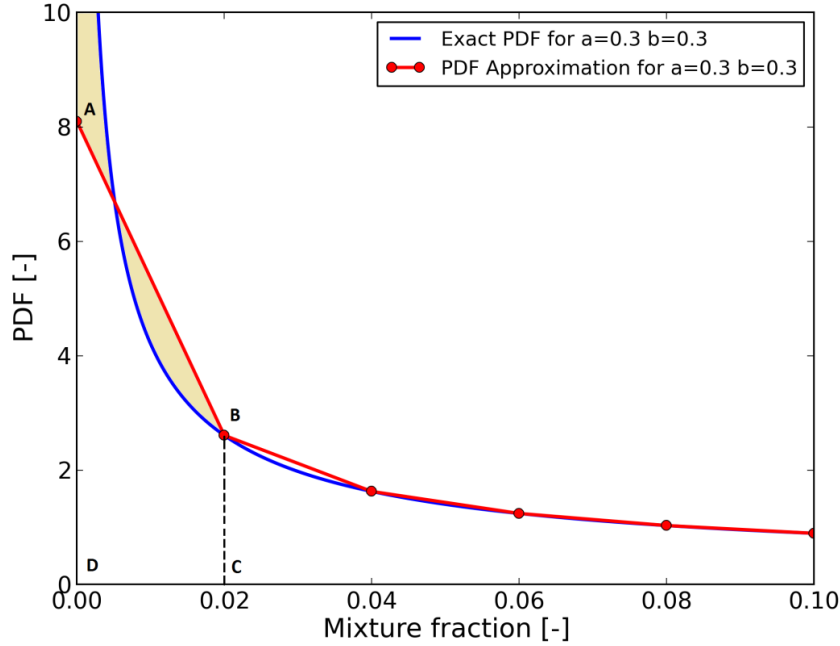
Figure C.1: Demonstration of the approximating β-PDF in the case of singularity.

The integral in Eq. (C.4) is equal to the value of the CDF at $Z = Z_2$ and is hence obtained analytically. Of course, the grid for the integration has to be chosen fine enough, in order to minimize the numerical error, by having a sufficiently small value for Z_2. The same process applies in case of a singularity at $Z = 1$.

A separate method for the approximation of the β-PDF in the vicinity of zero in the case of singularity is given by Brizuela in [65]. There, the PDF is approximated as

$$P(Z) = \frac{Z^{\alpha-1}(1-Z)^{\beta-1}}{\alpha+\beta} \cdot \alpha \cdot \beta \qquad (C.5)$$

Both methods yielded the same results within the measurable accuracy but the trapezoidal replacement was the one implemented eventually.

Appendix D: Effect of transport properties on Cantera Flamelet tables

As described in Section 3.3, generating the Flamelet tables using Cantera, does not involve solving the Flamelet equations (Eqs. (2.66)-(2.67)). Instead, the 1D flow problem is solved in the physical space. In contrast to the solution of the Flamelet equations, the PDEs in the physical space do not include the scalar dissipation as an input parameter. Hence, the limit of $\chi \to 0\,s^{-1}$ does not correspond to the chemical equilibrium mathematically, as is the case for the Flamelet equations (shown in Eq. (2.68)).

This can be also better understood when taking into account, that the transport properties of the fluid (dynamic viscosity and thermal conductivity), are required for the solution of the 1D counterflow diffusion flames. In the case of chemical equilibrium calculations, the transport properties are not part of the solution, since it is merely the 0D problem of minimizing the Gibb's free enthalpy. One would therefore expect that the counterflow diffusion flame does not exactly converge to the equilibrium solution for arbitrarily small scalar dissipation.

In order to examine this, the solution of the 1D counterflow flame was undertaken, with varying the transport coefficients (μ, λ) of the mixture. The variation was done by altering the collision diameter in the Lennard-Jones potential (σ_i), which directly correlates to the dynamic viscosity and thermal conductivity as in Eq. (3.11) and (3.14).

Four cases were compared to each other, one with the default transport properties and 3 with double, fourfold and tenfold value for σ_i, meaning a 25%, 6% and 1% value of the transport properties respectively. The operating point of 47 bar was chosen, with 300 K inlet temperature of oxidizer and fuel. The results for a H_2/O_2 combustion were obtained and are plotted in Figure D.1.
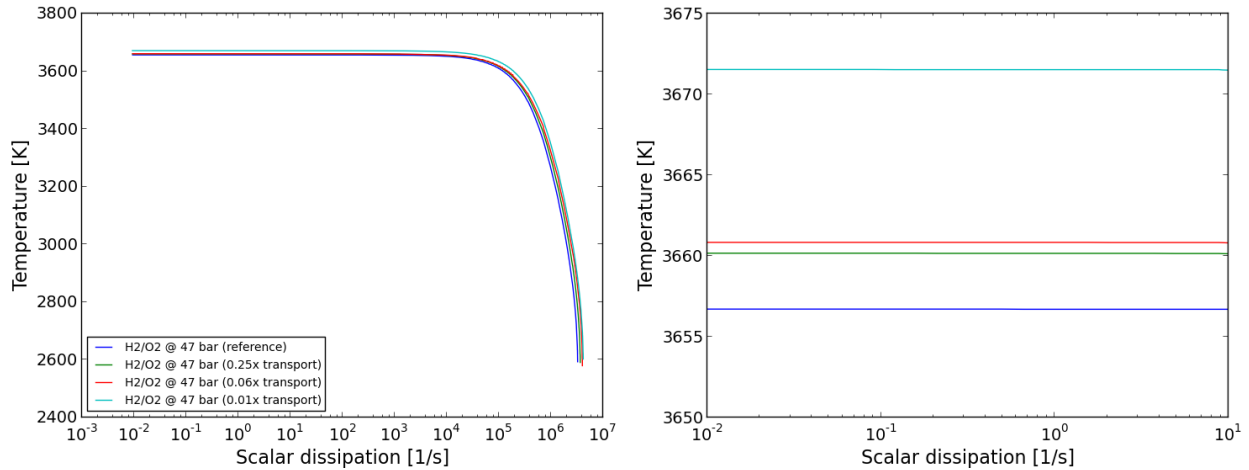
Figure D.1: Maximal flame temperature as a function of the scalar dissipation rate for different values of the transport parameters.

It is evident from the right plot in Figure D.1, that the calculated temperature for $\chi \rightarrow 0\,\mathrm{s}^{-1}$, demonstrates slight differences in the four cases described above. The discrepancy remains underneath 15 K (approximately 0.4%) and is hence negligible. It still however serves the point of shown that the 1D flow problem in physical coordinates is dependent on the chosen transport model and is not mathematically strictly equivalent to the equilibrium solution as χ approaches 0, but can still be used without significant departure from the exact solution.

Appendix E: Comparison of Flamelet tables

Before the simulation of each test case with CFX, the Flamelet tables produced by Cantera and RIF were compared to each other. Understanding the underlying differences in the structure of the tables can help identify the observed discrepancies in the final CFD results.

For the comparison of the tables, an existing visualization tool written in C was modified. Giving as an input the desired values for scalar dissipation and variance of the mixture fraction, the program was used to transform the .fll files into a format readable by Tecplot360.

The results for ISP-1 test case are shown and discussed in this section. Only some representative 2D plots are included in this comparison, since the visualization of the complete Flamelet table would be too extensive. The main differences between Cantera and RIF remain unaltered at all pressure levels, and hence the tables at 40 bar (Romeo test case) are not shown.

The equilibrium solution in the context of the used Flamelet tables is defined as the solution corresponding to the lowest value for the scalar dissipation χ. The lowest value in the case of the Cantera table is $0.02 \, s^{-1}$., whereas in the case of RIF it goes as low as $10^{-8} \, s^{-1}$. At this point it is important to note, the difference in the definition of the scalar dissipation between the two methods, which is done *a posteriori* in the case of Cantera and *a priori* in the RIF case. The results for the equilibrium results is given in Figure E.1.
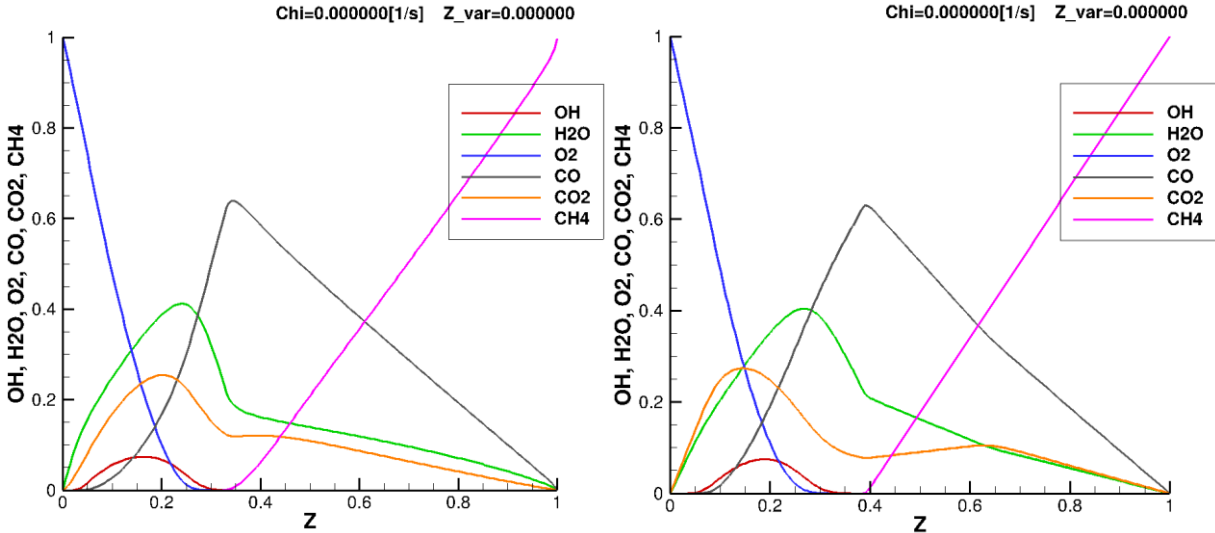
Figure E.1: Flamelet table visualization for the ISP-1 test case: equilibrium solution (Cantera table: left, RIF table: right)

The profiles of the major species (O_2, CH_4, CO_2, H_2O, CO, OH) appear to be quite similar in both cases, although some differences can be observed. For values of the mixture fraction smaller than 0.2, Cantera predicts that the H_2O mass fraction exceeds the one of CO_2, whereas RIF shows otherwise. Moreover, the CO_2 profile coming from RIF shows a second local maximum close to $Z = 0.65$, while Cantera predicts this second value close to $Z = 0.4$. The results stemming from the RIF calculation are in compliance with the findings presented in Section 4.1, where the equilibrium solution from CEA was presented. This implies that the RIF solution for $\chi \rightarrow 0\,s^{-1}$ has the same form as the theoretical equilibrium.

For higher values of the scalar dissipation rate, as shown in Figure E.2 and Figure E.3, some differences still remain. The Cantera solution seems to deliver a sharp decrease of the H_2O mass fraction profile after the $Z = 0.25$ mark, whereas RIF has a nearly linear drop. Finally, the CO concentration appears to be larger in the case of Cantera.

These differences are a product of the inconsistency between two sets of equations: RIF solves the Flamelet equations directly, whereas Cantera solves the 1D flame problem. This difference in the nature of the problem solved leads to those subtle discrepancies. Moreover the applied reaction mechanism is different in both cases (C1 mechanism in the case of RIF and GRI 3.0 in Cantera). However, the form of the profiles remains the same when comparing the two methods and therefore, only small deviations are expected in the final CFD results.
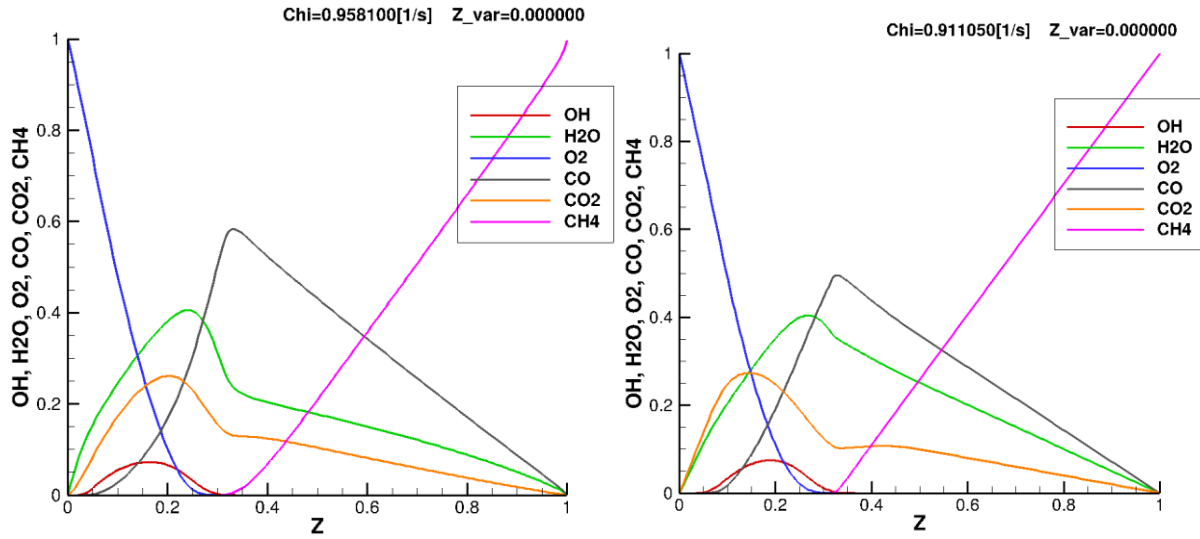
Figure E.2: Flamelet table visualization for the ISP-1 test case: $\chi = 1\ \mathrm{s}^{-1}$, $\widetilde{Z''}_{norm} = 0$
(Cantera table: left, RIF table: right)
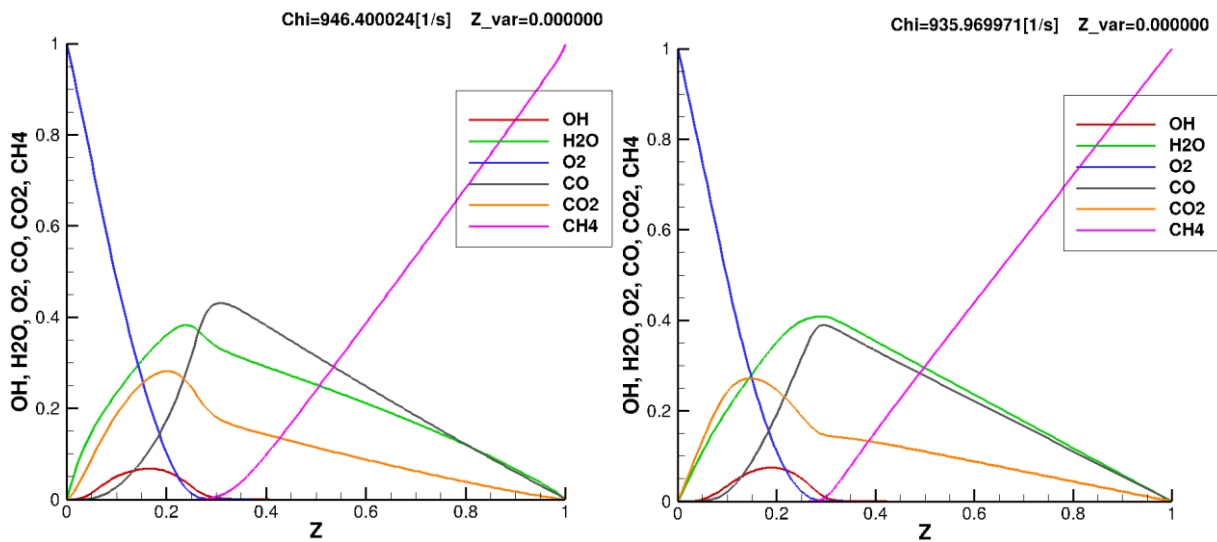
Figure E.3: Flamelet table visualization for the ISP-1 test case: $\chi = 1000\ \mathrm{s}^{-1}$, $\widetilde{Z''}_{norm} = 0$
(Cantera table: left, RIF table: right)

Appendix F: Calculation of the combustion efficiency

The calculation of the combustion efficiency η_{c^*} requires knowledge of the characteristic velocity stemming from the simulation results, as well as information about the theoretical characteristic velocity for the specific propellant combination at the examined operating conditions (pressure and O/F).

In order to calculate the simulated characteristic velocity, the properties of the flow resulting from the simulation (total pressure at throat, mass flow rate) and the throat cross sectional area are used as in Eq. (2.5). The main difficulty lies in the estimation of the total pressure at the throat. This is implemented by means of the isentropic expression, using the static pressure at throat p and the Mach number Ma:

$$p_c = p\left(1 + \frac{\gamma - 1}{2}Ma^2\right)^{\frac{\gamma}{\gamma - 1}} \tag{F.1}$$

The calculation of the adiabatic coefficient γ occurs using the speed of sound c_s at the throat location by making the assumption of an ideal gas (which is sufficient at the high temperatures present in the nozzle):

$$\gamma = \frac{c_s^2 p}{\rho} \tag{F.2}$$

The theoretical value for c^* was obtained using the CEA code by Gordon et al. [54]. The inputs required for the calculation of the "Simple Rocket Problem" which delivers the theoretical characteristic velocity, were fed to CEA directly from the CFX results. As Figure F.1 illustrates, the total pressure at the faceplate and the throat, the mass flow rate and inlet temperature of oxidizer and fuel, the simulated characteristic velocity and the total integrated heat release in the combustion chamber (up to the throat) were sent to the CEA interface.

In the CEA calculation, the assumption of an adiabatic flow is made, which implies that no energy is lost to the wall through heat transfer. However, in reality and in the simulated case, a significant portion of the energy escapes the combustion chamber through interaction with the wall and is not available for the combustion. This is also why the integrated heat loss to the wall is needed for the calculation. In order to include the non-adiabatic effect in the CEA simulation, the initial enthalpy of the propellants is reduced by the same amount of heat that escaped through the walls in the simulation. Hence, the

adiabatic problem is solved but with a reduced initial enthalpy of the propellants, which mimics the effect of energy loss. Both the adiabatic and the non-adiabatic values for c^* are calculated, leading to two different values for the efficiency η_{c^*}. In the comparisons made in the present thesis, only the corrected value was examined since it includes the non-adiabatic effects present in the operation of a real rocket engine.
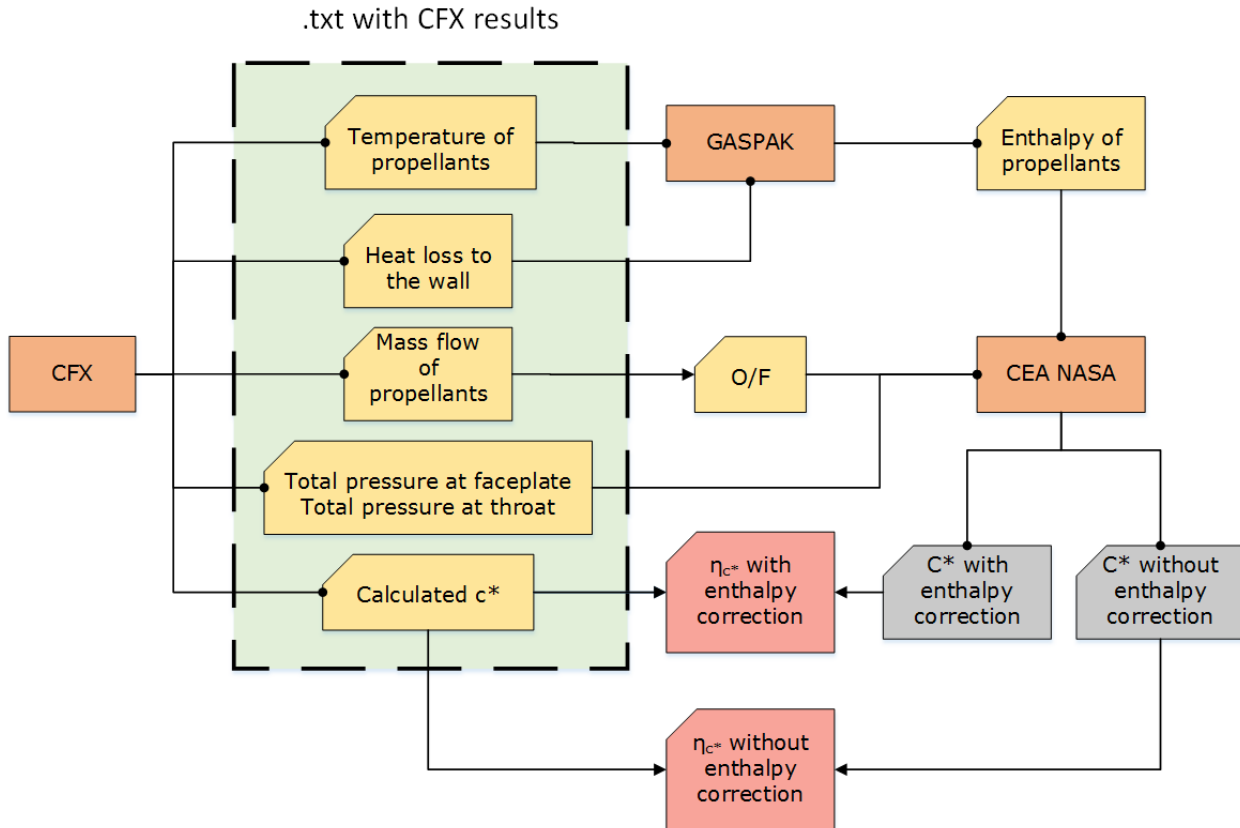
Figure F.1: Flow chart of the calculation process for the efficiency of the characteristic velocity.

Appendix G: Oxygen and Methane thermodynamic properties
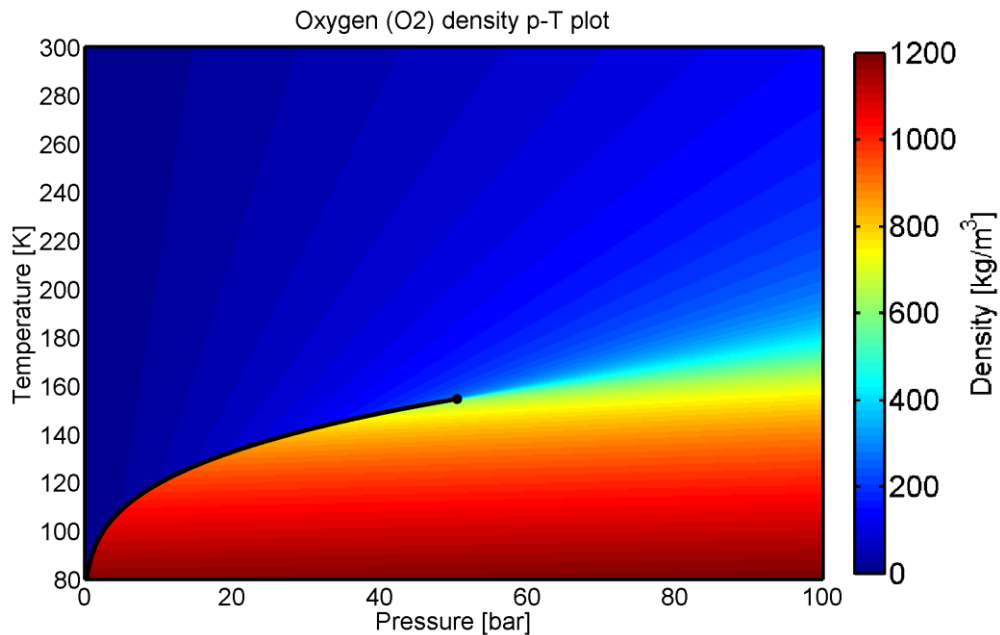
Figure G.1: Density plot for oxygen as a function of temperature and pressure. Plot generated using data from the National Institute of Standards and Technology (NIST) [8].
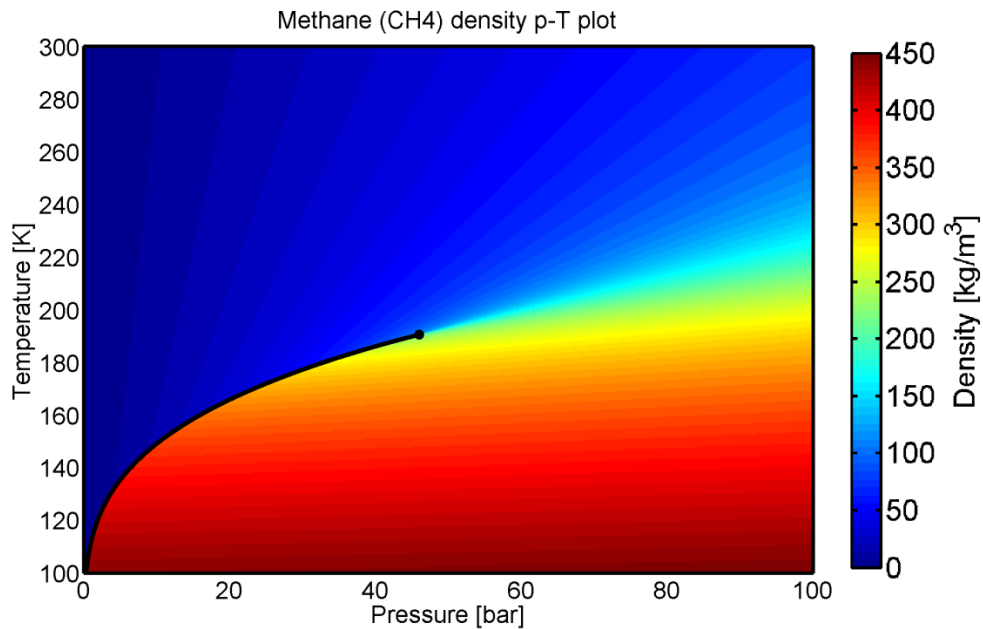
Figure G.2: Density plot for methane as a function of temperature and pressure. Plot generated using data from the National Institute of Standards and Technology (NIST) [8].
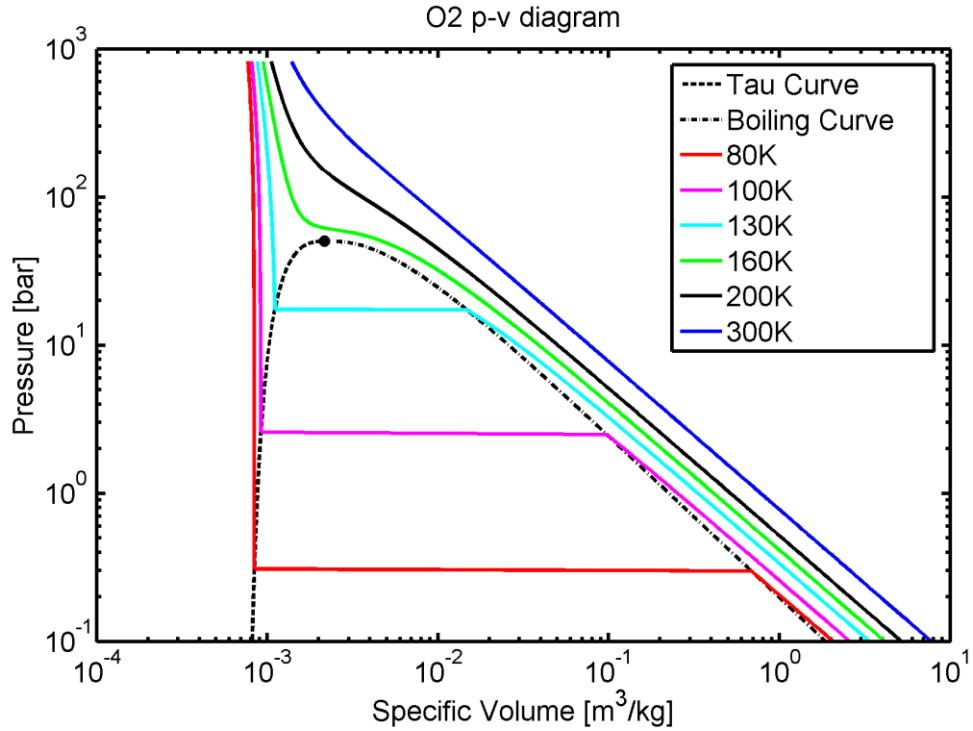
Figure G.3: p-v diagram for oxygen. Plot generated using data from the National Institute of Standards and Technology (NIST) [8].
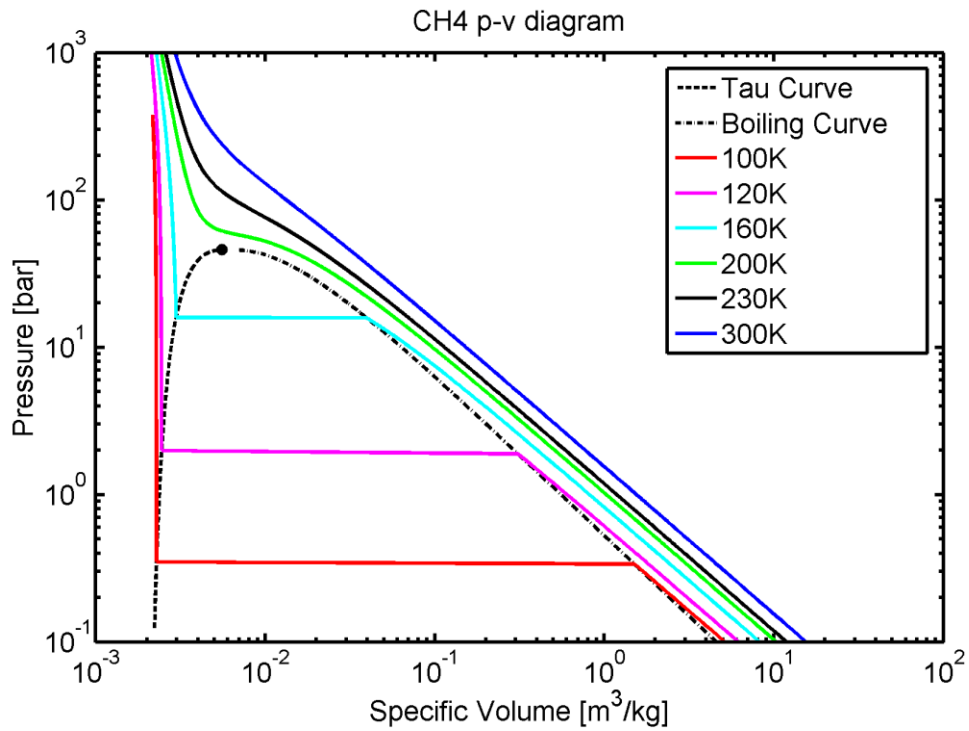
Figure G.4: p-v diagram for methane. Plot generated using data from the National Institute of Standards and Technology (NIST) [8].

Appendix H: User's guide for the Flamelet generator

The basic instructions for running the Cantera/Python Flamelet generator are outlined here. A description of the way the code is structured and the calculation process are presented in Chapter 3.

The first step for running the Flamelet generator, is installing Python and Cantera as well as establishing the interface between the two programs. In the present work, version 2.7 of Python and version 2.2.1 of Cantera were used.

Before using Cantera, it is recommended to run the setup script which configures its environment. This is done by typing into the console.

```
source /a4/cantera/2.2.1/bin/setup_cantera
```

In order to start the main program, the working directory has to be set to the path where the code is located. For example:

```
cd
cd /home/perakis/Documents/Flamelet_Tabellengenerator_Perakis
```

To start the main file "Flamelet-Tabellengenerator.py", the following command has to be given into the bash-shell:

```
python2.7 Flamelet-Tabellengenerator.py
```

User Inputs

The settings for the Flamelet table generation are given by the user in a separate file ("User_inputs.py"), also located in the same directory as the main code, and which is called by Flamelet-Tabellengenerator.py. The contents of this file are given here for clarity:

```
# -*- coding: utf-8 -*-

'''
The boundary conditions and the user settings are defined with this script.
The script is called by the main file "Flamelet-Tabellengenerator.py".
'''
def Def_Inputs():

        # ------------------------ Input ------------------------------------
        #Definition of the stoichiometric mixture fraction ( CH4 + 2 O2 --> 2 H2O + CO2 )
        Zstoich = 1.0/5.0  # stoichiometric mixture fraction (for h2/o2: 1.0/9.0)

        #Number of the oxygen atoms in the reactants of the stoichiometric reaction.  (4 for methane
        combustion, 2 for hydrogen combustion)
        n_O = 4

        #Number of the oxygen atoms in the reactants of the stoichiometric reaction.  (4 for methane
        combustion, 4 for hydrogen combustion)
        n_H = 4

        #Number of the oxygen atoms in the reactants of the stoichiometric reaction.  (1 for methane
        combustion, 0 for hydrogen combustion)
        n_C = 1


        # ------------------------ 1st Input ------------------------------------
        # Should the boundary conditions be given manually in the console or through this script?
        # True  --> The boundary conditions (T,p,mass fractions) are given by the user in the console and
        the values in this script are ignored
        # False --> The user does not give any inputs into the console. All BCs are taken from this file.
        GUIinput = False
        # ------------------------ 2nd Input ------------------------------------
        # Pressure in [bar]
        Pressure = 40

        # ------------------------ 3rd Input ------------------------------------
        # Inlet temperature of fuel in [K]
        # The lowest allowed temperature is 200 K.
        # Smaller values are replaced by 200 K.
        T_inlet_fuel = 280

        # ------------------------ 4th Input ------------------------------------
        # Inlet temperature of oxidizer in [K]
        # The lowest allowed temperature is 200 K.
        # Smaller values are replaced by 200 K.
        T_inlet_ox = 200.5

        # ------------------------ 5th Input ------------------------------------
        # Mass fractions at the fuel inlet
        # Using the Cantera format: 'species1:Y1, species2:Y2, .... , speciesN:YN'
        # for example: Y_fu='CH4:0.9, N2:0.05, H2:0.05'
        # If the sum of mass fractions is larger than 1, then it is normalized
        # e.g.: T_fu='CH4:3, N2:1, H2:1'  is transformed to 60% CH4, 20% N2 und 20% H2
        # Do not include species with 0 mass fraction: e.g.  'CH4:1, N2:0' produces an error
```

Y_fu = 'CH4:1'

# ----------------------- 6th Input -----------------------------------
# Mass fractions at the oxidizer inlet
# Using the Cantera format: 'species1:Y1, species2:Y2, ... , speciesN:YN'
# for example: Y_ox=O2:0.9, CO2:0.05, H2O:0.05'
# If the sum of mass fractions is larger than 1, then it is normalized
# e.g.: T_ox='O2:3, CO2:1, H2O:1' is transformed to 60% O2, 20% CO2 und 20% H2O
# Do not include species with 0 mass fraction: e.g. O2:1, N2:0' produces an error
Y_ox = 'O2:1'

# ----------------------- 7th Input -----------------------------------
# The path of the file containing the reaction mechanism
# 2 formats are allowed:
# 1) .xml file
# 2) .cti file
# The absolute path should be given, e.g.:
mech_file='/home/perakis/Documents/Flamelet_Tabellengenerator_Perakis/Reaktionsmechanism
us/test_mech.cti'
# If a mechanism is used, which is built-in in Cantera, then just giving the name suffices e.g.
mech_file='gri30.cti'
mech_file = 'gri30.cti'

----------------------- 8th Input -----------------------------------
Should the reaction mechanism be reduced?
The user can input "1" or "0"
Should the user input "1" and should there be no nitrogen in the inlets, then all reactions and
species containing nitrogen are removed. Same for carbon
reduce_m = 1

# ----------------------- 9th Input -----------------------------------
# Which species should be removed from the reaction mechanism?
# This variable is only taken into account, if the user has defined "reduce_m" with a "1"
# The user can only input species, which are not present in the fuel or oxidizer inlets
# It should be given as a list of strings, separated by commas e.g. ['CO','OH'].
# If one of the given species is not present in the reaction mechanism, it is ignored
# If no species are to be ignored, then simply input 0
species_to_del = 0

----------------------- 10th Input -----------------------------------
Path of starting solution
If the user gives a 0 (recommended), then the code uses an already converged solution for the
calculation
#ini_sol='/home/perakis/Documents/Flamelet_Tabellengenerator_Perakis/Initialloesungen/ini_1ba
r.xml'
ini_sol = 0

# ----------------------- 11th Input -----------------------------------
# Which PDF integrator should be used?
# If the user inputs the value 1, then the Python-based PPDF integrator is used.
# Otherwise, canterToFoam is used. This implies that OpenFOAM has to be installed
pdf_intern = 1

```
# ----------------------- 12th Input -------------------------------------
# Which PDF-type shold be used? (only taken into account for the Python-based integrator)
# There is the option 'beta' and the option 'gauss'.
pdf_method = 'beta'

# ----------------------- 13th Input -------------------------------------
# Name of the .fll table.
# If the value 0 is given, then the code generates an automatic name based on the BCs
tabelle_name = 'Romeo_40bar.fll'

# ----------------------- 14th Input -------------------------------------
# If the mass fraction of any species is larger than this value, then this species is not used in the
.fll table and hence also not modeled in CFX
# when the value 0 is given, then no species are removed.
limit_include = 1e-6

# ----------------------- 15th Input -------------------------------------
# Should a CCL file be exported, with the transport and thermodynamic properties of the species?
(True or False)
CCL = True

# ----------------------- 16th Input -------------------------------------
# Name of the .ccl file. When a 0 is given, then the name is determined automatically.
# e.g. 'test_ccl.ccl'
ccl_name = 0

# ----------------------- 17th Input -------------------------------------
# The .csv file, containing the NASA polynomials. Used for the generation of the CCL file.
thermo_csv =
"/home/perakis/Documents/Flamelet_Tabellengenerator_Perakis/CCL/grimech30_original.csv"



# ----------------------- 18th Input -------------------------------------
# The .csv file, containing the transport coefficients. Used for the generation of the CCL file.
transport_csv = "/home/perakis/Documents/Flamelet_Tabellengenerator_Perakis/CCL/trans.csv"

# ----------------------- 19. Input -------------------------------------
# False: The transport_csv file is not used, and instead the transport values of Cantera are taken
(recommended)
# True: The transport_csv file is used
use_csv_transport = False

return GUIinput, Pressure, T_inlet_fuel, T_inlet_ox, Y_fu, Y_ox, mech_file, reduce_m,
species_to_del, ini_sol, pdf_intern, pdf_method, tabelle_name, limit_include, CCL, ccl_name,
thermo_csv, transport_csv, use_csv_transport
```

The comments in the code give a description about each variable that the user has to modify before running the main script.

Reaction mechanism

The reaction mechanism is loaded in Cantera in the form of a .cti or .xml file. In order to create such a file, three separate data have to be imported: a file containing the reactions, one with the thermodynamic values and one with the transport quantities of the species, as explained in Section 3.2.2. In order to combine the three files into a .cti one, following command has to be given in the bash-shell:

```
python2.7 ck2cti.py --input=chem.inp --thermo=therm.dat --transport=tran.dat
```

Transforming the resulting chem.cti file into a .xml one, is done by :

```
python2.7 ctml_writer.py  chem.cti
```

The Python scripts ck2cti.py and ctml_writer.py as well as some already created reaction mechanism files, ready to be implemented in Cantera, are located in the path ./Flamelet_Tabellengenerator_Perakis/Reaktionsmechanismus .

Directory structure

The Python scripts called by the main program are located at two separate directories. The ones used for the creation of the laminar table, are saved at ./Flamelet_Tabellengenerator_Perakis/laminar, whereas the ones used for the turbulent integration, are located at ./Flamelet_Tabellengenerator_Perakis/pdf-integration.

When a new Flamelet table generation is started, a directory is created at ./Flamelet_Tabellengenerator_Perakis. The name of this directory includes information about the pressure, the fuel composition and the temperature at the inlets. Within this directory, the buffer files after the solution of each counterflow diffusion flame are saved as a backup. Moreover, some plots of the Flamelet table results are exported there, used for post-processing and to examine the convergence of the calculation.

Within the same directory, also the .csv files comprising the laminar table are also saved. These are also exported into the location ./Flamelet_Tabellengenerator_Perakis/pdf-integration/canteraTables but are overwritten after each new calculation.

Finally, the Flamelet .fll table, which is later on loaded into CFX, is exported at ./Flamelet_Tabellengenerator_Perakis/pdf-integration.

Trying another propellant combination

This was not undertaken within the frame of this thesis, but it should be easy to be implemented by changing the stoichiometric mixture fraction in the appropriate field of User_inputs.py, as well as the corresponding stoichiometric coefficients. Then, simply input the desired concentration in the 5th and 6th inputs of the same file. Of course, one has to make sure that the chosen hydrocarbon is in the chosen reaction mechanism.

Table of figures

References

[1] "NASA Spaceflight," [Online]. Available: http://www.nasaspaceflight.com/2014/03/spacex-advances-drive-mars-rocket-raptor-power/. [Accessed 1 July 2016].

[2] CNES, "Moteur PROMETHEE," [Online]. Available: https://ariane.cnes.fr/fr/moteur-promethee-une-evolution-vers-des-systemes-de-lancements-europeens-tres-bas-cout. [Accessed 01 September 2016].

[3] Blue Origin, "BE-4: America's next rocket engine," [Online]. Available: https://www.blueorigin.com/be4. [Accessed 01 September 2016].

[4] ECHA, "Candidate List of substances of very high concern for Authorisation".

[5] O. J. Haidn, "Advanced Rocket Engines," in *Advances on Propulsion Technology for High-Speed Aircraft*, 2008.

[6] H. Vernin and P. Pempie, "LOX/CH4 and LOX/LH2 heavy launch vehicle comparison.," in *45th AIAA/ASME/SAE/ASEE Joint Propulsion Conference & Exhibit*, Denver, Colorado, USA, 2009.

[7] S. Magniant, P. Vinet, R. Blasi, J.-P. Dutheil and T. Motomura, "Airbus Defence and Space LOX/Methane Propulsion Demonstrator," in *65th International Astronautical Congress*, Toronto, Canada, 2014.

[8] P. J. Linstrom and W. G. Mallard, NIST Standard Reference Database Number 69.

[9] K. Liang, B. Yang and Z. Zhang, "Investigation of heat transfer and coking characteristics of hydrocarbon fuels.," *Journal of Propulsion and Power,* pp. 789-796, 1998.

[10] F. Nasuti, "Regenerative Cooling in Liquid Rocket Engines by Light Hydrocarbons," Lecture at Technical University of Munich, Munich, Germany, 2013.

[11] R. Zubrin, B. Frankie and T. Kito, "Mars In-Situ Resource Utilization Based on the Reverse Water Gas Shift: Experiments and Mission Applications.," *AIAA,* 1997.

[12] O. Knab, M. Frey, J. Görgen, C. Maedling, K. Quering and D. Wiedmann, "Progress in combustion and heat transfer modelling in rocket thrust chamber applied engineering," *AIAA Paper,* 2009.

[13] U. Walter, Astronautics: the physics of space flight, John Wiley & Sons, 2012.

[14] G. P. Sutton and O. Biblarz, Rocket propulsion elements, John Wiley & Sons, 2010.

[15] J. W. Murdock, Fundamental fluid mechanics for the practicing engineer, CRC Press, 1993.

[16] ANSYS and CFX Solver, "Theory Guide," 2013.

[17] R. J. LeVeque, Finite Volume Methods for Hyperbolica Problems, Cambridge University Press, 2002.

[18] K. H. Ferziger and M. Peric, Computational methods for fluid dynamics, Springer Science & Business Media, 2012.

[19] R. Paoli, A. Poubeau and D. Cariolle, "Large-eddy simulations of a solid-rocket booster jet," *APS Meeting Abstracts,* 2014.

[20] A. Urbano, G. Staffelbach, B. Cuenot, T. Schmitt, S. Ducruix and S. Candel, "Exploration of combustion instability triggering using Large Eddy Simulation of a mutliple injector Liquid Rocket Engine," *Combustion and Flame,* vol. 169, pp. 129-140, 2016.

[21] M. Giglmaier, "Angewandte Strömungssimulation," Lehrstuhl für Aerodynamik und Strömungsmechanik, Technische Universität München, Garching, Germany, 2015.

[22] N. Adams, "Turbulente Strömungen," Lehrstuhl für Aerodynamik und Strömungsmechanik, Garching, Germany, 2013.

[23] G. P. Smith, D. M. Golden, M. Frenklach, N. W. Moriarty, B. Eiteneer, M. Goldenberg, T. C. Bowman, R. K. Hanson, S. Song, W. C. Gardiner, V. V. Lissianski and Z. Qin, "hhtp://www.me.berkeley.edu/gri_mech/," [Online].

[24] B. J. McBride, M. J. Zehe and S. Gordon, "NASA Glenn coefficients for calculating thermodynamic properties of individual species," NASA Glenn Research Center, Cleveland, Ohio, USA, 2002.

[25] B. J. McBride, S. Gordon and M. A. Reno, "Coefficients for calculating thermodynamic and transport properties of individual species.," NASA, Cleveland, Ohio, USA, 1993.

[26] R. A. Svehla, "Transport coefficients for the NASA Lewis chemical equilibrium program.," NASA Lewis Research Center, Cleveland, Ohio, USA, 1995.

[27] C. R. Wilke, "A viscosity equation for gas mixtures," *Journal of Chemical Physics,* vol. 18, p. 517, 1950.

[28] R. S. Brokaw, "Approximate Formulas for Viscosity and Thermal Conductivity of Gas Mixtures," NASA Lewis Research Center, Cleveland, Ohio, USA, 1968.

[29] H. Riedmann, "Ein Verfahren zur Sprayverbrennungs- und Wärmeübergangssimulation in Raketenschubkammern in 3D," Institute for Aerodynamics und Gas Dynamics, University of Stuttgart, Stuttgart, Germany, 2015.

[30] T. Poinsot and D. Veynante, Theoretical and numerical combustion, RT Edwards, Inc., 2005.

[31] N. Peters, "Combustion Theory," CEFRC Summer School, Princeton, 2010.

[32] N. Peters, Turbulent Combustion, Cambridge: Cambridge University Press, 2000.

[33] R. W. Bilger, "The structure of turbulent nonpremixed flames," in *Twenty-second*

Symposium (International) on Combustion, Pittsburgh, PA, USA, 1988.

[34] N. Peters, *Verbrennungstheorie und Modellierung,* Aachen, Germany.

[35] M. Abramowitz and I. A. Stegun, Handbook of Mathematical Functions with Formulas, Graphs and Mathematical Tables, New York, USA: Dover, 1972.

[36] C. K. Law, Combustion Physics, Cambridge: Cambridge University Press, 2006.

[37] T. Fiala and T. Sattelmayer, "Non-Premixed Counterflow Flame Simulations: Scaling Rules for Fast Batch Simulations," in *Proceedings of the European Combustion Meeting*, 2013.

[38] D. G. Goodwin, H. K. Moffat and L. Raymond, *Cantera: An object- oriented software toolkit for chemical kinetics, thermodynamics, and transport processes.,* http://www.cantera.org Version 2.2.1., 2016.

[39] T. Fiala, "Radiation from High Pressure Hydrogen-Oxygen Flames and its Use in Assessing Rocket Combustion Instability," PhD Thesis, Technische Universität München, Munich, 2015.

[40] J. S. Kim and F. A. Williams, "Structures of Flow and Mixture-Fraction Fields for Counterflow Diffusion Flames with Small Stoichiometric Mixture Fractions," *SIAM Journal on Applied Mathematics,* vol. 53, no. 6, pp. 1551-1566, 1993.

[41] D. G. Goodwin, *Cantera workshop - Introduction,* California Institute of Technology: Division of Engineering and Applied Science, 2004.

[42] D. G. Goodwin, *Cantera workshop - One-Dimensional Flames,* California Institute of Technology: Division of Engineering and Applied Science, 2004.

[43] R. J. Kee, M. E. Coltrin and P. Glarborg, "Chemically reacting flow: theory and practice," John Wiley & Sons, 2005.

[44] S. Pohl, M. Jarczyk, M. Pfitzner and B. Rogg, "Real gas CFD simulations of hydrogen/oxygen supercritical combustion," *Progress in Propulsion Physics,* vol. 4, pp. 583-614, 2013.

[45] X. Wang, H. Huo and V. Yang, "Supercritical combustion of general fluids in laminar counterflows," *AIAA,* no. 1165, 2013.

[46] C. R. Wilke, "A Viscosity Equation for Gas Mixtures," *The Journal of Chemical Physics,* vol. 18, pp. 517-519, 1950.

[47] R. J. Kee, F. M. Rupley, J. A. Miller, M. E. Coltrin, J. F. Grcar, E. Meeks, H. K. Moffat, A. E. Lutz, G. Dixon-Lewis, M. D. Smooke, J. Warnatz, G. H. Evans, R. S. Larson, R. E. Mitchell, R. Petzold, W. C. Reynolds, M. Caracotsios, W. E. Steward, P. Glarborg, C. Wang and O. Adigun, "CHEMKIN Collection, Release 3.6," Reaction Design, Inc., San Diego, CA, USA, 2000.

[48] "Cantera Documentation," [Online]. Available: http://cantera.github.io/docs/sphinx/html/index.html. [Accessed 01 06 2016].

[49] H. Müller, F. Ferraro and M. Pfitzner, "Implementation of a Steady Laminar Flamelet Model for non-premixed combustion in LES and RANS simulations," in *International OpenFOAM Workshop*, Jeju, Korea, 2013.

[50] K. E. Atkinson, An Introduction to Numerical Analysis, 2nd ed., New York: John Wiley & Sons, 1989.

[51] E. Jones, T. Oliphant and P. Peterson, *Scipy: Open source scientific tools for Python,* 2001-.

[52] P. Katzy, "Entwicklung, Optimierung und Validierung eines Flamelet-Tabellengenerators für H2/O2 Verbrennungssimulationen in Raketentriebwerken," Technische Universität München, Munich, Germany, 2014.

[53] B. Ivancic, H. Riedmann, M. Frey, O. Knab, S. Karl and K. Hannemann, "Investigatino of different modeling approaches for computational fluid dynamics simulation of high-pressure rocket combustors," *EUCASS Progress in Propulsion Physics,* 2016.

[54] S. Gordon and B. J. McBride, "Computer Program for Calculation of Complex Chemical Equilibrium Compositions, Rocket Performance, Incident and Reflected Shocks, and Chapman-Jouguet Detonations," Interim Revision, 1976.

[55] H. Müller and M. Pfitzner, "Large-Eddy Simulation of transcritical LOx/CH4 Jet Flames," in *6th Europeacn Conference for Aeronautics and Space Sciences (EUCASS)*, Krakow, Poland, 2015.

[56] G. Singla, P. Scouflaire, C. Rolon and S. Candel, "Transcritical oxygen/transcritical or supercritical methane combustion," *Proc. Combust. Institute,* no. 30, pp. 2921-2928, 2005.

[57] A. Frassoldati, A. Cuoci, T. Faravelli, E. Ranzi, C. Candusso and D. Tolazzi, "Simplified kinetic schemes for oxy-fuel combustion," in *1st International Conference on Sustainable Fossil Fuels for Future Energy*, 2009.

[58] M. Muszynski and P. Alliot, "The In-Space Propulsion (Isp-1) Project," in *61st International Astronautics Congress*, Prague, Czech Republic, 2010.

[59] D. Suslov, "ISP-1: Deliverable 2.6".

[60] D. Suslov, B. Betti, T. Aichner, F. Nasuti, S. Soller and O. Haidn, "Experimental Investigation and CFD-Simulation of the Film Cooling in an O2/CH4 subscale Combustion Chamber," in *Space Propulsion Conference*, Cologne, Germany, 2012.

[61] H. Riedmann, J. Görgen, B. Ivancic, K. Makowka and M. Frey, "Numerical simulation of the hot gas side flow and wall heat transfer in CH4/O2 rocket thrust chambers," in *Space Propulsion Conference*, Rome, Italy, 2016.

[62] A. Preuss, D. Preclik, C. Mäding, J. Görgen, S. Soller, O. J. Haidn, M. Oschwald, W. Clauss, Y. Torres and J. Sender, "LOX/Methane Technology Efforts for Future Liquid Rocket Engines," in *Space Propulsion Conference*, Heraklion, Crete, Greece, 2008.

[63] R. D. McCarthy and V. Arp, "User's Guide to GASPAK," 1992.

[64] V. P. Zhukov and A. F. Kong, "Development of Skeletal Kinetic Mechanism for Methane Oxidation for High Pressures and Temperatures," in *Space Propulsion Conference*, Rome, Italy, 2016.

[65] E. Brizuela, "Accurate Normalisation of the Beta-Function PDF," *Journal of Computational Physics,* vol. 119, pp. 385-387, 1995.

[66] L. Werling, N. Perakis, B. Hochheimer, H. K. Ciezki and S. Schlechtriem, "Experimental Investigations based on a Demonstrator Unit to analyze the Combustion Process of a Nitrous Oxide/Ethene Premixed Green Bipropellant," in *5th CEAS Air & Space Conference*, Delft, Netherlands, 2015.

[67] I. D. Boyd, *Simulation of Electric Propulsion Thrusters,* DTIC Document, 2011.

[68] L. D. Landau and E. M. Lifshitz, Fluid Mechanis - Course of Theoretical Physics Volume 6, Pergamon Press, 1966.

[69] A. Chorin and J.-E. Marsden, A Mathematical Introduction to Fluid Mechanis, Springer Verlag, 2000.

[70] H. Pitsch, "Flamemaster," [Online]. Available: http://www.itv.rwth-aachen.de/downloads/flamemaster/.